LAMINAR FLAME PROPAGATION STUDIES IN A SPHERICAL COMBUSTION CHAMBER; EXPERIMENTAL AND NUMERICAL APPROACHES

A THESIS SUBMITTED TO
THE GRADUATE SCHOOL OF NATURAL AND APPLIED SCIENCES
OF
MIDDLE EAST TECHNICAL UNIVERSITY

BY

TAHSİN BERK KIYMAZ

IN PARTIAL FULFILLMENT OF THE REQUIREMENTS
FOR
THE DEGREE OF MASTER OF SCIENCE
IN
MECHANICAL ENGINEERING

JANUARY 2023

Approval of the thesis:

LAMINAR FLAME PROPAGATION STUDIES IN A SPHERICAL COMBUSTION CHAMBER; EXPERIMENTAL AND NUMERICAL APPROACHES

submitted by **TAHSİN BERK KIYMAZ** in partial fulfillment of the requirements for the degree of **Master of Science** i**n Mechanical Engineering, Middle East Technical University** by,

Prof. Dr. Halil Kalıpçılar
Dean, Graduate School of **Natural and Applied Sciences** _____

Prof. Dr. M.A. Sahir Arıkan
Head of the Department, **Mechanical Engineering** _____

Prof. Dr. Ahmet Yozgatlıgil
Supervisor, **Mechanical Engineering, METU** _____

Prof. Dr. İskender Gökalp
Co-Supervisor, **Mechanical Engineering, METU** _____

Examining Committee Members:

Assist. Prof. Dr. Özgür Uğraş Baran
Mechanical Engineering, METU _____

Prof. Dr. Ahmet Yozgatlıgil
Mechanical Engineering, METU _____

Prof. Dr. Oğuz Uzol
Aerospace Engineering, METU _____

Prof. Dr. Metin Muradoğlu
Mechanical Engineering, Koç Uni. _____

Assoc.Prof. Dr. Barış Yılmaz
Mechanical Engineering, Marmara Uni. _____

Date: 04.01.2023

I hereby declare that all information in this document has been obtained and presented in accordance with academic rules and ethical conduct. I also declare that, as required by these rules and conduct, I have fully cited and referenced all material and results that are not original to this work.

Name Last name : Tahsin Berk Kıymaz

Signature :

ABSTRACT

LAMINAR FLAME PROPAGATION STUDIES IN A SPHERICAL COMBUSTION CHAMBER EXPERIMENTAL AND NUMERICAL APPROACHES

Kıymaz, Tahsin Berk
Master of Science, Mechanical Engineering
Supervisor: Prof. Dr. Ahmet Yozgatlıgil
Co-Supervisor: Prof. Dr. İskender Gökalp

January 2023, 115 pages

Global interest in hydrogen as an energy carrier for combustion and fuel cell applications to reduce CO2 emissions is expanding. However, the use of 100% hydrogen in combustion applications is still technologically and logistically immature, necessitating substantial adjustments to infrastructures linked to hydrogen generation, transfer, and conversion. Thus, blending hydrogen is considered as a preliminary approach on this transition. This work investigates laminar flame propagation of natural gas - air and natural gas - hydrogen - air premixtures in a spherical combustion chamber, both experimentally and numerically. H_2 addition rates up to 20% are investigated at atmospheric conditions for lean and stoichiometric conditions. A spherical combustion chamber is designed, manufactured, and commissioned to investigate spherical laminar flame propagation. Experiments were performed at 1bar and at 288 ± 2K. The experimental setup consists of a high-pressure combustion chamber, a Schlieren visualisation system and a high-speed video camera for flame images recording. Captured images are post processed to obtain flame radius in each frame. Linear methodology is used to extrapolate the experimentally measured stretched laminar burning velocities to the unstretched ones. The laminar flame speeds of the investigated mixtures are

compared with the literature results and 1D and 2D numerical simulations. It is shown that the laminar flame speeds of NG-air mixtures increase with hydrogen addition to the fuel. Additionally, laminar boundary layer flame flashback is investigated numerically. 2D transient computations were performed up to 20% hydrogen addition rate into methane-air mixtures for 300K and 600K wall temperatures. Laminar flashback limits were calculated; it is found that flashback propensity increases with increasing wall temperature and increasing hydrogen addition rate. The quenching distance decreases with hydrogen addition to the mixture.

Keywords: Laminar Premixed Flames, Laminar Flame Speed, Spherically Expanding Flames, Hydrogen Enriched Natural Gas, Flame Flashback, Schlieren Visualisations, OpenFOAM 2D Flame Simulations

ÖZET

KÜRESEL YANMA ODASINDA LAMİNER ALEV YAYILIM ÇALIŞMALARI DENEYSEL VE SAYISAL YAKLAŞIMLAR

Kıymaz, Tahsin Berk
Yüksek Lisans, Makina Mühendisliği
Tez Yöneticisi: Prof. Dr. Ahmet Yozgatlıgil
Ortak Tez Yöneticisi: Prof. Dr. İskender Gökalp

Ocak 2023, 115 sayfa

CO_2 salımlarını azaltmak için yanma ve yakıt hücresi uygulamaları ile kullanılabilen bir enerji taşıyıcısı olan hidrojene olan ilgi artmaktadır. Yanma uygulamalarında %100 hidrojen kullanımı teknolojik ve lojistik açılardan henüz olgunlaşmamış olup, hidrojen üretimi, iletimi ve dönüşümü ile bağlantılı altyapılarda önemli yenilemeler yapılmasını gerektirmektedir. Bu nedenle, hidrojenin doğal gaz ile karıştırılması bu süreçte bir ön yaklaşım olmaktadır. Bu çalışma, küresel bir yanma odasında doğal gaz-hava ve doğal gaz-hidrojen-hava ön karışımlarının laminer alev yayılımını deneysel ve sayısal olarak incelemektedir. %20'ye varan hidrojen ilave oranları, fakir ve stokiyometrik koşullar için atmosferik koşullarda araştırılmıştır. Laminer alev yayılımını araştırmak üzere küresel bir yanma odası tasarlanmış, imal edilmiş ve devreye alınmıştır. Deneyler 1 bar'da ve 288±2K'da yapılmıştır. Deney düzeneği başlıca, yüksek basınçlı bir yanma odasından, yakıt besleme sisteminden, Schlieren görüntüleme sisteminden ve alev görüntülerinin kaydedilmesi için kullanılan hızlı video kamerasından oluşmaktadır. Elde edilen görüntüler anlık alev yarıçapını elde etmek için işlenmiştir. Ölçülen gerilmiş laminer yanma hızlarından gerilmemiş olanları tahmin etmek için lineer yaklaşım kullanılmıştır. İncelenen karışımlar için

elde edilen laminer alev hızları, literatür sonuçları ve 1 ve 2 boyutlu sayısal hesaplamalar ile karşılaştırılmıştır. Yakıta hidrojen ilavesiyle doğal gaz-hava karışımlarının laminer alev hızlarının arttığı gözlenmiştir. Ayrıca, laminer sınır tabaka alev geri tepme süreci sayısal olarak incelenmiştir. 300K ve 600K yakıcı çeper sıcaklıkları ve metan-hava karışımına %20'ye kadar hidrojen ekleme oranları için 2 boyutlu hesaplamalar yapılmıştır. Laminer alev geri tepme sınırları hesaplanmış ve artan çeper sıcaklığı ve artan hidrojen ekleme oranı ile alevin geri tepme eğiliminin arttığı bulunmuştur. Karışıma hidrojen ilavesiyle söndürme mesafesinin azaldığı tespit edilmiştir.

Anahtar Kelimeler: Laminer Ön Karışımlı Alevler, Laminer Alev Hızı, Küresel Yayılan Alevler, Hidrojen ile Zenginleştirilmiş Doğal Gaz, Alev Geri Tepmesi, Schlieren Görüntüleme Tekniği, OpenFOAM 2 Boyutlu Alev Hesaplamaları

To my family…

ACKNOWLEDGMENTS

I would like to express my deepest gratitude to my mentor Prof. Dr. İskender Gökalp for his guidance, encouragement, and availability. I am truly proud to be his student. I am grateful to my supervisor Prof. Dr. Ahmet Yozgatlıgil for his support.

I wish to express my sincere thanks to all the members of my jury for their valuable comments and time.

My special thanks go to Dilay Güleryüz for her contributions on our flame flashback studies, for supporting and motivating me, and most importantly, for being the best companion in our adventures. Similarly, I'd like to thank Emre Böncü for his contributions to flame flashback studies, the insightful discussions we had, and for reminding me that “the journey is what matters”.

There are three valuable individuals who always were available for me, namely Dr. Mehmet Karaca, Dr. Christophe Allouis and Doç. Dr. Barış Yılmaz. I would like to express my heartfelt thanks to them for sharing their guidance during the past two and a half years.

This thesis was made possible by the financial support of two TÜBİTAK BİDEB Uluslararası Lider Araştırmacılar projects (project 118C287, PI Dr. İskender Gökalp and project 118C233, PI Dr. Christophe Allouis). I express my sincere thanks to TÜBİTAK for providing the financial support to design, build and operate the spherical combustion experimental facility and for my Master's study grant.

I would like to thank TÜBİTAK ULAKBİM, High Performance and Grid Computing Center (TRUBA) since the numerical calculations were performed using their resources.

My warmest thanks go also to TÜBİTAK-SAGE for hosting me to conduct the experiments using their experimental site, techniques and expertise: special thanks to Semra Gümrük, Ozan Can Kocaman, Dr. Bora Yazıcı and Dr. Bülent Sümer for their technical availability and their kindness.

Oğuz Kaya and his team from the Pro-sis Mühendislik company were truly instrumental for the design, manufacturing, and commissioning of the spherical combustion chamber facility. I express my deepest thanks to them.

I would also like to thank Fatih Coşkun and his team at Yediç Mühendislik for their several interventions in parts of the experimental facility.

I am grateful to Dr. Gökhan Çelik and his team from the Chemical Engineering Department for their help.

From the administrative side, I express my thanks to ODTÜ-BAP, especially to its Director Doç. Dr. Hüsnü Dal. and to Mehtap Dişbudak and Şaban Dişbudak for their various administrative helps.

I would like to thank my Department of Mechanical Engineering at METU for all those years I spent with them for my education. During my thesis, Turan Kalender took care of several administrative businesses especially for the provisioning of the needed materials for my experiment. I also address him very special thanks.

During my master studies, I shared lots of good memories with our team (Dr. Rasiha Nefise Mutlu, Dr. Esra Eroğlu and Dr. Jayaraman Kandasamy) in the C- Building. Thank you for the warmest work environment and many discussions.

Last but not least, I would like to thank my mother and father for their endless faith in me throughout my whole life and my little brother for his encouragement. Also, special thanks go to my dearest friend Orhun Taşoğlu for his guidance in all parts of my work related to electrical engineering, and to Yiğit Vural for the design ideas and countless parts he manufactured for me. I am grateful to my beloved friends Damla San, Emre Karabıyık, Alptuğ Calasın and Berke Çetiner for giving me all the support I needed; and Hakan Bostan for his availability for my never-ending questions.

TABLE OF CONTENTS

LIST OF TABLES

TABLES

LIST OF FIGURES

FIGURES

LIST OF ABBREVIATIONS

1D	One Dimensional
2D	Two Dimensional
3D	Three Dimensional
CFD	Computational Fluid Dynamics
CPM	Constant Pressure Method
CVM	Constant Volume Method
DAC	Dynamic Adaptive Chemistry
DNS	Direct Numerical Simulation
DC	Direct Current
FKM	Fluro-Elastomer Material
ISAT	In-Situ Adaptive Tabulation
Le	Lewis Number
LES	Large Eddy Simulation
NG	Natural Gas
NPT	National Pipe Thread (American)
OD	Outer Diameter
PISO	Pressure Implicit with Splitting of Operator
RANS	Reynolds Averaged Navier-Stokes
SIMPLE	Semi-Implicit Method for Pressure-Linked Equations
TDAC	Tabulated Dynamic Adaptive Chemistry

LIST OF SYMBOLS

a	Thermal diffusivity
D	Mass diffusivity
D_{ij}	Binary diffusion coefficients
g_c	Critical gradient at flashback
h_s	Sensible enthalpy
Ji	Diffusion flux
K	Stretch rate
K_S	Strain rate
L	Markstein Length
l_D^0	Preheating zone thickness
l_R^0	Reaction zone thickness
M_i	Molecular weight
N_{Oxi}	Total number of oxidizer moles
R_f	Flame radius
$\dot{R}_h$	Heat release term due to chemical reactions
$\dot{R}_\iota$	Reaction source term
S_L^0	Unstretched laminar flame speed
S_L	Stretched laminar flame speed
T_u	Unburned gas temperature
T_b	Burned gas temperature

u_f	Mean bulk cold flow velocity at flashback
u_g	Velocity of the unburned gas
V_s	Stretched laminar flame burning velocity
V_{S0}	Unstretched laminar flame burning velocity
W_0	Principle branch of the Lambert function
X_i	Mole fractions
Y_b	Burned mixture mass fraction
Yu	Fresh mixture mass fraction
α	Bunsen flame cone angle
δ_p	Penetration distance
δ_d	Quenching distance
κ	Flame curvature
λ	Thermal conductivity of the mixture
ρ_u	Unburned gas density
ρ_b	Burned gas density
σ	Expansion ratio
τ	Viscous stress tensor
Φ	Equivalence ratio

CHAPTER 1

INTRODUCTION

1.1 Background

Hydrocarbon fossil fuels will continue to be the main source of energy for modern society for the foreseeable future, despite the recent significant advancements made in the development of renewable energies [1]. Transportation, electricity generation, and industries require high temperatures (cement, glass, iron production), and thus rely heavily on combustion processes. However, pollution resulting from combustion processes contributes to environmental problems. The link between CO_2 emissions and the global warming, for instance, is already well-established and may constitute a substantial threat for the human beings and the nature.

Global interest in hydrogen as an energy carrier for combustion and fuel cell applications to reduce CO_2 emissions is expanding. However, the use of 100% hydrogen in combustion applications is still technologically and logistically immature, necessitating substantial adjustments to infrastructures linked to hydrogen generation, transfer, and conversion. Hydrogen Enriched Natural Gas studies and uses could be a preliminary strategy [2-7] for facilitating the introduction of hydrogen.

With the addition of H_2 to a CH_4-Air premixture, combustion parameters such as the laminar flame speed, flame thickness, flammability limits, and adiabatic flame temperature change. Presently, there is no unified regulation for hydrogen blending rates at the EU level. It is important to explore how the performances of present domestic combustion devices, such as gas-fired ovens, water heaters (boilers) for heating purposes, and cooktop burners, change under the effect of blending hydrogen to natural gas. Manufacturers of internal combustion engines and gas turbines are

developing fuel-flexible combustion systems since several years, making them tolerant to high levels of hydrogen enrichment rates from an industrial standpoint. But the degree of research effort in the literature is insufficient for fuel interchangeability in household combustion appliances. Consequently, it is crucial to evaluate the safe hydrogen injection limits into the current natural gas (NG) distribution network, as well as the safe combustion limits and performance characteristics of this mixture [8]. Premixed combustion of hydrogenated mixtures may cause the possibility of upstream flame propagation into the premixing sections of the combustion appliance, often known as the flame flashback phenomenon. This is one of the major reasons for investigating the combustion properties of hydrogenated natural gas – air mixtures.

1.2 Motivation

The aim of this thesis is investigating laminar flame characteristics of NG + Air and NG+H_2+Air premixtures. An experimental setup is designed and built for this purpose and used to measure laminar flame speeds of these premixtures using spherically expanding flame method at atmospheric conditions. This setup can be further used to determine laminar flame speeds of various premixtures such as biogas+air and syngas+air also under high pressure and temperature conditions. Additionally, 2D modelling of NG+Air and NG+H_2+Air premixtures are developed and compared to the experimental values. Lastly, laminar flame flashback phenomenon is numerically investigated, to analyse the increase of the flame flashback risk with H_2 addition.

1.3 Thesis Structure

This thesis investigates spherically expanding laminar flames experimentally and numerically. Additionally, numerical boundary layer flame flashback studies are presented. The thesis comprises a total of 7 Chapters.

- Chapter 2 introduces premixed laminar flames, and the definitions of its fundamental parameters. This chapter mostly introduces the theory and previous work done in the literature.
- Chapter 3 presents the experimental methodology, where the recently built spherical combustion chamber setup is presented. This chapter also introduces experimental procedures and methods used for post processing.
- Chapter 4 explains the numerical methodology used for modelling both 2D spherically propagating flames and the boundary layer flame flashback phenomenon. Details of the spherically propagating flame modelling is presented in this chapter.
- Chapter 5 presents our experimental results on spherically expanding flames and their comparison with 1D flame computations and the experiments found in the literature. 2D spherically expanding flame computation results are also presented in this chapter.
- Chapter 6 discusses the modelling and numerical methodologies we used for boundary layer flame flashback studies, and the obtained results.
- Chapter 7 summarizes the main conclusions of the work done in this thesis and the future work suggestions.

CHAPTER 2

LITERATURE REVIEW

2.1 Laminar Premixed Flames Phenomenology

Premixed flames are defined as a type of flame where reactants and oxidizers are mixed homogeneously at the molecular level before combustion occurs. These flames are investigated in two categories based on their flow characteristics, laminar or turbulent. In a laminar flow, the fluid moves in a straight and predictable path, with little mixing between the different layers. Laminar flows are related to smooth and orderly characteristics having low velocities, especially with no spatial or temporal variations of flow parameters such as the velocity [9]. Turbulent flows are characterized by random structures where all the flow parameters fluctuate in time and space. The tools of statistical mechanics and mathematics are needed to analyse turbulent flows [10].

To achieve a stable laminar premixed flame, fuel and oxidizer should be mixed in correct proportions there should not be any disturbances in the flow. The ratio of the fuel to air in premixed flames is defined as the equivalence ratio (Φ). It represents the ratio of the actual amount of the fuel in the mixture to the required oxidizer for complete combustion reactions. A stoichiometric mixture ($\Phi=1$) is defined as the mixture where all the fuel and oxidizer in the reactants are consumed at the end of the reaction zone. For $\Phi > 1$ the mixture is named rich and for $\Phi < 1$ it is named lean. In this work, lean and stoichiometric mixtures are considered for spherical flame propagation studies; in addition, rich flames are studied for the laminar flame flashback computations.

2.1.1 Structure of Laminar Premixed Flames

In the detailed work of Law and Sung [11] three layers of complexity are introduced to describe the structure and propagation of a typical premixed flame. Figure 2.1 explains the first level analysis, the hydrodynamic flame sheet model.

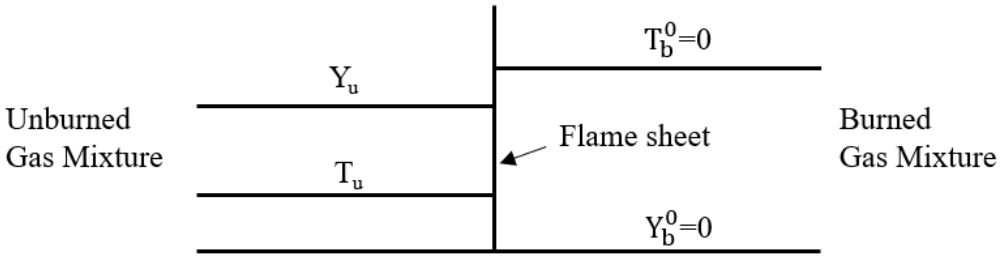

Figure 2.1. Adiabatic, one-dimensional, freely propagating planar premixed flame; hydrodynamic (first) level analysis

The hydrodynamic (first) level analysis assumes that unburned and fresh gases are in a state of thermodynamic equilibrium, and the flame sheet is conceived as an interface dividing them. The temperature and reactant mass fractions abruptly shift from (unburned gas temperature) to T_b^0 (burned gas temperature) and from Y_u (fresh mixture mass fraction) to Y_b^0=0 (burned mixture mass fraction), correspondingly, at the interface. In this analysis level, chemical kinetics and transport properties are not considered.

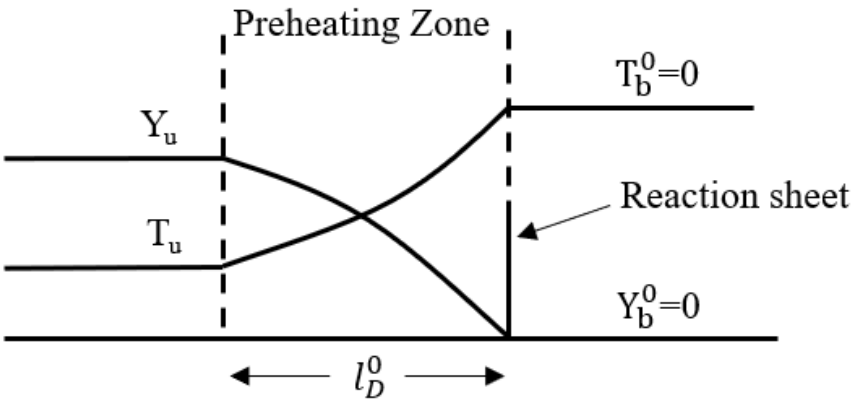

Figure 2.2. Adiabatic, one-dimensional, freely propagating planar premixed flame; transport (second) level analysis

In the second, transport-dominated level analysis, the flame sheet from Fig. 2.1 is enlarged to reveal a preheating zone with thickness l_D^0 (Fig. 2.2) and is controlled by heat and mass transport processes. As the mixture gets closer to the flame, it is gradually heated by the heat transmitted forward from the region of chemical heat release, resulting in a temperature profile that continually increases until T_b is attained. Continuous heating of the mixture will eventually result in its ignition, followed by sustained chemical reactions. The reactions are assumed to be activated only where/when the required ignition temperature is attained. Therefore, at this second level analysis the reactions are assumed as concentrated in a thin zone, which is called a reaction sheet.

The disappearance of reactant concentrations at the reaction sheet produces a concentration gradient in the preheating zone. Thus, the reactant concentration continuously drops in the preheating zone. Moreover, for mixtures whose Lewis number (Le) is close to one, the similar values of heat and mass diffusivities indicate that the rate of temperature increase should be comparable to that of the concentration decrease. The Lewis number is defined as the ratio of the thermal diffusivity (a) to the mass diffusivity of the mixture (D).

$$Le = \frac{a}{D}$$

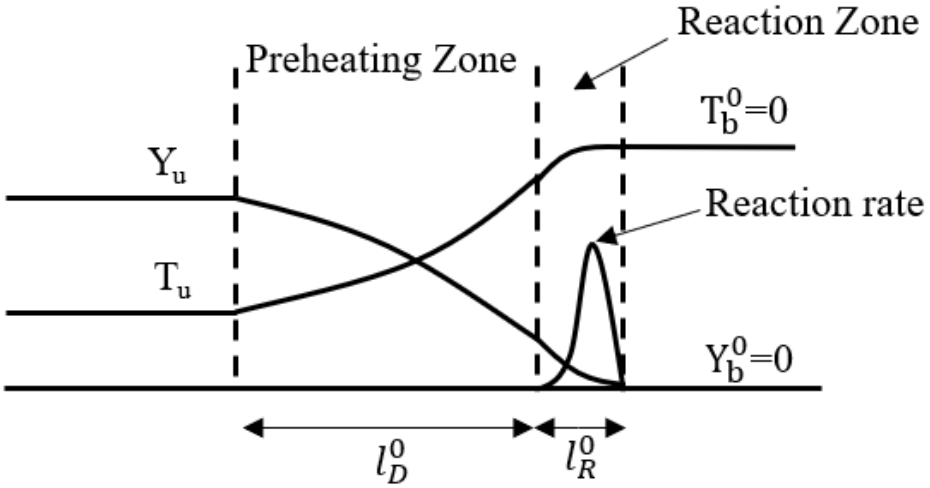

Figure 2.3. Adiabatic, one-dimensional, freely propagating planar premixed flame; reaction (third) level analysis

Thermal and molecular transport processes are taken into consideration in the most detailed third level analysis of laminar flames as proposed by Zeldovich and Frank-Kamenetsky [12] based on the Mallard and Le Chatelier theory [13]. The flame structure is then split into two distinct zones, as depicted in Figure 2.3: a narrow reaction zone (l_R^0) where reaction and diffusion rates balance each other, and a thick preheating zone (l_D^0) where convection and diffusion dominate and balance each other. In the reaction zone, bulk of the chemical energy is released while in the preheat zone there is little heat release [14]. It is assumed that $l_D^0 >> l_R^0$. The activation of the reactions and the depletion of reactants work together to form the reaction rate profile in the reaction zone.

2.1.2 Definition of the Laminar Flame Speed

Laminar flame speed is a flame parameter, which has crucial impact on the combustion characteristics [15]. It is important for both laminar and turbulent flames, since the turbulent flame speed correlations are also based on the laminar flame

speed knowledge. It also contributes to the understanding of various combustion phenomena such as flame stabilization, flame flashback, flame blowout, and flame extinction [14]. Additionally, it is used as an important parameter for the validation of chemical kinetic mechanisms.

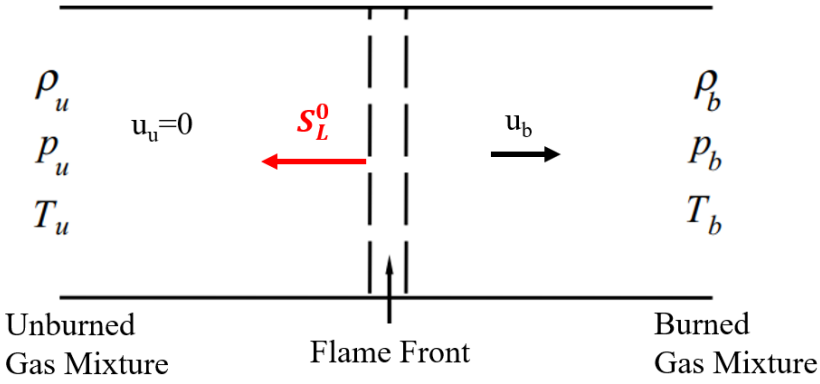

Figure 2.4. Representation of a planar laminar premixed flame propagating through a quiescent unburned gas mixture

The laminar flame speed (S_L^0) can be defined as the speed of the flame front propagating normally to its surface through a quiescent, homogeneous mixture of unburned reactants, under adiabatic conditions [14]. It is a fundamental flame parameter that depends on the pressure, temperature, and species composition of the unburnt mixture [16]. Differences between the unstretched (S_L^0) and stretched (S_L) laminar flame speed will be explained in the following chapters in detail.

Generally, S_L^0 increases with increasing temperature and decreases with increasing pressure. The chemical composition of the unburnt mixture has a significant impact on the laminar flame speed. For example, laminar flame speed of hydrogen is higher than that of hydrocarbons because of its lower molecular weight and higher reactivity with oxygen. [17]. There are different methodologies described in the literature to obtain experimentally the laminar flame speed of various mixtures, which will be explained in detail in the following chapters.

2.1.3 Definition of the Flame Stretch

Flame stretch occurs when an external flow is applied to laminar, premixed flames. It is defined as the fractional area change of a Lagrangian flame surface element:

$$K = \frac{dA}{Adt} \tag{2.1}$$

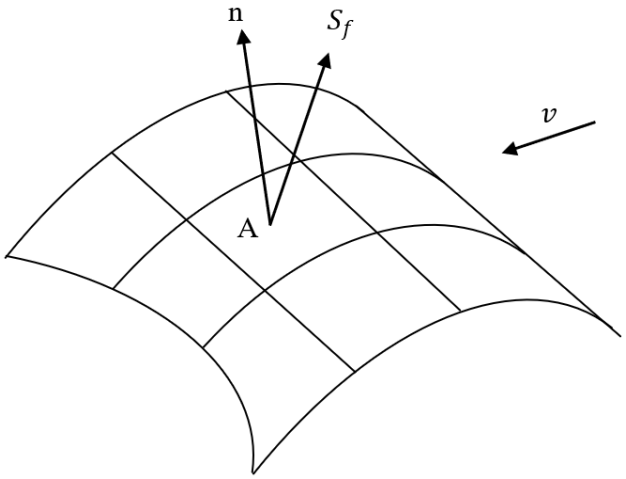

Figure 2.5. Schematic representation of a flame surface subjected to stretch

Flame stretch is an important phenomenon, which is studied extensively in the literature [18-23]. In this work, the definition of Matalon is used [18]. Based on kinematic considerations, flame stretch is expressed by using the flame curvature and the strain rate as follows:

$$K = S_f \kappa + K_S \tag{2.2}$$

where S_f is the flame surface speed. In the context of hydrodynamic theory, $S_f \approx S_L$ [18].

κ is the flame curvature and is defined as:

$$\kappa = -\nabla \cdot \mathrm{n} \tag{2.3}$$

and K_S is the strain rate defined as:

$$K_S = -(v \cdot n)\kappa + \nabla_\tau \cdot v_\tau \tag{2.4}$$

where the first term is associated with the normal straining and the second term with tangential straining. Overall, flame stretch can be defined with 3 terms [18] as:

$$K = S_L\kappa - (v \cdot n)\kappa + \nabla_\tau \cdot v_\tau \tag{2.5}$$

- The first term indicates the stretch due to flame curvature and the flame front element can be contracted or expanded by the propagating motion depending on the sign of the curvature.
- The second term is the normal straining, and the flame front element can be contracted or expanded based on the sign of the curvature.
- The third term is the tangential straining represented by the divergence of the tangential velocity vector. The flame front element can be expanded or compressed by this term.

Fig. 2.6a shows the normal straining and Fig. 2.6b the tangential straining applied on a flame surface area.

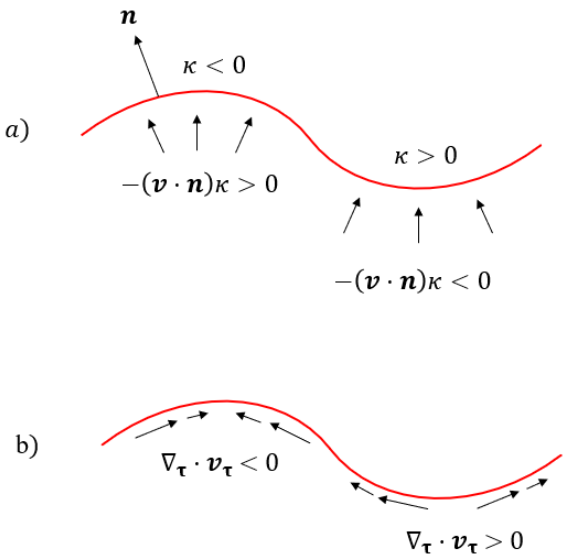

Figure 2.6. a) Normal straining on a flame surface b) Tangential straining on a flame surface

It is suggested by asymptotic theories [19-22], for flames with Le close to unity and exposed to weak stretch, K is accepted as the only parameter controlling the structure of the laminar flame. Thus, the following linear relationship between the flame speed and the stretch rate is proposed by Markstein [25] and used extensively in the literature. This relation suggests that the unstretched laminar flame speed can be related to the stretched laminar flame speed, using the Markstein length (L) concept and the flame stretch. It is assumed that L is constant, and the stretched laminar flame speed can be extrapolated to the unstretched one linearly.

$$S_L = S_L^0 - LK \tag{2.6}$$

For high stretch rates and/or mixtures with Le numbers far from unity, it is found that this linear extrapolation overpredicts the laminar flame speed values and non-linear extrapolation methods are suggested in the literature [26-28].

2.1.4 Laminar Flame Flashback Phenomenon

Laminar flame flashback happens when the laminar flame speed surpasses the bulk cold premixture velocity. It is an unwanted phenomenon because flashback can carry the flame front to regions of the combustion system that are not designed to sustain a flame [29,30]. This can damage the device parts which were not designed to endure the burned gases high temperatures and even may cause explosions. Laminar flame flashback may happen in different forms such as core flow flashback, boundary layer flashback and combustion instability induced flashback. The only focus in this work is on the boundary layer flashback phenomenon.

Flashback limits depend on various parameters such as the unburnt flow velocity gradients, laminar flame speed, burner diameter, tip temperature, burner material, wall and preheat temperatures and the pressure. Boundary layer flashback is first studied by Lewis and von Elbe in 1943 [31]. They developed a model based on the critical gradient concept, after series of experiments using Bunsen type burners with laminar flows. This model assumes a fully developed laminar velocity profile of the cold premixture at the burner inlet and introduces two critical parameters: the quenching distance (δ_q) and the penetration distance (δ_p), shown in Fig. 2.7. The quenching distance is the distance from the burner inner wall where chemical reactions are quenched due to heat losses to the wall. The penetration distance is the distance from the wall at which the local laminar flame speed is equal to the local premixture velocity at flashback conditions.

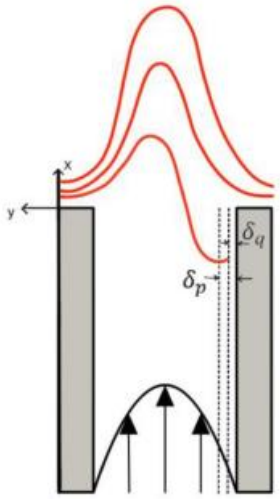

Figure 2.7. Illustration of boundary layer flashback parameters in a laminar premixed flame.

At some distance from the wall, burning velocity is higher than the flame velocity, thus flashback occurs. In this model, flashback is then associated with the velocity gradient of the unburned mixture at the wall, Eq. (2.7).

$$g_{wall} = \left|\frac{\partial u_x}{\partial y}\right|_{y=0} \tag{2.7}$$

In a circular burner, a fully developed laminar flow profile can be represented with the Hagen-Poiseuille flow equation where y is the coordinate normal to the wall and d is the burner diameter.

$$u_x(y) = 2u_{avg}\left[1 - \left(2\frac{y}{d} - 1\right)^2\right] \tag{2.8}$$

Then analytically, using Eq. (2.7) and Eq. (2.8), the critical gradient is calculated as:

$$g_c = \frac{8u_f}{d} \tag{2.9}$$

where u_f is the bulk average velocity at flashback. Assuming that the local premixture velocity variation is linear close to the wall, the gradient is approximated as the ratio of the laminar flame speed (S_L) to the penetration distance. This is because the local premixture velocity is accepted to be equal to the laminar flame speed at the penetration distance.

$$g_c = \frac{S_L}{\delta_p} \tag{2.10}$$

Combining Eqs. (2.9) and (2.10), u_f can be expressed from the critical gradient definition as,

$$u_f = \frac{dS_L}{8\delta_p} \tag{2.11}$$

On the basis of Lewis and von Elbe's theory, Putnam et al. [32] proposed that the critical gradient concept can be represented by the Peclet number (the ratio of advection transport to thermal diffusion transport) of the bulk premixture flow at flashback. The approach of Putnam et al. [32] also assumes a linear velocity profile near the wall as Lewis and von Elbe [31].

Since the critical gradient concept of Lewis and von Elbe [31] does not take stretch effects into account, Hoferichter et al. [33] proposed a critical flashback correlation based on the critical gradient concept with stretch effects, by using the Markstein length. This model again uses the Hagen-Poiseuille flow profile as in the critical gradient concept and requires the penetration distance as an input. The modified correlation employs the stretched laminar flame speed instead of the unstretched laminar flame speed.

2.2 Experimental Laminar Flame Speed Determination Methodologies

2.2.1 Bunsen Burner Method

The Bunsen burner method is a conventional way to determine the laminar burning velocities of different fuel + air mixtures, used in the literature extensively due to its simple setup. Under laminar flow conditions, a stationary premixed conical flame is attached at the exit of the burner nozzle in this method [16]. If necessary, the incoming mixture may be preheated to study the temperature effects on the laminar flame speed. This method can be applied to different mixtures with a wide range of unburnt gas velocities [34].

In this method, since the flame is stationary, the laminar flame velocity becomes equal to the normal component of the velocity of the unburned gases. Fig. 2.8 represents the flame front in a Bunsen burner. Eq. 2.12 shows the relation between the stretched flame speed, S_L , the velocity of the unburned gas, u_g, and the flame cone angle, α.

$$S_L = u_g sin\,(\alpha) \tag{2.12}$$

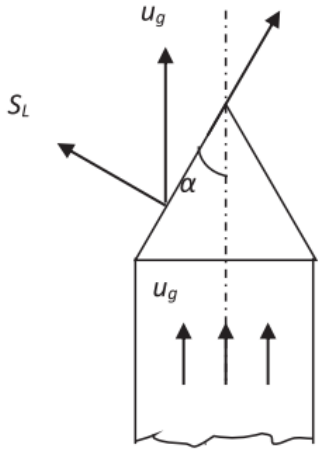

Figure 2.8. Schematic representation of the Bunsen Burner Method

The drawback of the Bunsen burner method is that it assumes that there is no strain effects or heat losses present at the burner's lips [16].

2.2.2 Stagnation Flame / Counterflow Flames Method

In the counterflow flame configuration method, two identical fuel and oxidizer premixtures are allowed to flow towards each other [35-36]. The flow velocities are precisely controlled to generate two stable laminar flames as shown on Fig. 2.9.

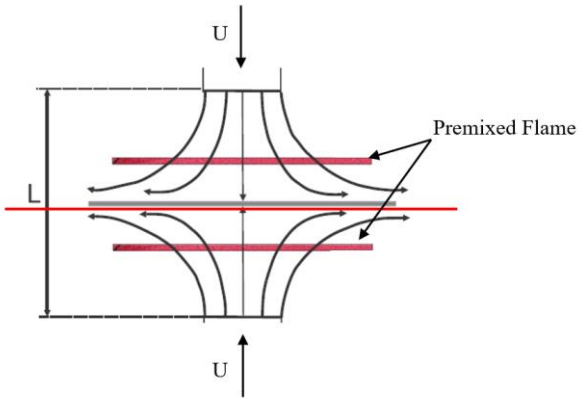

Figure 2.9. Counterflow method schematic with twin flat premixed flames

In this configuration, there is only the strain rate which contributes to the flame stretch, and it is defined as:

$$K = 2U/L \tag{2.13}$$

where U is the cold flow exit velocity and L is the burner separation distance. The flame speed is equal to the exit cold flow velocity for which twin stable flames are obtained. By changing the exit cold flow velocities or the distance between the two burners, the strain rate can be changed and the variation of the flame speed with the strain rate can be obtained as well as the unstrained laminar flame propagation speed by extrapolation.

2.2.3 Heat Flux Method

The heat flux method, introduced by van Maare [37], is a method that does not require any extrapolation due to stretch or heat loss effects [38]. In this configuration, a flat flame can be obtained due to design of perforated burner plate placed on the burner. The burner design is depicted schematically in Figure 2.10a, and it consists of a perforated burner plate, a heating jacket around the burner plate to raise its temperature and compensate for the heat loss from the flame, a series of thermocouples embedded inside the burner plate to measure the radial temperature distribution, a plenum chamber to smooth the flow velocity of the unburned fuel/oxidizer premixture, and a cooling jacket to keep the plenum chamber at a constant temperature [39].

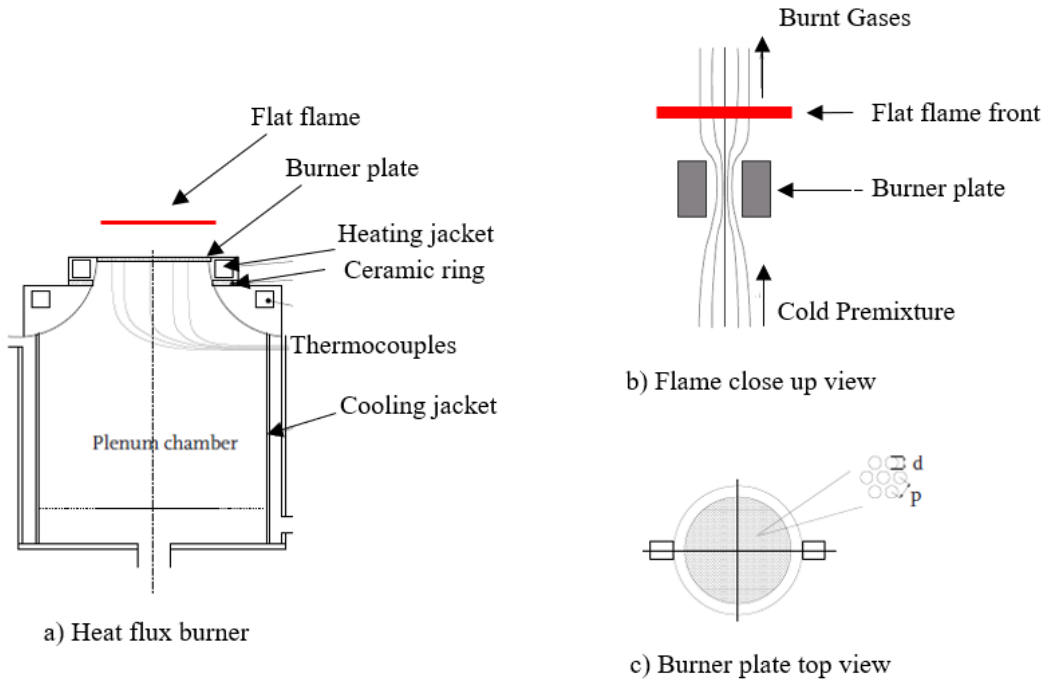

Figure 2.10. a) Heat flux burner b) Close up view of the flat flame c) Burner plate top view and perforation pattern

In order to stabilize the flat flame, cold premixture is preheated with the heating jacket. The heat loss from the flame to the burner rim can be compensated with this preheating effect. The difference between the heat loss to the burner rim and the heat gain from the heating jacket is monitored with thermocouples. The cold premixture velocity is adjusted to the value where the heat gain and loss are equal to each other, resulting in an adiabatic flame. Therefore, the laminar flame speed of the stabilized flat flame is equal to the cold premixture velocity.

Even though the laminar flame speed obtained from the heat flux method agrees well with various numerical predictions and results obtained from other measurement techniques, there are some inherent difficulties, such as the following: Adjusting the cold flow velocity is difficult and interpolation of the gas velocity to a zero-heat flux is required. Detailed information about the interpolation can be found in the thesis of Hermanns [39] Measuring laminar burning velocities at higher mixture temperatures is difficult as the flame stand-off distance decreases, resulting in the quenching phenomenon close to the plate; at high pressures, burning velocities are very low and flame stabilization becomes difficult beyond 10 bar [40,41]. Additionally, this configuration has a very complex design to build and operate.

2.2.4 Spherically Expanding Flames

In this method, a premixed fuel + air mixture at known equivalence ratio, initial temperature, and pressure conditions is introduced in a constant volume spherical chamber. After ignition of the mixture by depositing the necessary ignition energy by a spark or a laser, a spherical flame propagates outwards in the homogenous quiescent fuel mixture (Fig. 2.11) [42]. The advantage of this method is that laminar flame speed of mixtures at elevated pressures and high temperatures can be obtain easily, compared to other methods [28, 43, 44]. This method is based on the assumptions that flame is adiabatic and burned gases are stagnant and in thermodynamic equilibrium [44]. Additionally, the flame front is accepted as a smooth surface free from any diffusional/thermal and hydrodynamic instabilities.

This method can be used in two different configurations, namely constant volume method (CVM) and constant pressure method (CPM).

Lewis and von Elbe used the constant-volume propagating spherical flame method for the first time in 1934 [45]. They measured the evolution of the chamber pressure as the spherical flame propagates in a closed thick-walled spherical vessel [46]. The pressure-time history is used to calculate burning velocities for a wide range of temperatures and pressures Later studies used the outwardly propagating flame front images recordings to determine the laminar flame speed [7, 43, 47, 48].

In CPM, the chamber pressure is kept constant as the flame expands with different methods [44]. In order to achieve higher pressures in the experimental setup, Law et al. [49] designed a dual chamber setup, where the pressure inside the chamber is kept constant by mechanical holes opening and closing between the inner and outer chamber. Later, Qin and Ju [50], modified the design of Law et al. by introducing magnetically controlled gates for pressure relief.

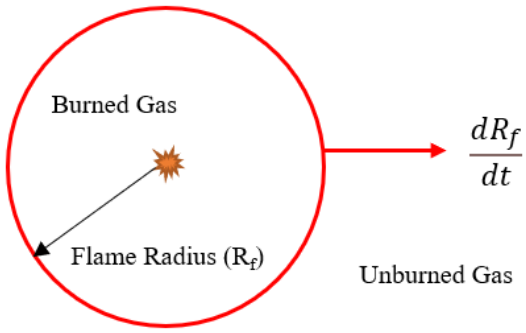

Figure 2.11. Representation of the spherically expanding flame

Even though the spherically expanding flame method has advantages over other methods, it also has some drawbacks. Spark ignition can generate instabilities due to

the initial energy deposit. During the ignition phase, spherical flame tends to accelerate due to the supplied excess energy. Therefore, the critical radius where this effect diminishes should be determined and the flame radius data before that critical point should not be used in the flame speed calculations. Electrodes providing the spark should be sharp and thin enough to avoid disturbing the flame front. Since the flame is stretched, there are errors caused by the extrapolation process to zero stretch. For the constant pressure method, it is important to check that the pressure rise is minimal during the experiment [43]. It is reported in the literature that only 1/3 of the chamber radius should be used to prevent the influence of the pressure rise even when using the constant pressure method [51].

For the scope of this thesis, the spherical flame propagation method is selected with the constant volume spherical combustion chamber approach.

2.3 Measurements of Methane/Air and Methane + Hydrogen/Air laminar flame speeds in the Literature

Laminar flame speeds of methane (which is the primary component of natural gas) and air premixtures are widely studied in the literature by using the techniques presented in the previous chapter. Most of the experiments are performed at atmospheric pressure and in room temperature. Van Maaren and de Goey's [52] numerical demonstration that flame stretch due to flame front curvature and/or flow divergence must be considered in laminar flame speed calculations, marked as a major breakthrough. Today, thanks to advances in measurement methodologies that consider the effect of flame stretch and the use of more accurate and reliable experimental devices (digital flow meters, pressure, and temperature sensors), the experimental data on laminar burning velocities of methane/air mixtures present a better coherence between various experiments [34].

The effects of hydrogen addition on the flame propagation of methane-air mixtures are also studied in the literature. Yu et al. [53] found that the flame speed of methane

and propane mixtures with hydrogen addition was proportional to the hydrogen concentration. Halter et al. [7] used the constant volume spherically propagating method to investigate laminar flame speeds at both atmospheric and elevated pressures. It is found that hydrogen addition to methane-air laminar flames increases the flame propagation speed and decreases the flame front thickness., It is also found that pressure has the opposite effect, reducing flame speed and thickness. Hu et al. [48] conducted both experimental (CVM) and numerical simulation studies on the combustion characteristics of premixed methane-hydrogen-air laminar flames for a wide range of hydrogen addition rates (0-100%). Numerical simulation results indicated that the flame speed increased quasi-linearly when the hydrogen molar concentration was below 40%, but exponentially at higher concentrations. Hermanns et al. [39] and Dirrenberger et al. [54] studied the effects of various hydrogen addition rates on methane-air mixtures flame speeds using the heat flux method. Tang et al. [55] reported that the addition of hydrogen to flames impacts flame speed through thermal, kinetic, and diffusion effects. Their sensitivity analysis indicated that the kinetic effect was the most significant, followed by the thermal effect, with the diffusion effect being the least significant.

2.4 Modelling of Laminar Premixed Flames

Combustion modelling involves the use of mathematical and computational models to predict and understand the behaviour of chemical reactions during the combustion reaction processes. This includes predicting the temperature and concentration profiles of species, and the flow characteristics of the reacting gases. Laminar premixed flame modelling is performed by solving the Navier-Stokes equations numerically, with the inclusion of species transport equations and the chemical source term to the energy equation. Detailed information about the equations and derivations can be found in [56].

1D flame modelling is widely used in the literature since it gives information about basic flame characteristics with low computational costs. In this work, two distinct

1D codes, namely CANTERA and CHEMKIN-PRO are used. To obtain 1D flame speeds of various mixtures at different conditions, CANTERA is preferred. CHEMKIN-PRO is used to obtain initial flame conditions for our 2D laminar flame calculations, which are described in detail in Chapter 4.2. For the computation of detailed transport properties, the pre-processing tool of CHEMKIN-PRO is used.

CANTERA models 1D laminar flames by stabilizing an axisymmetric flame front in a stagnation flow configuration and computes the solution along the stagnation streamline (r=0) [57]. To do that, similarity solution is used for reducing 3D governing equations to 1D. Governing equations for a steady axisymmetric stagnation flow. CHEMKIN-PRO computes a 1D laminar flame with uniform inlet conditions. Only continuity, energy, species and ideal gas equations are solved using implicit finite difference methods [58].

For the calculation of the net chemical production rates, the widely used Arrhenius approach is implemented by both software. Additionally, both of them are capable of modelling transport phenomenon by utilizing mixture-averaged multicomponent transport properties.

CHAPTER 3

EXPERIMENTAL METHODOLOGY

3.1 Experimental Setup Design

In this work, laminar flame speed experiments are performed using the spherical expanding flame method with constant volume. For this purpose, a spherical combustion chamber, which is designed to maintain high initial pressures and temperatures, is manufactured and assembled. The experimental setup consists mainly of the spherical combustion chamber, the gas feeding/exhaust system, and the optical diagnostics. Each of them are explained in detail in this chapter. Fig. 3.1. shows a comprehensive global layout of the experimental setup.

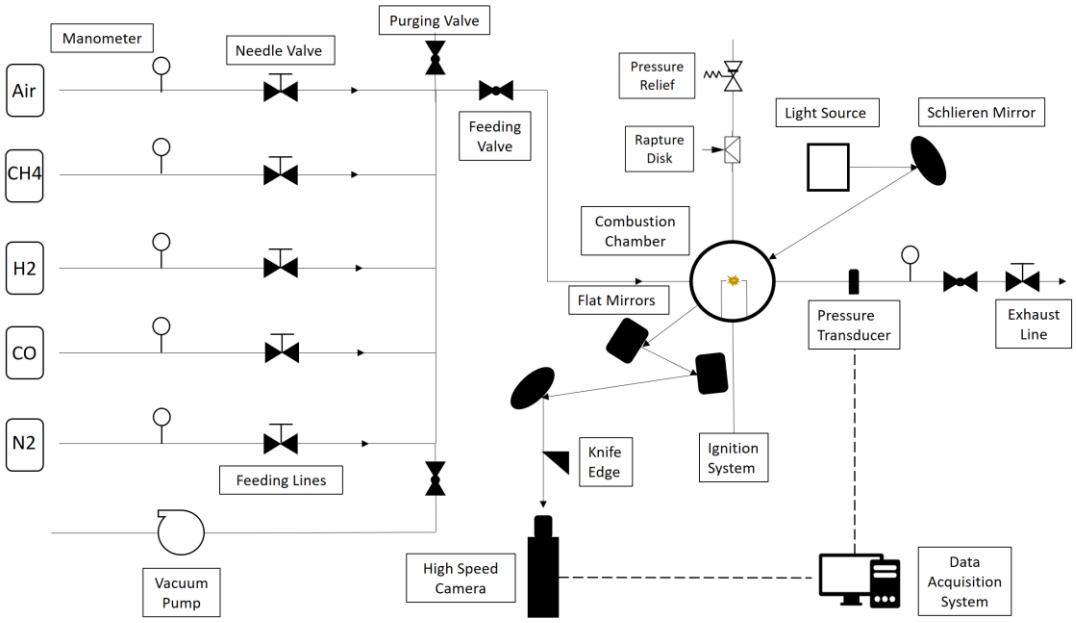

Figure 3.1. General layout of the experimental setup

3.1.1 Spherical Combustion Chamber Design

The high-pressure chamber has been designed to sustain combustion with a maximum initial pressure up to 15 bars. Considering the maximum expansion ratio attainable with classical hydrocarbon fuels (~8), the combustion chamber has been designed to support pressures up to 120 bars. The high-pressure enclosure is machined from of a stainless steel (AISI304) cube with 235 x 235 x 235 mm^3 external dimensions. Three holes, 108 mm in diameter, were machined in this cube, thus releasing a volume of 3.5 litres.

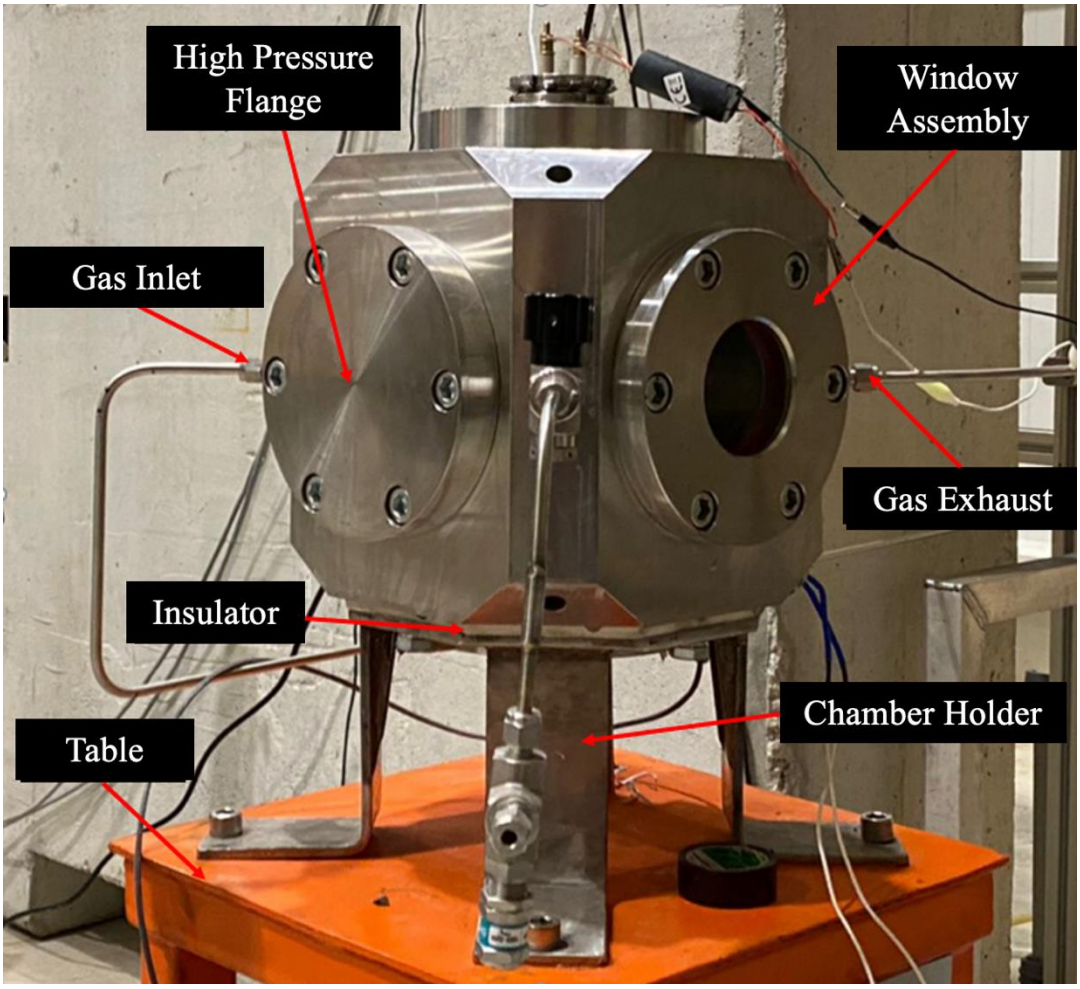

Figure 3.2. Spherical combustion chamber assembly

The eight ports of the combustion chamber are closed by high pressure flanges. Six spot-faced holes are drilled and M12 screws are used for the assembly. The sealing of the unit is ensured by an O-ring made from Fluorocarbon elastomer (FKM).

Two of the eight ports available are closed by high-pressure glass windows, allowing the visualization of the propagating flame. The window assembly consists principally of a thick glass window, a flange holder and some small parts dedicated to sealing and maintaining. The sealing between the unit and the high pressure enclosure is ensured by the same O-ring used in the other flanges. Concerning the sealing of the glass window and his support, 2 facing seals are disposed on each side Eight screws (M4x0.7) are used for enclosing the glass. Windows are placed face to face on the chamber to provide optical access. The thick glass windows are made from quartz cylinders with an outer diameter of 82 mm and 60 mm in thickness. These windows are chosen to sustain pressures up to 300 bars and an operational temperature of 200°C. The available optical diameter is 70 mm.

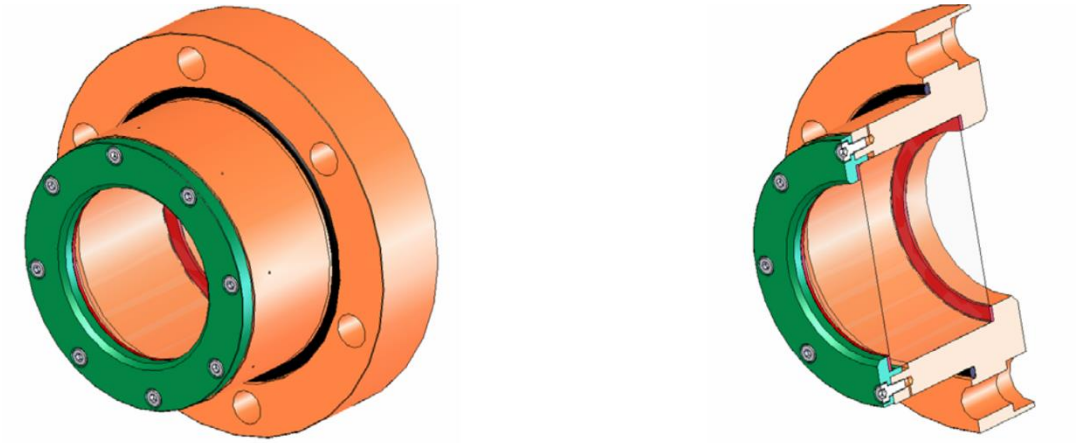

Figure 3.3. Windows assembly

The ignition flange system is placed on the top hole of the combustion chamber. It has 3 main components: the high pressure flange (similar to other flanges but with a

hole), the tight passage for the isolator, and conductors / electrodes for ignition. The tight passage is a machined piece in aluminium alloy, which supports two isolator tubes. The isolator tube is made from PEEK polymer, which gives the required electrical high voltage insulation. The sealing is achieved by using a FKM O-ring, placed between the flange and the tight passage. A small flange is used to compress and maintain the assembly.

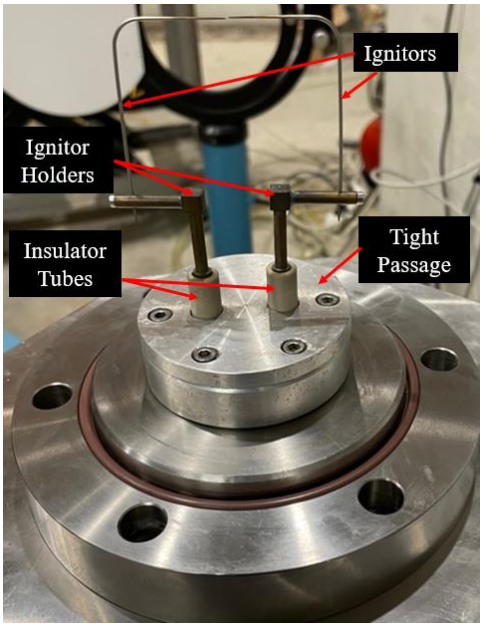

Figure 3.4. Ignition flange system

Two conductor elements made from brass are used to ensure the high-voltage connection between the electrodes inside the chamber and the high voltage cables outside. The connection with the high-voltage cables is made by a thread (M4) at one end. The connection with the electrodes is ensured by tightening screws from the sides. The electrodes made from Tungsten wires with 1mm diameter and 90 mm length are curved (90°) and the short end is tapered to 100 µm diameter. One important parameter of the ignition efficiency is the distance separating the two tapered electrodes. Spacing distance is set to 0.8 mm after some experiments to ensure repeatable ignition conditions. To achieve mixture ignition, an arc generator is placed between the electrodes and a DC source is used. The arc generator enhances

the voltage supplied from the DC source to create a spark powerful enough to ignite the mixture. A manual switch is used to give power to the DC source.

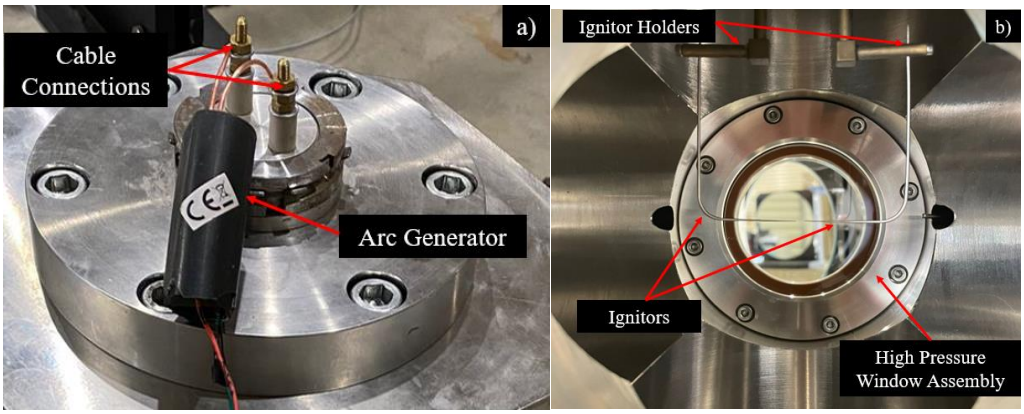

Figure 3.5. a) Cable connections for the ignitors and arc generator b) Ignitors and ignitor holders placed inside the chamber

Connecting elements are based on two ferrules mounting system. In this system, the front ferrule creates a seal against the fitting body and on the tubing outside diameter. As the nut is turned, the back ferrule axially advances the front ferrule and radially applies an effective tube grip. Inlet and outlet flows use tubes of 6 mm outer diameter and 4 mm inner diameter. The connecting elements have a tube fitting of 6 mm OD at one side and a 1⁄4" male NPT for the other side. The inlet and outlet ports are diametrically disposed around the vessel.

Two thermocouples (± 0.5K accuracy) are connected to the combustion chamber. One is flash mounted to the combustion chamber using one of the free ports on the chamber, to measure the temperature of the gas mixture inside the chamber. Sealing is ensured by a seal-gland. The other thermocouple is welded on the chamber for surface temperature monitoring.

The last free port is dedicated to the safety devices of the experiment. A rupture disk and a pressure relief valve are connected to this port. The pressure relief valve opens if the pressure inside the chamber exceeds the design condition (150 bar) and releases

the chamber pressure continuously to keep the inside pressure at this condition. The rupture disk bursts and releases the pressure inside the chamber immediately if the pressure inside the chamber exceeds 300 bars.

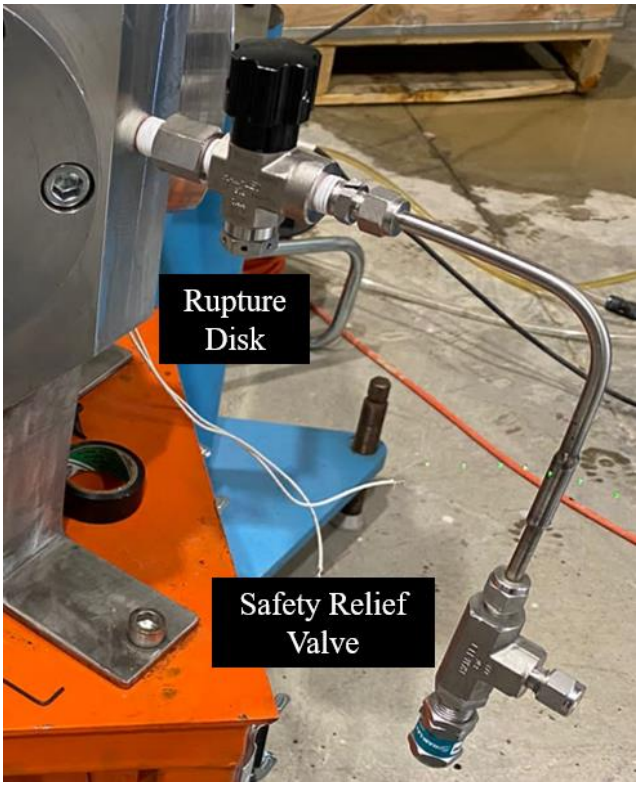

Figure 3.6. Safety elements connected to the combustion chamber

The pressure vessel assembly is supported by a chamber holder. In order to limit the heat conduction from the warm chamber to the experimental table, a flat insulator made from ceramic is used between the bottom of the combustion chamber and the support. The table is designed to match the height of the Schlieren visualisation system mirrors. Wheels are mounted to the table to ease its movements.

3.1.2 Gas Feeding/Exhaust System

There are five different gas lines, for Air, CH_4, H_2, CO and N_2 and all the gases are supplied from pressurized tanks (Fig. 3.7) to the gas lines with flexible hosepipes. A needle valve is located on each line. With these needle valves, the desired gas amount can be supplied to the combustion chamber. For purging the gas line after each experiment, a globe valve is used. Two globe valves are located before and after the combustion chamber. The first one is for the feeding of the combustion chamber and second one for the exhaust line. A vacuum pump is connected to the feeding line to obtain vacuum conditions in the combustion chamber before each experiment. Gases are introduced into the combustion chamber with respect to their partial pressures, from the lowest to the highest to obtain the desired reactive mixture composition. A pressure transducer is used to read the pressure value inside the combustion chamber. After each experiment, the gas lines are purged with N_2 (See Figs. 3.8 and 3.9).

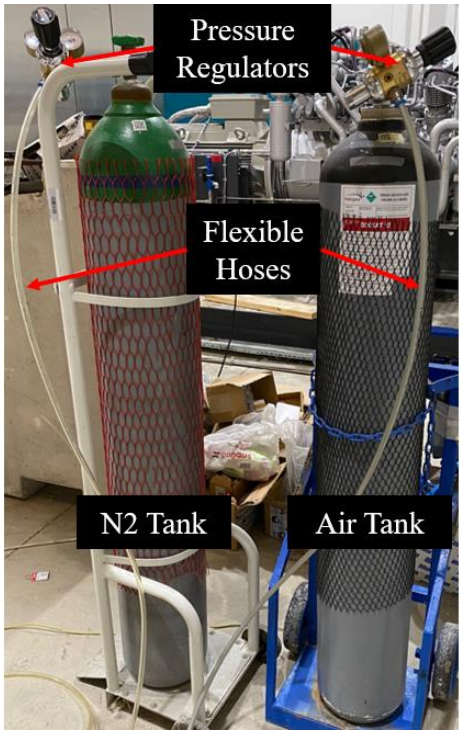

Figure 3.7. N_2 and air tanks

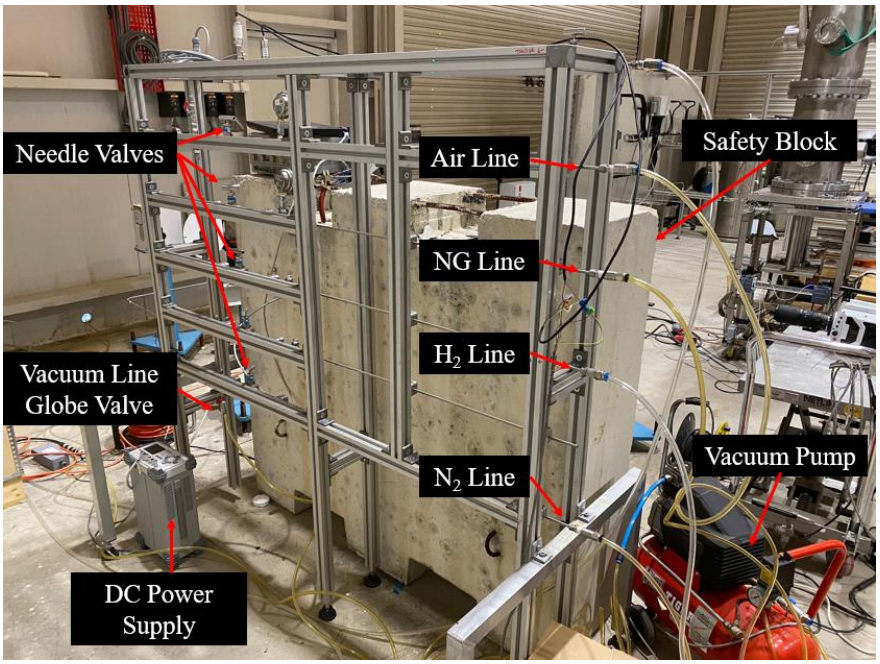

Figure 3.8. Gas feeding/exhaust system seen behind the protection concrete wall (safety block)

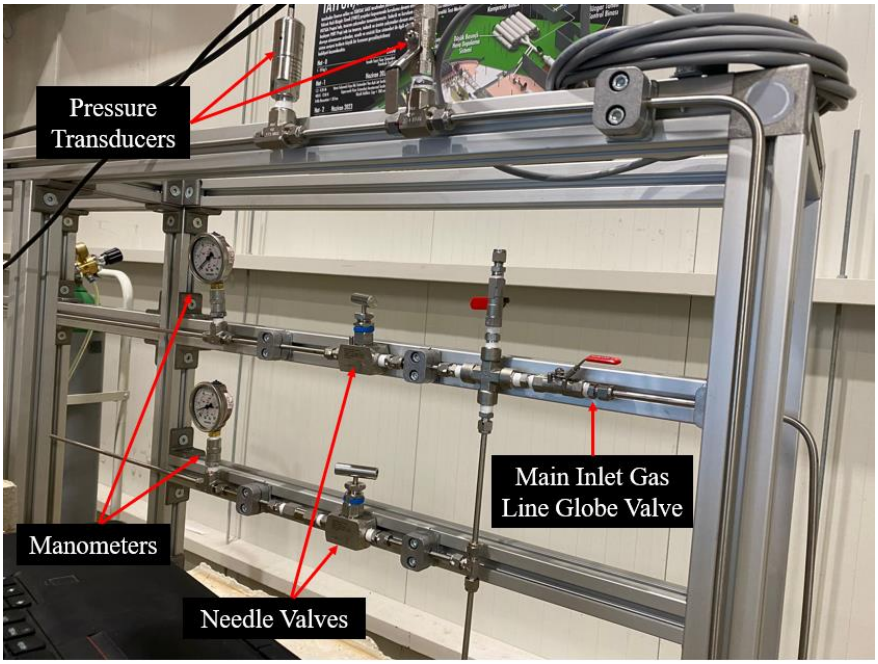

Figure 3.9. Gas feeding/exhaust system, close up view

3.1.3 Optical Diagnostics

The Schlieren visualisation method is used to observe the spherical flame propagation process (Fig. 3.10). In this method, the point light source is parallelized using a spherical mirror and sent to the experimental setup. After the light passed from the experimental system observation windows, it is focused with the help of a second mirror. At the focal point of the second mirror, a knife edge is placed. The purpose of the knife edge is to block the part of the light coming from the mirrors and decreasing the light intensity. This blockage is named as "cutoff" [59,60]. With this method, it is possible to capture the density differences introduced by the presence of the flame front. Light waves are deflected as they pass through a non-constant density field. If these light waves are deflected towards the knife edge, darkened sectors can be observed in the image. If the light is deflected away from the knife edge, brighter images are created at the non-constant density zones.

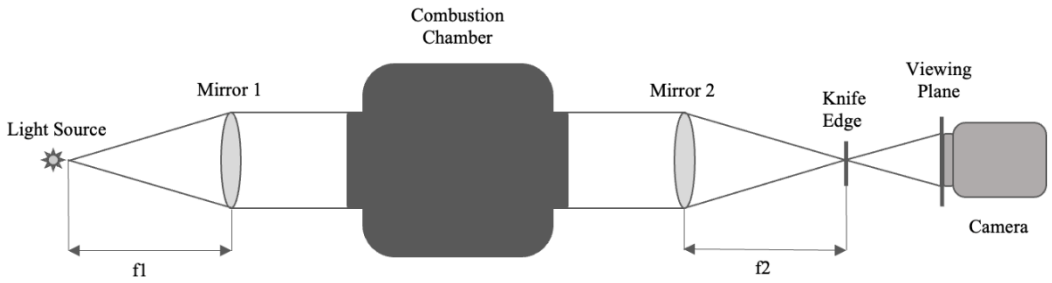

Figure 3.10. Basic Schlieren imaging setup

Fig. 3.11 shows the experimental setup where Schlieren mirrors and flat mirrors can be seen. The height of the midpoints of mirrors and observation windows are set to 85cm from ground. Due to available limited area in the experiments room, two flat mirrors are used reflecting the image to Schlieren mirrors. Normally, focal points of the used Schlieren mirrors are at 2m but with the help of a flat mirrors, this distance is reduced to 1m between the light source and the flat mirror and to 1m between the

flat mirror and the first Schlieren mirror (f1). The same procedure applies also for the second Schlieren mirror and the knife edge (f2).

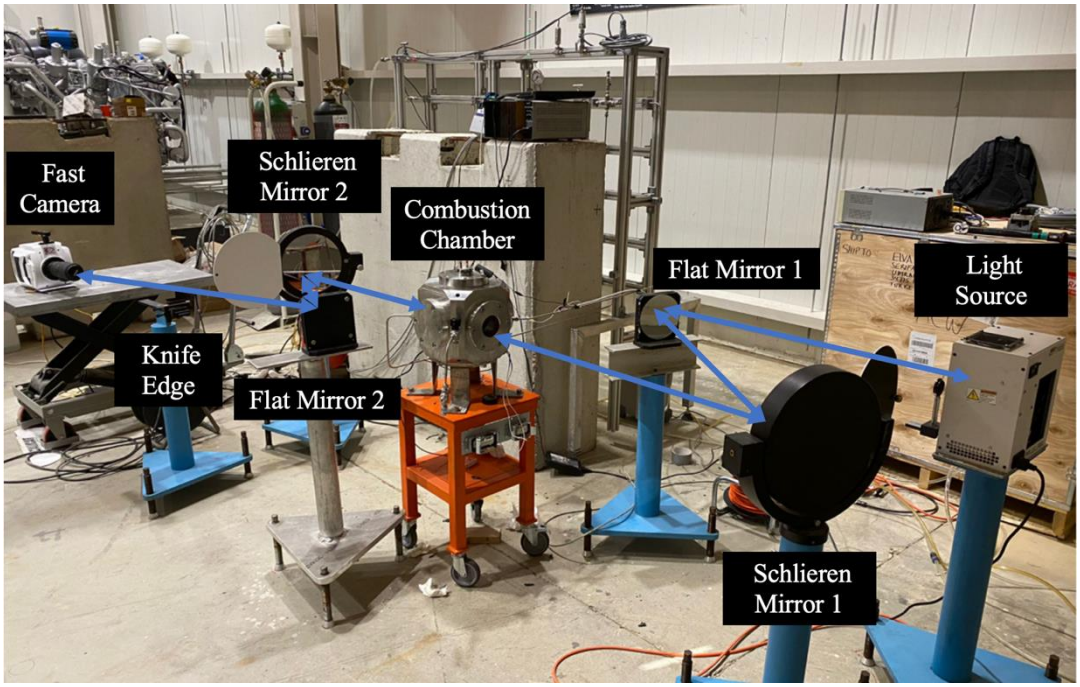

Figure 3.11. Experimental setup and the Schlieren system

A high-speed camera (Phantom) with 24000 fps and 768x576p resolution is used to collect the flame propagation images. A Nikkor 200mm f/4D IF-ED camera lens is mounted on the high-speed camera. The distance between the camera lens and the knife edge is set to 80cm. Collected images are transferred to the computer.

Figure 3.12. High speed camera with lens

3.1.4 Experimental Procedure

The procedure applied to each experiment is explained step by step in this section. This procedure follows the steps listed below:

1. Globe and needle valves are checked if they are in closed position.
2. Manometers on the line are checked to check if there is any pressurized gas in the line (only for the first experiment).
3. Main feeding globe valve is opened.
4. Vacuum line globe valve is opened, and vacuum pump is started.
5. After reaching the vacuum limit (between 5kPa-8kPa depending on the room temperature), the vacuum line globe valve is closed, and vacuum pump is stopped.
6. Pressure inside the combustion chamber is checked from the computer using the pressure transducer and the determined partial pressure of hydrogen is added to this value. Hydrogen is introduced into the combustion chamber by opening the needle valve slowly. When the calculated pressure is reached, the valve is closed.
7. Step 6 is applied for the natural gas feeding line.
8. Step 6 is applied for air until total pressure value is reached (for the scope of this thesis 100kPa).
9. Main feeding globe valve is closed.
10. Ignition is triggered and at the same instant camera recording is started.
11. Combustion products are exhausted by opening both valves at the exhaust line.
12. Chamber is purged with N2 and prepared for the next experiment.

Fig. 3.13. shows the data acquisition system. Partial pressure values are adjusted according to the value read from the computer. A Kistler 4260A pressure transmitter with ±0.4% accuracy is used to measure partial pressures inside the chamber.

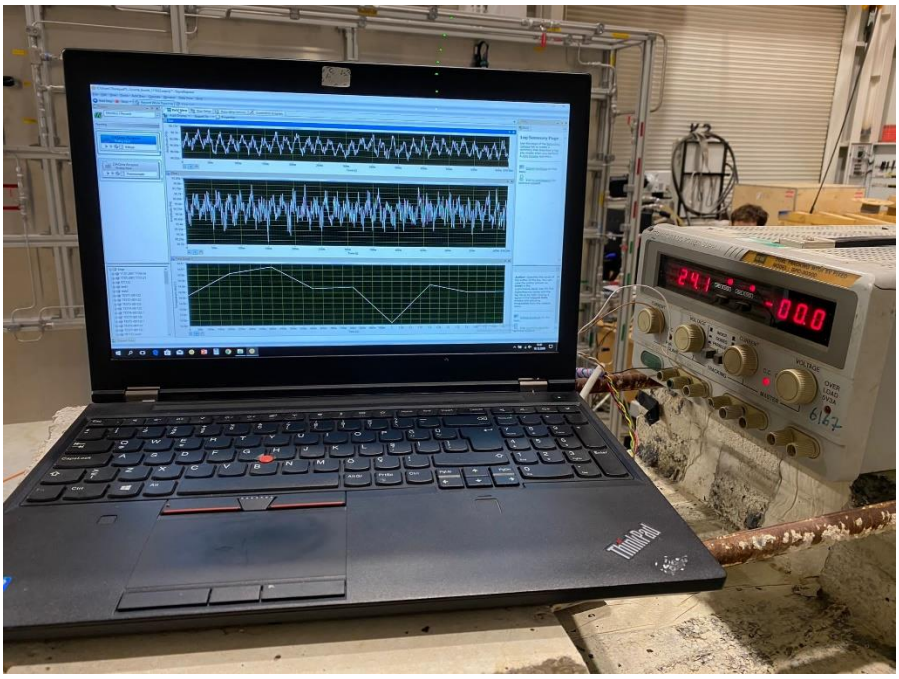

Figure 3.13. Data acquisition system

Hydrogen addition rate to the fuel is calculated based on Eq. 3.1, where X represents the molar fractions of the individual species.

$$H_2\ addition\ rate\ (\%) = \frac{X_{H_2}}{X_{H_2} + X_{CH_4}} \tag{3.1}$$

The global chemical reaction for the reactant side is given in Eq. 3.2:

$$\left(\frac{100 - \%_{H_2}}{100}\right) NG + \left(\frac{\%_{H_2}}{100}\right) H_2 + \left(\frac{N_{Oxi}}{\Phi}\right) (O_2 + 3.76\, N_2) \tag{3.2}$$

N_{Oxi} represents total number of oxidizer moles (in this case O_2) to complete combustion of the fuel ($NG + H_2$) blend and is calculated as:

$$N_{Oxi} = x + \frac{y}{4} \tag{3.3}$$

where x is the total number of carbon atoms in the fuel and y is the total number of hydrogen atoms in the fuel.

In this work, the experiments are performed by calculating the partial pressures of the mixture by assuming that only CH_4 is present in the NG mixture since the company could not provide the exact composition of the mixture. After the experiments are performed, natural gas mixture composition is determined using the gas chromatography method. The analyses are performed at the METU Chemical Engineering Department and the mixture species, and their molar compositions are presented in Table 3.1. Species with carbon number higher than 3 (such as C_4H_{10}, C_5H_{12}, C_6H_{14}) are added to the C_3H_8 composition assuming that their effect will be negligible (total of % 0.3).

Table 3.1 Natural Gas Mixture Species and Their Molar Composition (%)

Gas Mixture	Molar Composition (%)
CH_4	88.75
C_2H_6	9.65
C_3H_8	1.60

The partial pressure values calculated using the actual gas compositions for the experimental matrix are given in Table 3.2. The presented values are calculated for a total initial pressure of 100kPa. Differences of partial pressures of the actual NG-air and CH_4-air mixtures are also presented in the table. We assume that the changes of the mixture equivalence ratio occasioned by these actual partial pressure values are not significant enough to modify our main experimental results. This is because of the uncertainties caused by the partial pressure measurement inaccuracies, as shall be highlighted in results section 5.1.

Table 3.2 Partial pressures of the experimental matrix

Equivalence Ratio	*Mixture composition [mol %]*		*Partial Pressures [kPa]*	
	CH_4/NG	*H_2*	*CH_4 / NG*	*H_2*
0.6	100	0	5.95 / 5.3	0
	90	10	5.76 / 5.28	0.64 / 0.59
	80	20	5.54 / 5.09	1.39 / 1.27
0.8	100	0	7.78 / 7.12	0
	90	10	7.52 / 6.91	0.84 / 0.77
	80	20	7.22 / 6.65	1.81 / 1.66
1	100	0	9.54 / 8.75	0
	90	10	9.21 / 8.47	1.03 / 0.95
	80	20	8.83 / 8.14	2.21 / 2.04

3.2 Laminar Flame Speed Determination from the Experiments

3.2.1 Image Processing

After the video images are collected from the high speed camera, flame radius values are extracted by fitting an ellipse on the flame front for each frame. This image processing is performed by a python code, with the help of the openCV extension. The code is given in Appendix A. Firstly, the 70mm diameter observation area should be defined in the algorithm. Then, dimensions of each pixel are estimated in order to calculate the real radius. After the pixel ratio is obtained, the image is converted to a grayscale. The goal is detecting the flame front and fitting an ellipse onto it. To do this, the background image is subtracted from each image using a background subtractor (MOG2). The history of background subtraction is adjusted to obtain a decent flame front extraction. After the background subtraction, the image is threshold, blurred and edge detection is applied on the modified image. Then using the coordinates of these edges, an ellipse, which is more general form of a circle, is fitted to the flame front. Since the flame front is mostly circular, ellipses correspond actually to circles. But, when there are disturbances on the images (for example due to ignitors), instead of fitting a circle on the flame front with an important error rate, an ellipse is fitted and the code generates an average radius.

The number of points on the ellipse is set to 100. The average radius is obtained by averaging those 100 points on the ellipse. Figs. 3.14a-b show flame propagation images, where an ellipse fitted on the flame front using only 10 points in order to simplify the image to explain the post-processing process. Time and radius values are stored for post-processing the results.

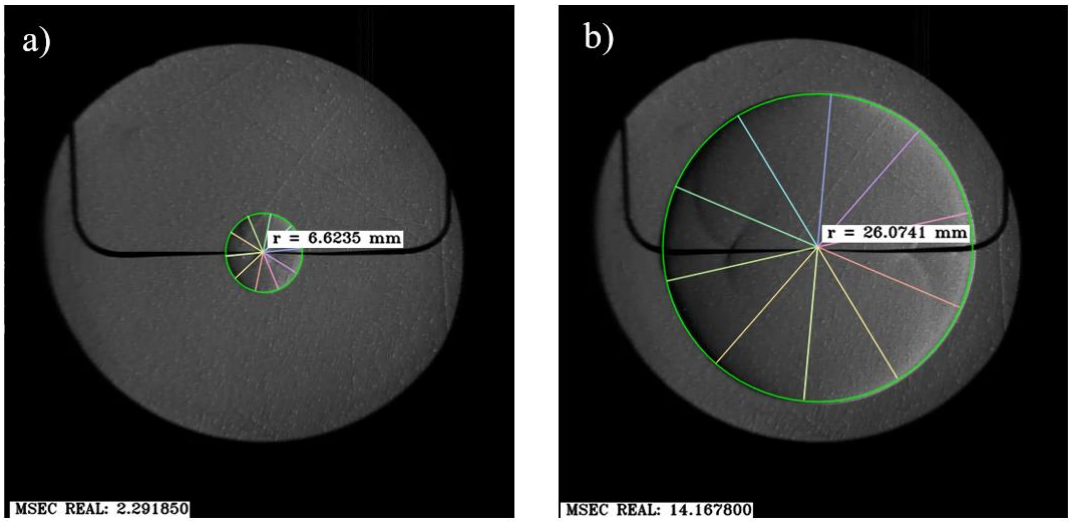

Figure 3.14. Instants of postprocessing for Φ= 0.8 NG/Air premixture with ellipses fitted at 10 points after a) 2.29 ms from ignition b) 14.17 ms from ignition

3.2.2 Laminar Flame Speed Calculations

From the instantaneous images of the flame front, using the approach of Clavin and Joulin [61], the stretched laminar flame burning velocity Vs can be obtained as the time derivative of the flame radius (Rf).

$$V_s = \frac{dR_f}{dt} \tag{3.4}$$

We use the flame stretch definition given in section 2.1.3 (Eq. 2.1), where the flame element area is defined as the set of points which are located on the flame surface and has the same normal velocity as the flame surface. For the spherically expanding flame case [62,63]:

$$A = 4\pi R_f^2 \tag{3.5}$$

and hence

$$K = \frac{8\pi R_f}{4\pi R_f^2}\frac{dR_f}{dt} = \frac{2}{R_f}\frac{dR_f}{dt} = \frac{2V_s}{R_f} \tag{3.6}$$

where K is the stretch rate, due to strain and curvature acting on the flame surface. Markstein [25] proposed a relationship between stretched and unstretched burning velocities, using the flame stretch concept. If the spherical flame thickness is assumed as infinitesimally thin and weakly stretched, for a unconfined and quasi-stable flame, the unstretched laminar burning velocity can be found using the Markstein length concept. In this case, a linear theory relates the stretched laminar flame burning velocity to unstretched laminar flame burning velocity, using the Markstein length concept and the flame stretch. This method is considered to be accurate for moderate curvature and strain rates, as mentioned in Chapter 2.1.3.

$$V_s = V_s^0 - LK \tag{3.7}$$

V_s^0 stands for the unstretched laminar flame burning velocity and L is the Markstein length. The unstretched laminar flame speed (S_L^0) can be obtained using the expansion ratio $\sigma = \frac{\rho_u}{\rho_b}$ where ρ_u is the unburned gas density and ρ_b is the burned gas density:

$$\frac{V_s^0}{S_L^0} = \sigma \tag{3.8}$$

3.2.3 Determination of the Stretched Laminar Flame Burning Velocity

In order to obtain the laminar flame speed, the first step is to determine the stretched laminar flame burning velocity (V_s) from the temporal flame front evolution data. The raw data acquired from the image-processing step cannot be used directly to determine $\frac{dR_f}{dt}$ due to experimental noise. In the literature, there are different methods for the extraction of the flame burning velocity. They can be classified as the polynomial fitting method, the analytical method first used by Taylor et al. [64-65] and the differential equation fitting method proposed by Tahtouh et al. [66]. In this work, first and third method are considered and explained below.

3.2.3.1 Polynomial Fitting Method

The polynomial fitting to the raw temporal radius evolution data, is intensively used in the literature [7, 67-69] for the extraction of the stretched flame burning velocity of spherical flames. In this method, polynomial functions with different orders are fitted to the raw data. The differentiation of the used polynomial with respect to time gives the stretched flame burning velocity. Degrees of suggested polynomials changes between 2nd order and 4th order. Halter [7, 67] used a 4th order fit, Kelly and Law [68] suggested 2nd order fitting and Tahout et al. [66] mentioned that higher than 3rd order polynomials introduce more noise. Although the deviations between the raw radius data and the fitted curves are relatively small, differentiation of this polynomial introduces additional errors influencing the laminar flame speed calculations. Also, the selection of the radius data interval modifies the results tremendously [66].

In figures 3.15 and 3.16 below, deviations between different orders of polynomial fittings are presented for NG/air mixture at Φ= 0.8. Fig. 3.15. illustrates V_s vs Time variations derived from different order of polynomial fittings. 2nd order gives nearly linear relation where 4th and 5th order gives polynomial profiles. This is expected since these are first derivatives. Fig 3.16. illustrates V_s vs Stretch rate variations for

the same fittings. For the second order fitting case, data deviates from linearity strongly. 5th order case underestimates the V_{S0}. For this case (Φ=0.8 NG/Air), the best fit is for the 4th order fitting.

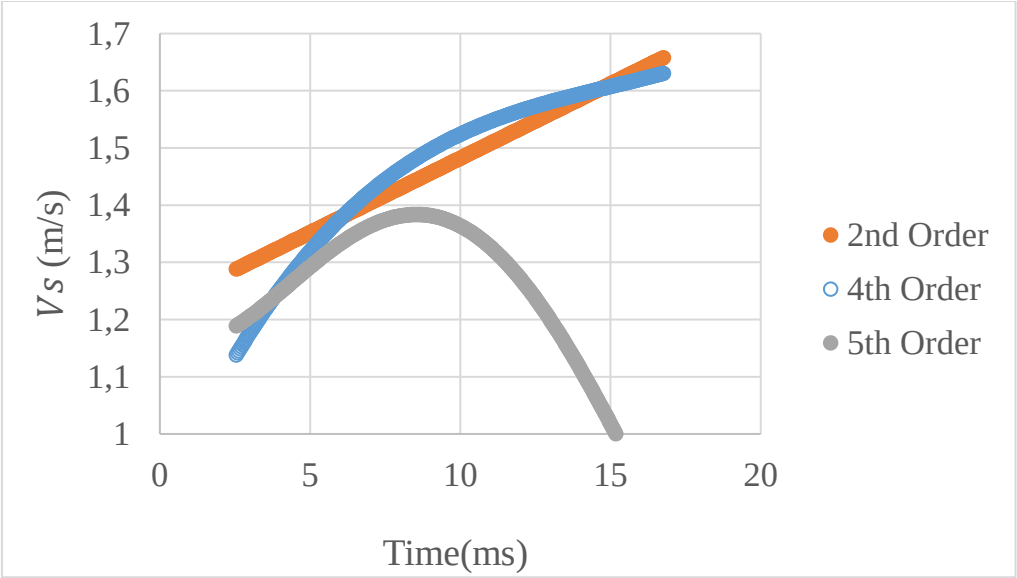

Figure 3.15. V_s vs Time for different orders of polynomial fittings

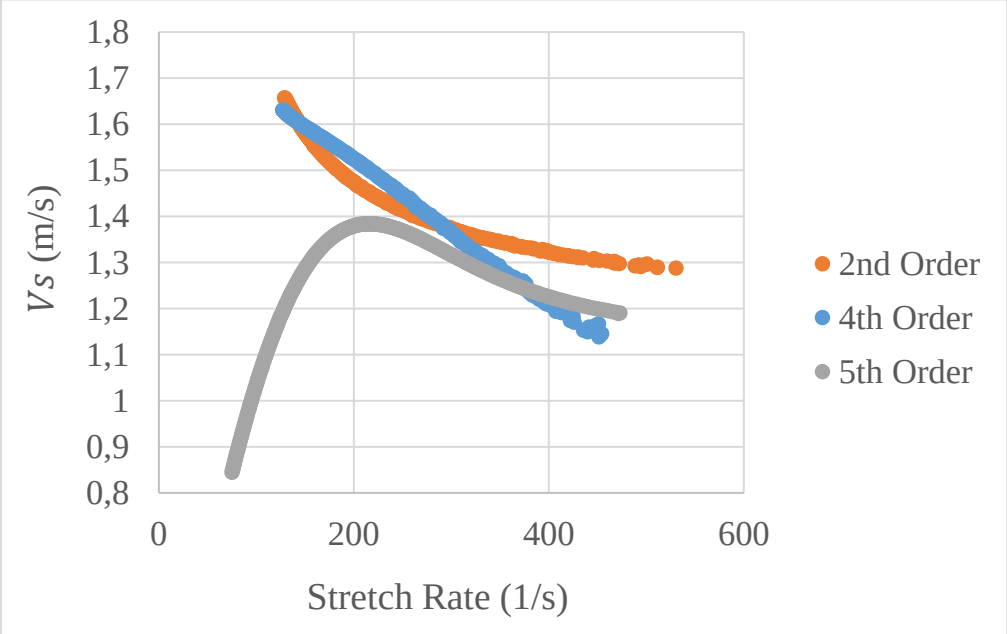

Figure 3.16. V_s vs Stretch Rate for different orders of polynomial fittings

3.2.3.2 Differential Equation Fitting Method

This methodology is introduced by Tahout et al. [66] based on the exact differential solution of the combinations of Eq. 3.9 and 3.10. We follow here the developments given in this reference that should be consulted for more details.

$$\frac{dr}{dt} = V_{S0} - 2L_b \frac{dr}{rdt} \tag{3.9}$$

Using the definition of the Lambert W function [66], the solution of Eq. 3.9 becomes:

$$r(t) = 2L_b W_0(Z) \tag{3.10}$$

where Z is:

$$Z = \frac{e^{\frac{V_{S0}t + C_1}{2L_b}}}{2L_b} \tag{3.11}$$

C_1 is a constant to be determined and W_0 is the principal branch of the Lambert W function, which is defined as the inverse function of Eq. 3.12.

$$f(W) = We^W \tag{3.12}$$

From the definition of W [66],

$$\frac{dW}{dZ} = \frac{W(Z)}{Z\big(1 + W(Z)\big)} \tag{3.13}$$

for $Z \neq \frac{-1}{e}$ and $W(Z) \neq -1$.

$W_0(Z)$ is a positive real number if L_b > 0 and Z > 0. So that, L_b, V_{S0} and C1 can be obtained minimizing Eq. 3.14.

$$\sum_{1}^{N}(r_{raw}(t) - r(t))^2 = \sum_{1}^{N}(r_{raw}(t) - 2L_b W_0(Z))^2 \tag{3.14}$$

After minimization is performed and unknowns are obtained, V_S can be found by the differentiation of Eq. 3.10. with respect to time. This method reduces errors linked to differentiation of polynomial fits [66]. The minimization process is performed by writing a MATLAB script, which is given in Appendix B. The downside of this method is that the initial guesses for unknowns are important, and they impact the results. A set of results are presented inFig.3.17 – 3.19 for the same NG/air mixture at Φ = 0.8.

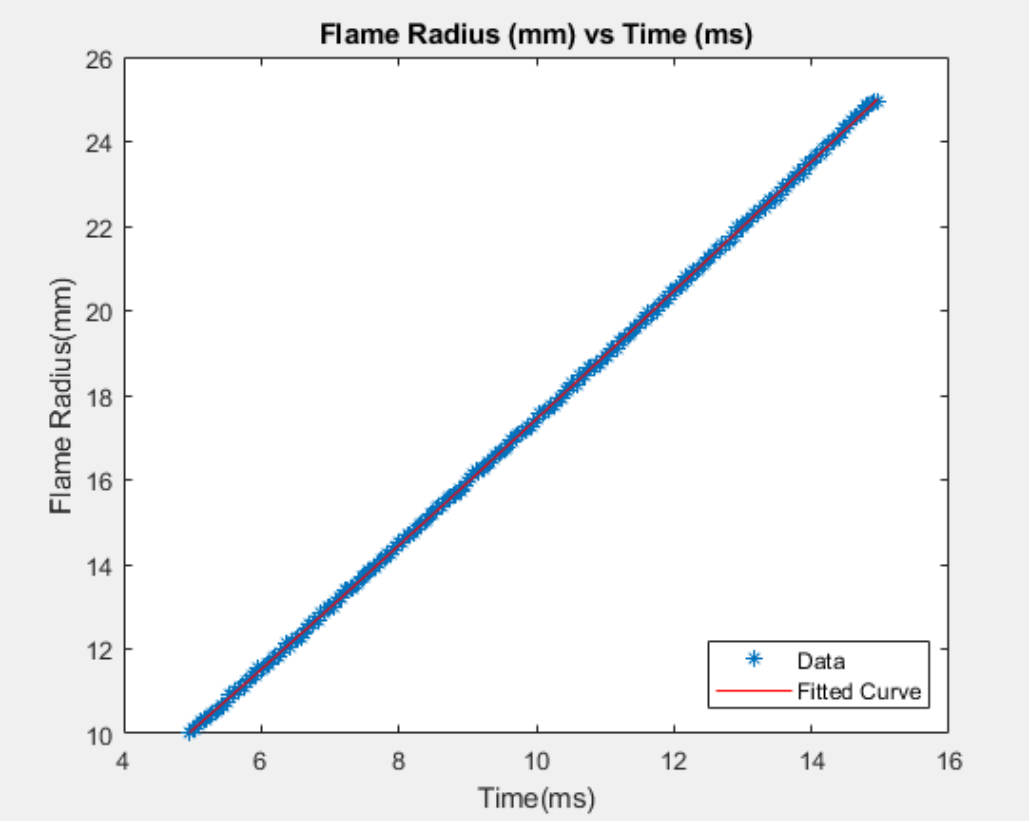

Figure 3.17. Flame radius vs Time (ms) graph, temporal radius data and the fitted curve

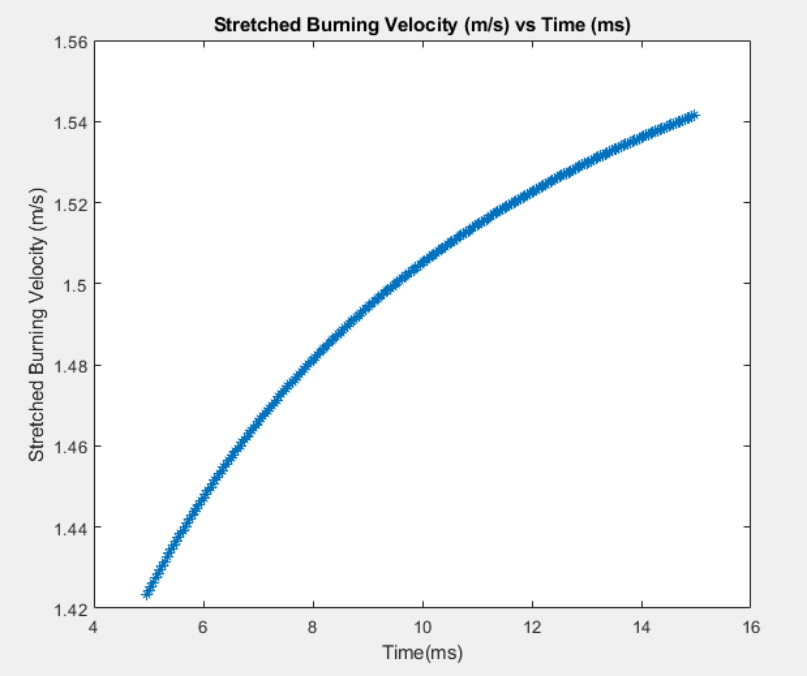

Figure 3.18. Stretched Burning Velocity (m/s) vs Time (ms) graph, V_s calculated by the differentiation of Eq. 3.10

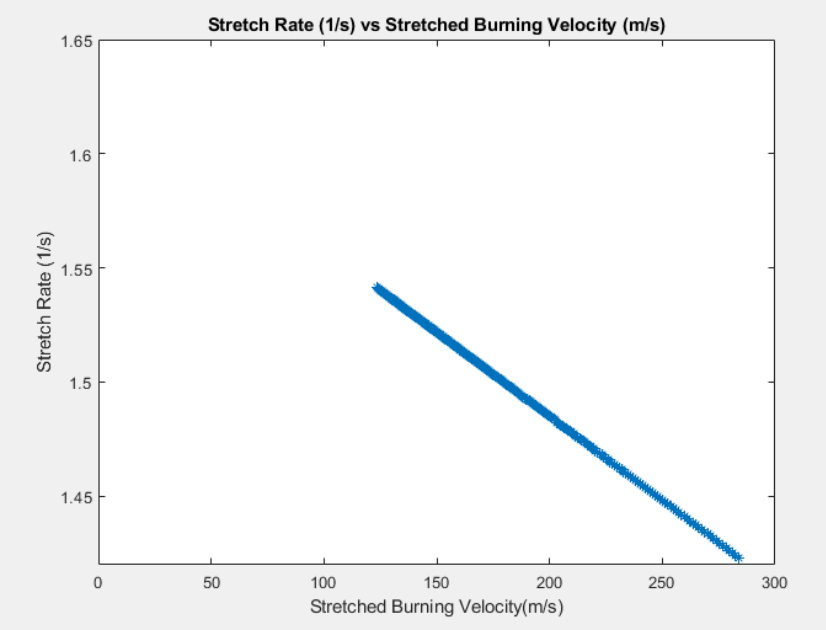

Figure 3.19. Stretch Rate (1/s) vs Stretched Burning Velocity (m/s) graph, with the stretch rate calculated using Eq. 3.6

CHAPTER 4

NUMERICAL METHODOLOGY

4.1 Numerical Modelling

For the numerical part of this work, the open source OpenFOAM finite volume method based computational fluid dynamics software is used. Currently OpenFOAM has no built-in reactive flow solver with multicomponent diffusion. The most common built-in reactive flow solver for premix mixtures “reactingFoam” employs the transport equations under the assumption of Le=1 and Sc=1. This may be suitable for RANS or LES simulations of turbulent combustion, when molecular diffusion is weak compared to turbulent diffusion. However, this assumption is not acceptable for the reaction-diffusion processes, such as the propagation of a laminar flame, and especially when hydrogen is present in the mixture. Thus, transient, compressible reacting flow solver 'reactingDNS' developed by Zhang et al. [70-71] on OpenFOAM is used to compute laminar flame simulations. This solver is equipped with an integrated multicomponent species transport model. The finite volume solver utilizes the PIMPLE [72] algorithm, which is a combination of the PISO (Pressure Implicit with Splitting of Operator) and SIMPLE (Semi-Implicit Method for Pressure-Linked Equations) procedures. The reaction terms are estimated using a simplified GRI-Mech 3.0 mechanism consisting of 218 reactions involving 36 species [73]. The Tabulated Dynamic Adapted Chemistry approach [74] treats chemical reactions by combining two run-time reduction techniques,

namely the In Situ Adaptive Tabulation [75] and the Dynamic Adaptive Chemistry [76]. In order to achieve a stable solution, an adjustable time step is used, restricting the maximum Courant number to 0.1. This results in a time step on the order of 10^{-6} seconds. N2 is the inert element used in computations.

4.1.1 Governing Equations

The governing equations employed by the solver are described in this section, in conservative form.

Continuity equation:

$$\frac{\partial \rho}{\partial t} + \nabla \cdot (\rho \boldsymbol{U}) = 0 \tag{4.1}$$

Momentum equation:

$$\frac{\partial}{\partial t}(\rho \boldsymbol{U}) + \nabla \cdot (\rho \boldsymbol{U}\boldsymbol{U}) = -\nabla p + \nabla \boldsymbol{\tau} \tag{4.2}$$

with the viscous stress tensor τ neglecting bulk viscosity

$$\boldsymbol{\tau} = \mu \left[(\nabla \boldsymbol{U} + \nabla \boldsymbol{U}^T) - \frac{2}{3} \nabla \cdot \boldsymbol{U} \boldsymbol{I} \right] \tag{4.3}$$

Energy Equation:

$$\frac{\partial}{\partial t}(\rho h_s) + \nabla \left(\frac{\rho}{\boldsymbol{U} h_s} \right) + \frac{\partial}{\partial t}(\rho K) + \nabla (\rho \boldsymbol{U} K) = \nabla \left(\frac{\lambda}{c_p} \nabla h_s \right) + \dot{R}_h + \nabla \left(\rho \sum_i^N \nabla h_{ki} \, \boldsymbol{J}_\iota \right) + \frac{\partial p}{\partial t} \tag{4.4}$$

where h_s is the sensible enthalpy, K is the kinetic energy, and $\dot{R}_h$ is the heat release term due to chemical reactions.

Species Transport equation:

$$\frac{\partial}{\partial t}(\rho Y_i) + \nabla \cdot (\rho \boldsymbol{U} Y_i) + \nabla \cdot (\boldsymbol{J}_\iota) = \dot{R}_\iota \tag{4.5}$$

$\dot{R}_\iota$ represents the reaction source term and the diffusion flux Ji contains only Fickian diffusion.

$$\boldsymbol{J}_\iota = -\rho D_i \nabla Y_i \tag{4.6}$$

where Di is the mass diffusivity of the ith species, calculated using the mole fractions (Xi), molecular weight (Mi) and binary diffusion coefficients (Ɗij) according to Eq. (4.7):

$$D_i = \frac{\sum_{i \neq j}^{N} X_j M_j}{M \sum_{i \neq j}^{N} \frac{X_j}{\mathrm{D}_{ij}}} \tag{4.7}$$

4.1.2 Detailed Transport Processes

A logarithmic polynomial fit is used for the calculation of mixture transport coefficients, using third-order polynomial coefficients [57]:

$$lnN_i = \sum_{n=1}^{n} a_{n,i} (lnT)^{n-1} \tag{4.8}$$

$$ln\mathrm{D}_{ij} = \frac{\left(\sum_{n=1}^{n} b_{n,ij}(lnT)^{n-1}\right)p}{p_{ref}} \tag{4.9}$$

In Eq. 4.8, N_i is the viscosity or the thermal conductivity of the i^{th} species and $a_{n,i}$ stands for the n^{th} polynomial coefficient of i^{th} species. p/p_{ref} is the mixture pressure to the atmospheric pressure ratio. $b_{n,ij}$ is the n^{th} polynomial coefficient of the binary diffusion coefficient of i^{th} species in j^{th} species. λ is the thermal conductivity of the mixture, which is calculated as follows:

$$\lambda = \frac{1}{2}\left(\sum_{i=1}^{N} X_i\lambda_i + \frac{1}{\sum_{i=1}^{N} X_i/\lambda_i}\right) \tag{4.10}$$

$\dot{R}_\iota$ is calculated using Arrhenius equations defined for each chemical reaction modelled in the reduced GRIMECH 3.0 mechanism. $\dot{R}_h$ is calculated using the $\dot{R}_\iota$ and h_i for species i.

4.2 2D Spherically Expanding Flame Modelling

Cross sectional area of the spherical combustion chamber is simplified as a 14 cm x 14 cm square to create a uniform hexahedral mesh system. In order to reduce the computational time, only the quarter of the cross-sectional area is modelled since flame propagates symmetrically. This simplification is validated by comparing the radius evolution of the full scaled domain with that of the quarter domain and no significant difference is found. Computational domain and the boundary conditions are given in Fig. 4.1. Freely propagating flames at atmospheric pressure and confined flames within the chamber at initially atmospheric pressure are modelled. For the freely propagating flame, velocity boundary condition is selected as zero gradient and the pressure boundary condition is set to wave transmissive in order to avoid reflection of pressure waves from the boundary. In the confined flame configuration,

outer boundaries are set to walls with no slip condition and zero gradient for pressure. For both cases, temperature is set to 300K at the boundaries. For the confined case, it is assumed that the inner wall temperature stays constant during the experiment. Bottom and left boundaries are set to symmetry condition for each case.

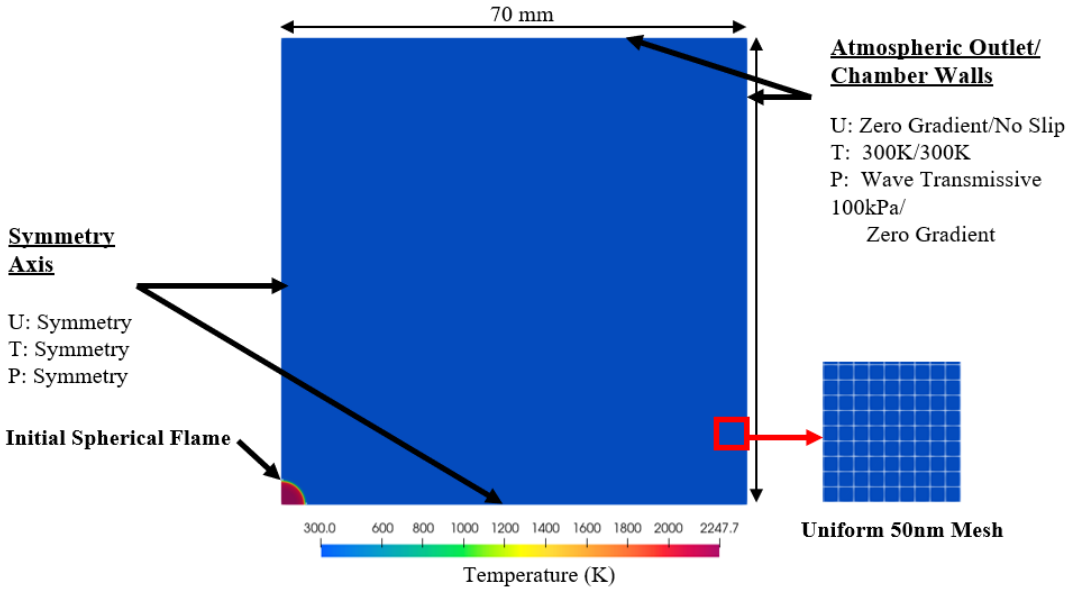

Figure 4.1. Boundary and initial conditions of the problem domain

For the initial conditions of species mass fraction and temperature values, a 1D flame is modelled using ANSYS CHEMKIN. Then, changes in mass fractions and the temperature with respect to distance is converted into a text file to be used in OpenFOAM. Using reactingDNS's built-in feature the 1D flame is extrapolated to the domain to obtain a circular flame with 3.5 mm initial radius. This procedure is performed in order to avoid any numerical disturbances at the ignition phase, rather than introducing a temperature or an energy field.

Flame radius extraction is performed based on the isocontour corresponding to progress variable = 0.75. Progress variable represents the degree of completion of the global combustion reactions [77], and is calculated based on the temperature as:

$$Progress\ Variable = \frac{T_{final} - T_{initial}}{T_{maximum} - T_{initial}}$$

Bradley et al. [78] stated that flame radius differentiation used for stretched burning velocity is nearly independent from the chosen isotherm or progress variable. To do that, each point on the selected isocontour is extracted and the distance to the origin is found. These points are averaged for each time step to obtain the average flame radius. Fig 4.2. illustrates a close-up view of the spherical flame propagation. Fig. 4.2a. is labelled as t=0 to indicate that it is the initial condition which corresponds to r=3.5mm and Fig 4.2b. is the flame front after 3ms. The isocontour corresponding to T=1750K for Φ=1 is illustrated as a black solid line on the figures.

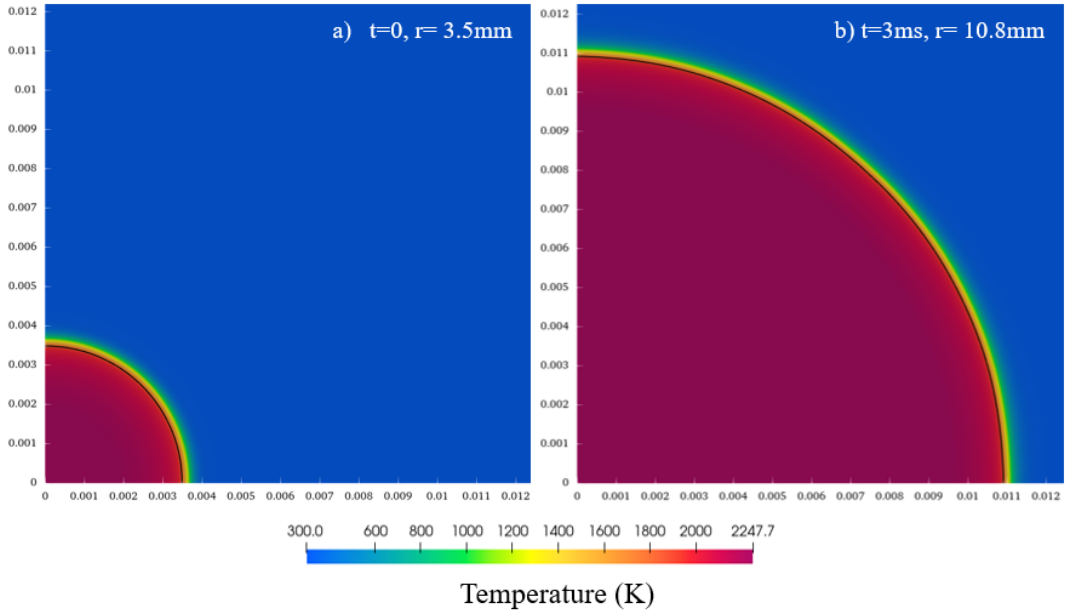

Figure 4.2. Spherical flame propagation and 1750K isocontour representations a) t=0 b) t=3ms

The mesh size is selected after a mesh independence study performed for the case with the smallest laminar flame thickness for the considered mixtures in this study (Φ=1 with %20 H_2 addition rate). It is reported in the literature that, for methane-air mixtures, the flame thickness is minimum around Φ=1[7,9,79] and decreases with hydrogen addition [7]. Computations are performed for 0.2mm, 0.1mm, 0.075mm, 0.05mm and 0.025 mm mesh sizes for freely propagating flame configuration. Fig. 4.3. shows the flame radius versus time evolution of a spherically expanding flame for different mesh sizes. It is found that, a further reduction after 0.05mm does not have an effect on the flame radius evolution with respect to time. Thus, 0.05mm grid size is selected, which corresponds to 1400 cells in each direction, and to a total of 1.96 million cells. A sample view of uniform mesh is illustrated in Fig 4.1.

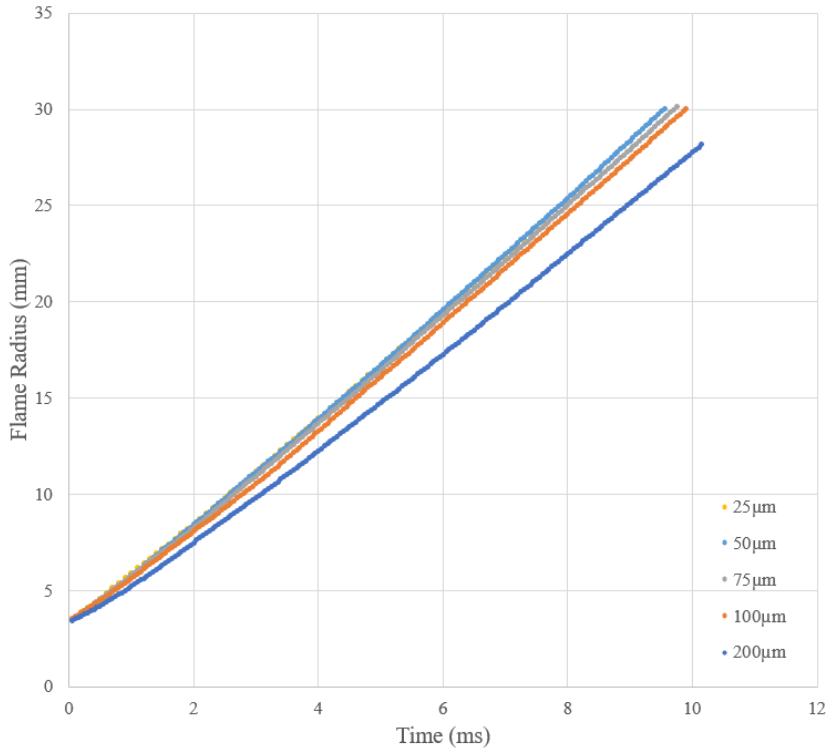

Figure 4.3. Results of mesh independence study performed for Φ= 1, flame radius (mm) evolution with respect to time.

CHAPTER 5

SPHERICALLY EXPANDING FLAMES; RESULTS AND DISCUSSION

5.1 Experimental Results

In this section, experimental results on the propagation of spherically expanding laminar premixed flames are presented. Experiments are performed for NG+air and NG+H_2+air mixtures, up to 20% H_2 addition (molar fraction in the fuel). Details of the partial pressure values in the mixture can be found in Table 3.1.

After the mixture is prepared, ignition is triggered, and the flame propagation evolution is recorded using the high-speed camera via the Schlieren imaging technique. Sample sequences of the obtained spherical flame propagation images for NG+air mixture at Φ= 0.8 for 1 bar pressure are shown in Fig.5.1. Experiments are performed at 288 ± 2K. In the first figure of the sequence, spherical flame generation due to electrode ignition is seen at the centre of the combustion chamber; this instance is labelled t=0. After ignition, the flame front starts to expand outwardly with a shape very close to spherical. Traces of the ignitors are seen in the figures, which should not be confused with cellular instabilities that we did not observe.

Flame radius data between r = 10mm and 25mm are considered for each experimental condition while calculating the laminar flame speed. Flame radius data below r = 10mm are not considered because of the ignition source perturbating effects. This value is taken between 5 to 10mm in the literature, depending on the experimental setup [7, 48, 66-69] Flame radius values above r = 25mm are not considered neither to avoid chamber wall effects. 25mm is selected based on our numerical simulations, where the wall effect on flame radius evolution is investigated in Chapter 5.2.1. For each experimental condition, the results are averaged for three successive experiments.

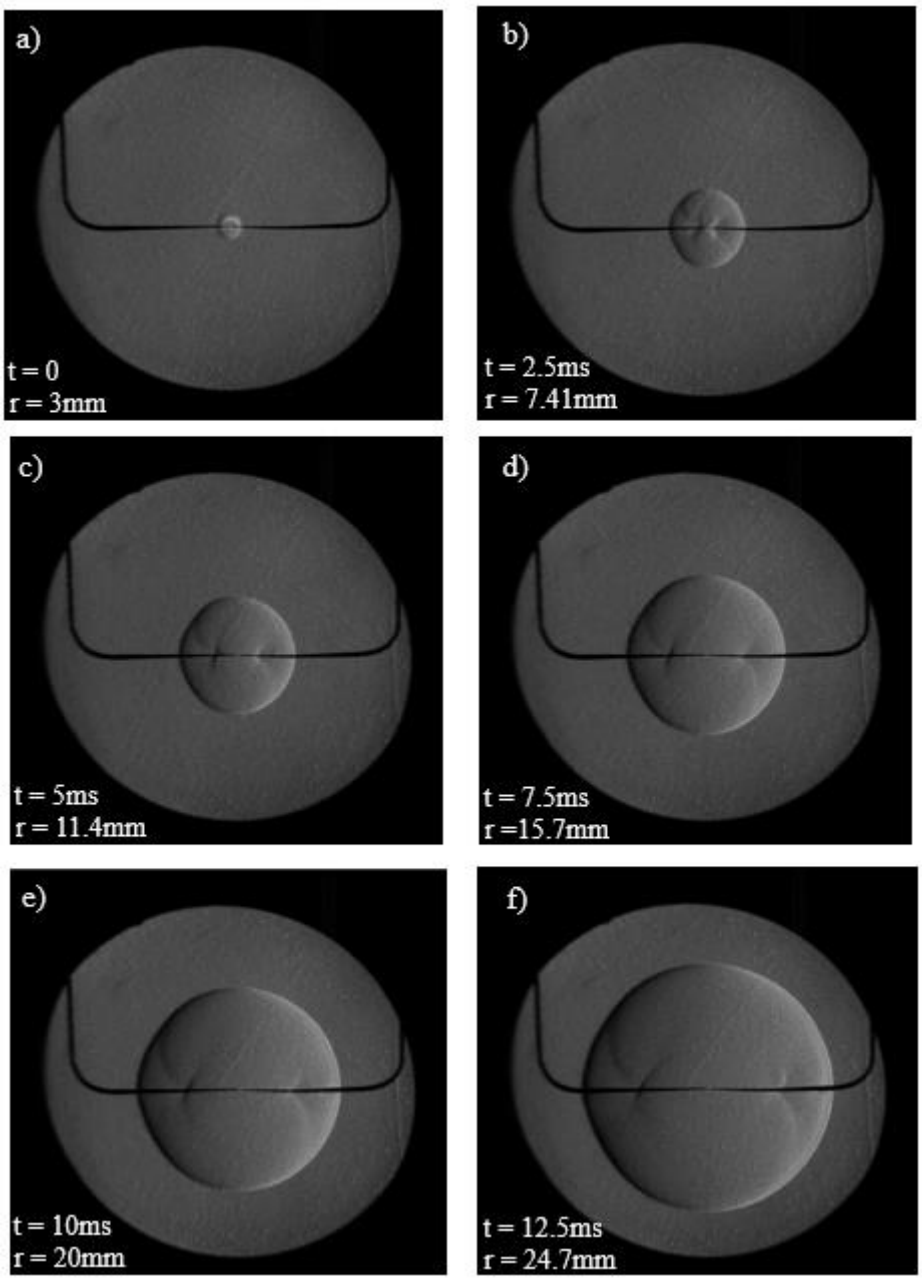

Figure 5.1. Spherical flame propagation for NG+air mixture at Φ=0.8

Fig. 5.2 shows the flame radius evolution with respect to time for various equivalence ratios (0.6-0.8-1) and hydrogen addition rates in molar fraction (0-20%). For all cases, flame radius evolutions show trends close to linear. The slope of the R(t) curves becomes higher with increasing equivalence ratio, which leads to higher stretched burning velocities. With hydrogen addition, R(t) curves shift towards the

left side and slight increases in slopes can be observed. Shifting towards left means faster stretched burning velocity. These curves are fitted with the exact solution of the linear model [66], which is explained in detail in section 3.2.3.2.

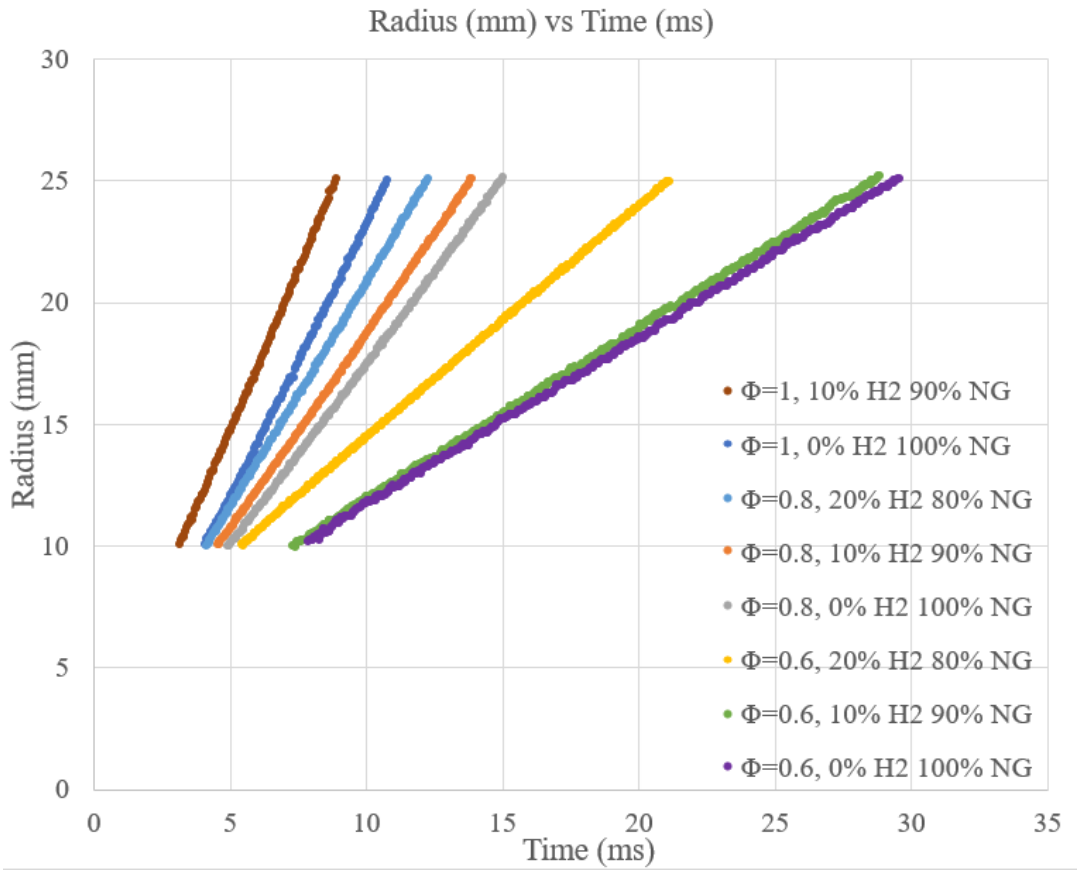

Figure 5.2. Flame radius evolution with respect to time for various equivalence ratios and hydrogen addition rates

An example of the stretched laminar burning velocity (V_S) with respect to time is given in Fig. 5.3. for Φ=0.8 NG+air mixture after the fitting is performed. It is clearly seen that, even though a global quasi-linear trend is observed from Fig 5.2, V_S shows an increasing trend, as also observed in [7, 66, 68]. As the flame radius increases, V_S increases gradually due to the decrease in the flame stretch as shown in Fig. 5.4. This phenomenon is valid for mixtures with positive Markstein length, based on Eq. 3.7. Also, this behaviour concerns mixtures where the Lewis number is above the critical value (around unity) [66].

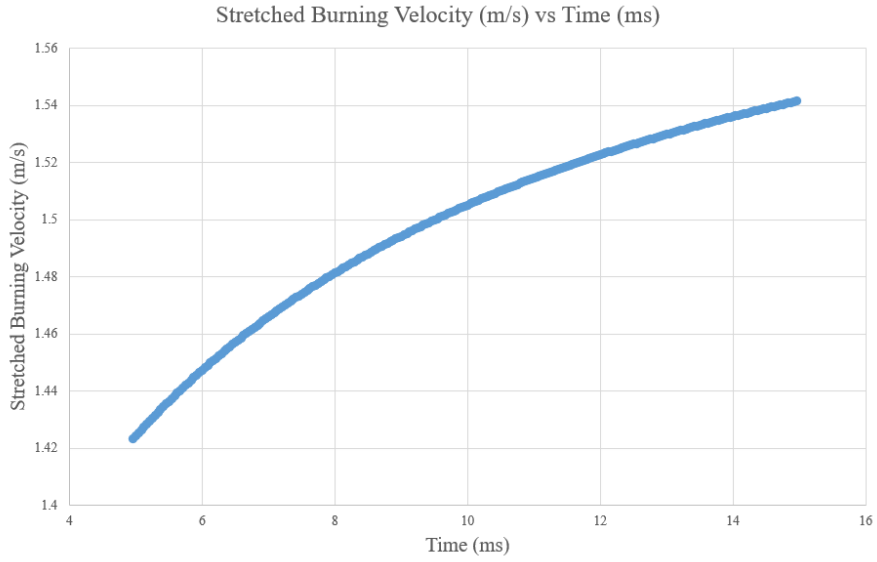

Figure 5.3. Stretched Burning Velocity (m/s) vs Time (ms) at Φ=0.8 for NG+air Mixture

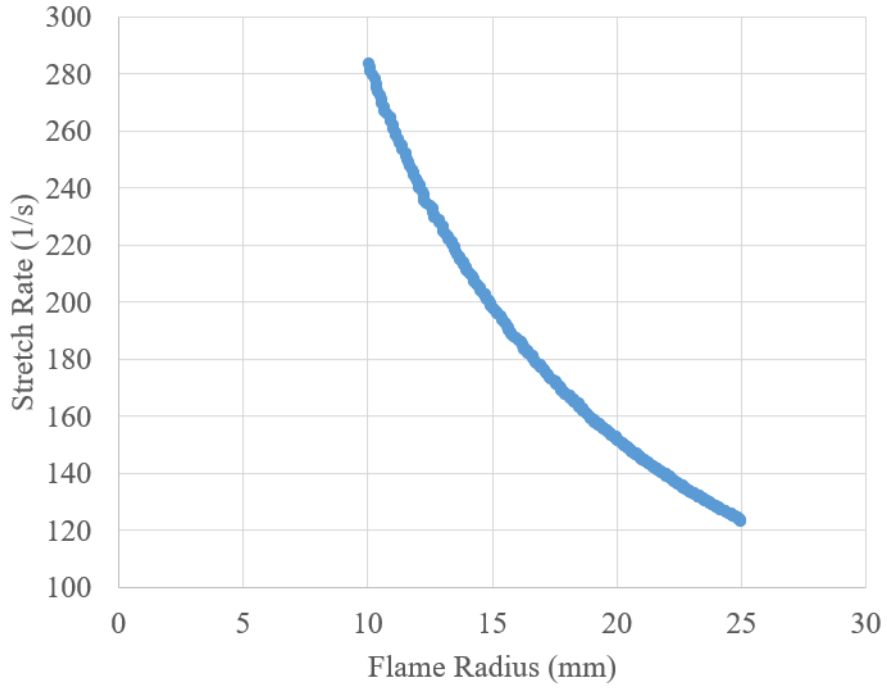

Figure 5.4. Stretch Rate (1/s) vs Flame Radius (mm) at Φ=0.8 for NG+air Mixture

Fig. 5.5. presents the variations of the stretched burning velocity (V_S) with respect the stretch rate (K) for various equivalence ratios and hydrogen addition rates. As the flame expands, V_S increases while the stretch rate decreases. The linear fits are represented for all mixtures and their extrapolation to zero stretch rate gives the unstretched burning velocity (V_{S0}). For the calculation of K, raw radius data is used, and all fits gave R^2 value of 1. All data between r=10mm and r=25mm is used. With the increase of both the equivalence ratio and the H_2 addition rate, V_{S0} is found to increase.

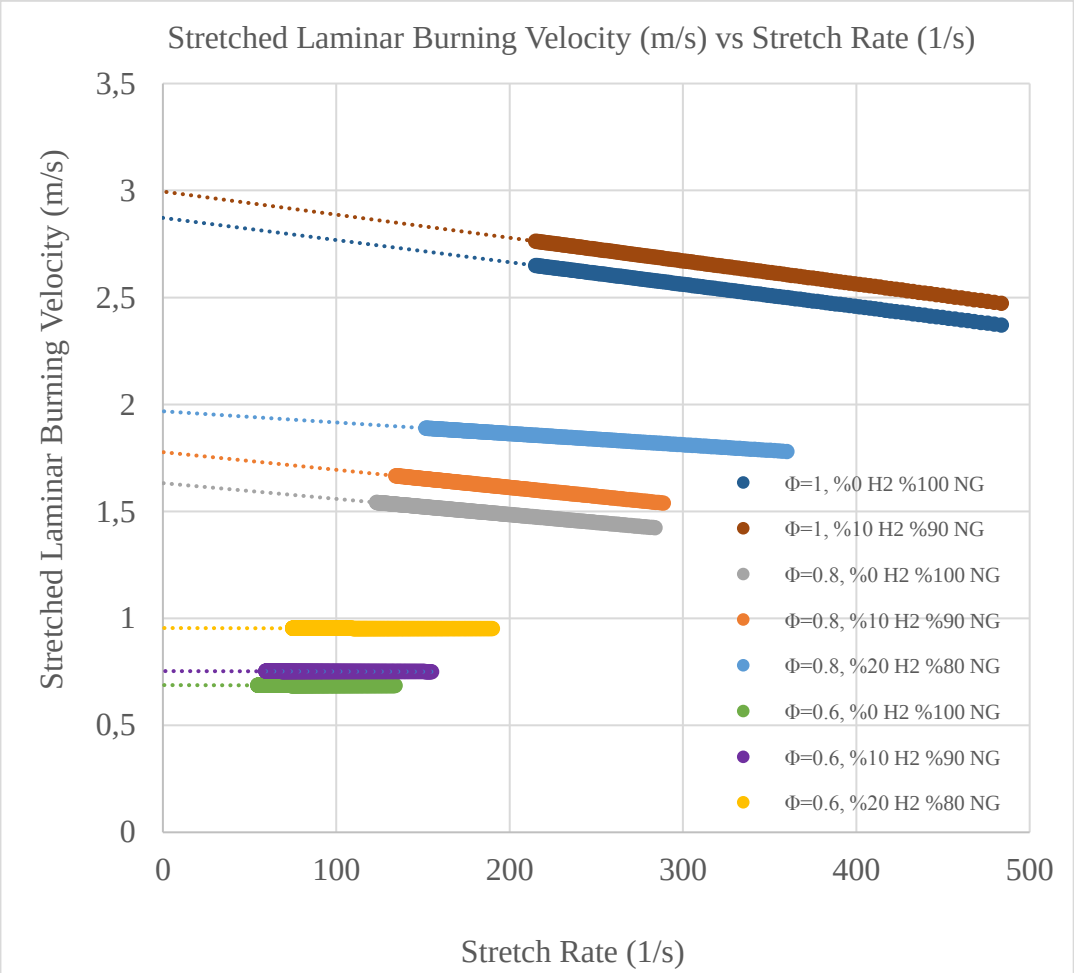

Figure.5.5 Stretched Burning Velocity (m/s) vs the Stretch Rate (1/s) for various equivalence ratios and hydrogen addition rates

The slope of the curves corresponds to the Markstein length L_b, which is positive for all the mixtures considered in this study. This also shows that even in leanest condition (at Φ=0.6), hydrogen addition up to 20% in volume does not change the sign of L_b, which is a critical flame characteristic of NG/CH4+air premixtures.

5.2 Laminar Flame Speed Results Compared to 1D Numerical Computations

1D flame computations are performed using open-source CANTERA code. Adiabatic, freely propagating laminar premixed flames are modelled with GRI-MECH 3.0 chemical kinetic mechanism. Flames in the equivalence ratio interval between Φ=0.6 and Φ=1.3 are computed. Multi-component transport is considered in the computations. After unstretched laminar burning velocity (V_{S0}) is obtained by performing the linear extrapolation operation, S_L^0 is calculated by dividing V_{S0} by the expansion rate (σ) as shown in Eq. 3.8. The expansion rate (defined as the ratio of unburned to burned density) is also calculated using the 1D computations software package. Calculated expansion rates are provided in Appendix C.

Fig 5.6 presents the overall experimental results for unstretched laminar flame propagation speeds and 1D computations for comparison. This figure illustrates the changes in the laminar flame speed for both equivalence ratio variations and the H_2 addition rates to NG-air (or to CH_4-air) mixtures. Lines represent 1D computations and experimental results are shown with symbols. Solid lines represent 1D computations for NG – air flames at 288K initial temperature; dotted lines are used for NG – air flames computations at 300k initial temperature and dashed lines are used for CH_4 – air flame computations at 300K initial mixture temperature. Colour coding is used for the H_2 addition rates. Blue represents no H_2 addition to the NG-air mixture, red and green corresponds to 10% and 20% H_2 addition rates respectively.

1D simulations and experiments both show that laminar flame speed increases with increasing the equivalence ratio (for considered mixtures in this work). 1D simulations also show that the laminar flame speed reaches its peak around Φ=1.05 and starts decreasing as the mixture becomes richer. This trend is also found in many experimental and numerical studies in the literature [7, 39, 47-48, 53-55]. Hydrogen addition also increases the laminar flame speed for each equivalence ratio; higher the hydrogen addition rate, higher is the laminar flame speed.

Differences between the experimental values of the laminar flame speed and those from 1D flame computations exist but they are within the limits of the literature values and are also within our experimental error margins. In addition, 1D computations assume freely propagating adiabatic flame assumptions which are not fully valid in the experiments. The effect of the confinement will be discussed below in section 5.3 with 2D computations. Fig. 5.6 also presents that; computations are affected by the reactive mixture temperature change from 288 K to 300 K. Computational results are also shown for CH4-air mixtures and for the actual NG compositions.

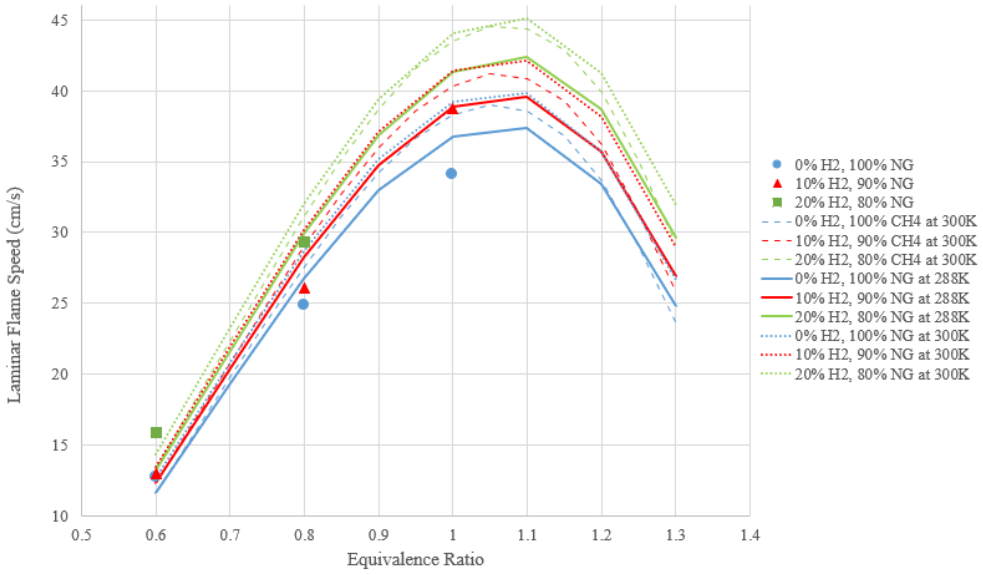

Figure 5.6. Comparison of Laminar Flame Speed (cm/s) vs Equivalence Ratio, experimental values and 1D Cantera code computation results

Experimental results found in the present study are compared with some literature results in Figs.5.7-5.9. Authors, years, experimental conditions, and laminar flame speed calculation methods of the reference studies are given in Table 5.1. It should be noted that reference experiments are performed for CH4-air mixtures with H_2 addition, compared to the NG-air mixtures used in this work. Error bars for the present experiments indicate the standard deviation between 3 different experiments for each conditions set used for averaging.

Table 5.1 Laminar flame speed studies in the literature for methane-hydrogen-air mixtures used for comparison with our results

Author	Year	Conditions	Experimental Methods	H_2 addition rate (%)
Dirrenberger et al. [54]	2011	298K, 1atm	Heat Flux	0-67
Hu et al. [48]	2009	303K, 1atm	Constant Volume	0-100
Hermanns et al. [39]	2007	298K, 1atm	Heat Flux	0-40
Halter et al. [7]	2005	298K, 1atm	Constant Volume	0-20

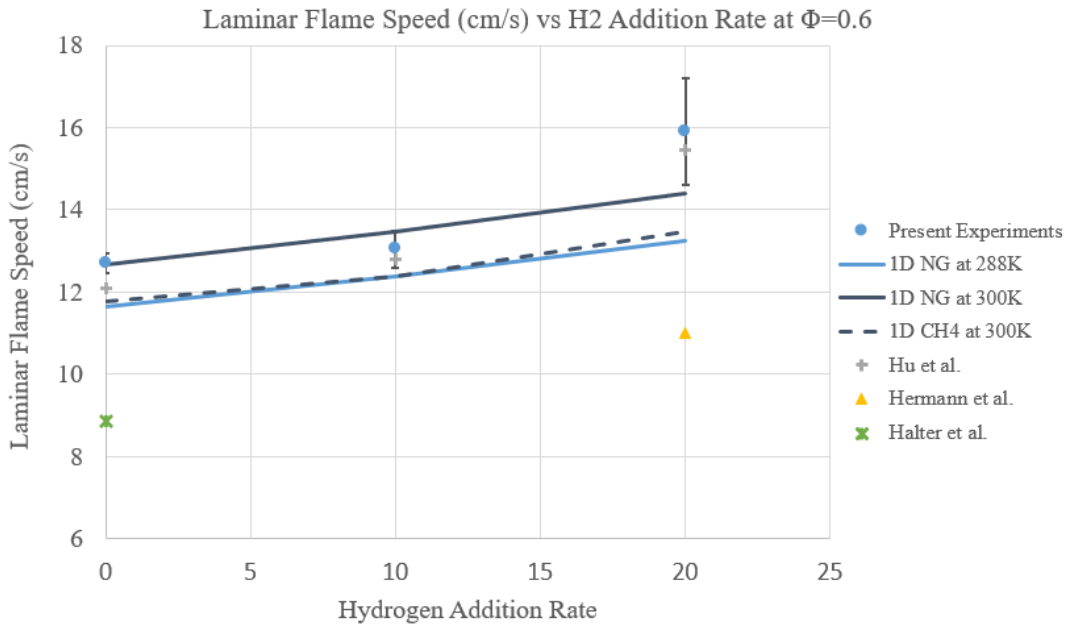

Figure 5.7. Laminar Flame Speed (cm/s) change with Hydrogen Addition Rate (%) at Φ= 0.6

Fig. 5.7 illustrates changes in S_L^0 with the hydrogen addition rate at Φ= 0.6 for the present experiments, reference results and 1D computations. In the literature only Hu et al. (2009) studied hydrogen addition at Φ= 0.6 for the considered hydrogen addition rates; Hermanns et al. (2007) studied 20-40%H_2 addition rates. Present results and the experimental results of Hu et al. (2009) are in good agreement with each other. There is a significant difference between Halter et al. (2005) and the present experiments at no H_2 addition rate. Hermanns et al. (2007) predicts much lower S_L^0 values than the present experiments for %20 H_2 addition rate. At Φ= 0.6, experimental values exceed 1D computations, which is not observed for Φ= 0.8 and Φ= 1. This trend may be attributed to the increase in the experimental equivalence ratio determination uncertainty when far away from stoichiometric conditions [80]. For the present experiments, %10 H_2 addition increases S_L^0 slightly (% 2.5), while 20% H_2 addition results in a significant increase (%22). Standard deviation between our experimental results increases with the hydrogen addition at Φ= 0.6 (minimum 0.24 cm/s, maximum 0.86 cm/s).

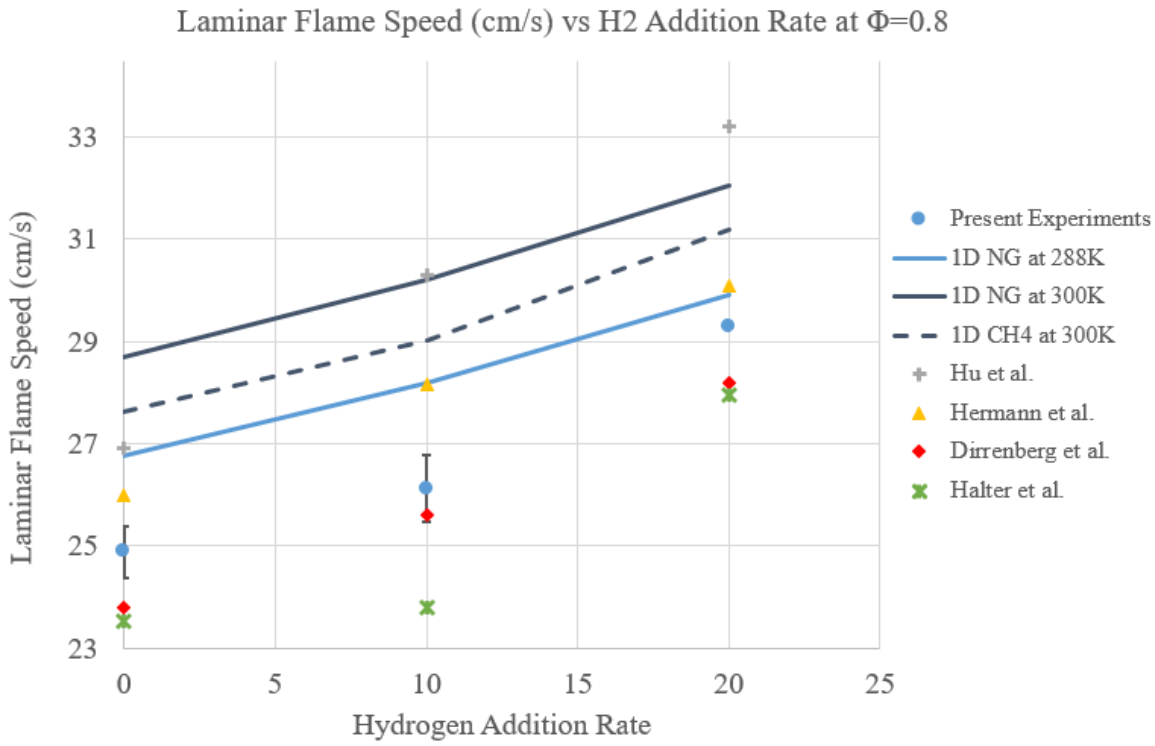

Figure 5.8. Laminar Flame Speed (cm/s) changes with the Hydrogen Addition Rate (%) at Φ= 0.8

Present experimental results for changes in S_L^0 with the H_2 addition, comparisons with 1D flame computations and the literature results at Φ= 0.8 are given in Fig. 5.8. Compared to Φ= 0.6, there are more reference data in the literature for Φ= 0.8. Present results agree well with the literature experimental results and fall in between the results of Hermanns et al. (2007) and Dirrenberger et a. (2011) (around 4% deviation). 10% H_2 addition results in 5% increase in S_L^0, while 20% H_2 addition increases S_L^0 by 18%. Hu et al. (2009) show the highest S_L^0 values while the experimental results of Halter et al. (2005) are the lowest. Only Hu et al. (2009) predict higher S_L^0 values than 1D computations for both 10% and 20% H_2 addition rates. Standard deviations of the averaged values in the present work are 0.5 cm/s and 0.66 cm/s for 0% and 10% H_2 addition respectively. For 20%, experimental results are almost the same.

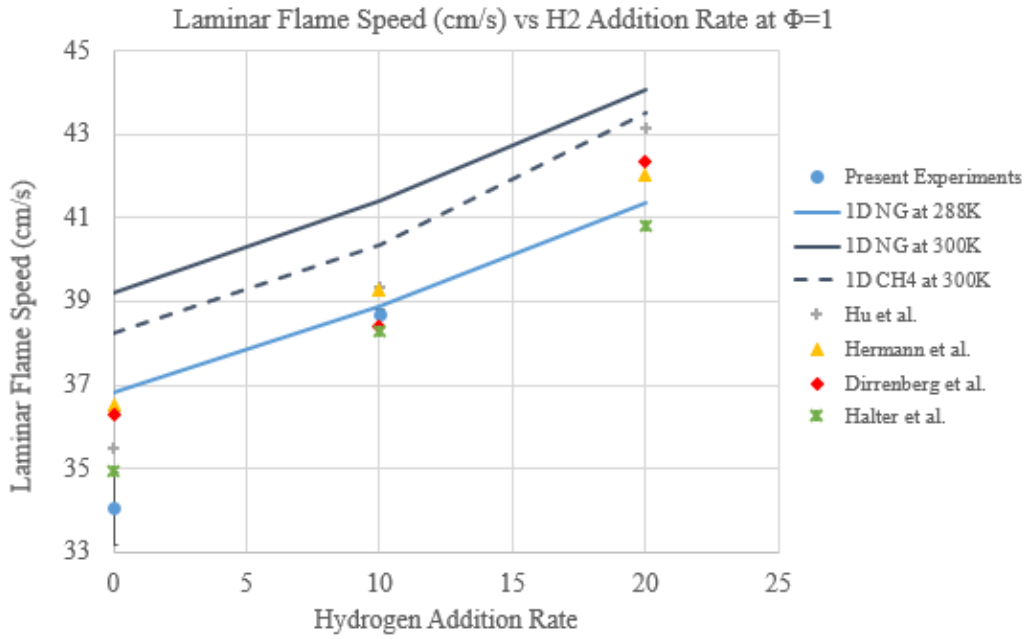

Figure 5.9. Laminar Flame Speed (cm/s) changes with the Hydrogen Addition Rate (%) at Φ= 1

Fig 5.9 illustrates the variations in S_L^0 with the hydrogen addition rate at Φ= 1 and compares with the literature results and 1D computations. Only 10% H_2 addition is considered for Φ= 1 in our work as we could not obtain an acceptable experimental result for the 20% case. For stoichiometric NG-air mixture, our laminar flame speed results are found to be smaller compared to the results in the literature: 5.5% smaller than Hermanns et al. (2007) and 2.5% smaller than Halter et al. (2005). 10% H_2 addition results in 13.7% increase in the laminar flame speed and agrees very well with the values found in the literature. 0.82 cm/s standard deviation is calculated for 0% H_2 addition rate and for 10% H_2 addition rate standard deviation is so small that error bars cannot be seen in the figure.

Calculated Markstein lengths (Lb) are illustrated in Fig. 5.10 and compared with the results from the literature. Lb is calculated from the slope of the variation in the stretched velocity versus the stretch rate (Eq. 3.7) and it represents the sensitivity to stretch for a flame of a given mixture.

Results for 0%, 10% and 20% H_2 addition rates are represented with blue, red and green colours respectively. Lb results found in this study is compared with Hu et al. (2009).(no data for %10 H_2 addition) and Halter et al. (2005) (no data for Φ= 0.6), which are both determined using the constant volume spherically expanding flame method. Due to the unstretched nature of the heat flux method, there is no Markstein length data presented in Hermanns et al. (2007) and Dirrenberger et al. (2011). From Fig. 5.10, it is observed that Lb increases with increasing equivalence ratio for both the present work and literature results. Also, it is shown that Lb decreases with H_2 addition rate in the present work, this indicates that with the addition of H_2 to the mixture, laminar flames tend to be less sensitive to stretch [48]. For Φ= 0.6, Lb values are on top of each other in the figure. Present experiments predict Lb values as 0.04, 0.02 and 0.016 respectively for 0%, 10% and 20% H_2 addition rate. This indicates that, there is almost no effect of stretch for Φ= 0.6. For Φ= 0.8 and Φ= 1, Lb estimates in the present work and Hu et al. (2009) are similar. Halter et al. (2005) predicts smaller Lb for each case, compared to the present work and Hu et al. (2009).

Deviation between Lb values in different experiments can be associated with the sensitivity of Lb determination to the selected data points. Even though the start and end points of the raw radius data did not affect laminar flame speed significantly, they have substantial effects on Lb calculations, especially when a polynomial is fitted to raw radius data to obtain the stretched burning velocity [66].

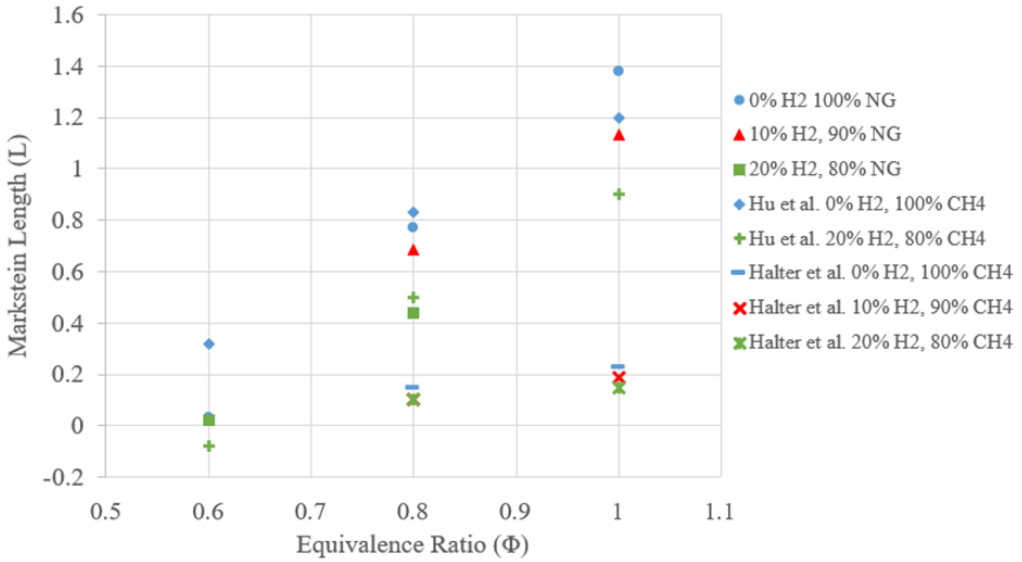

Figure 5.10. Markstein length values for varying equivalence ratio and hydrogen addition rates

During the calculation of laminar flame speed from spherically expanding flames, there are various factors influencing the accuracy of the calculation such as ignition, radiation, confinement, extrapolation to zero stretch and mixture preparation [80]. The uncertainty arising from the preparation of the mixture is highly dependent on the accuracy of the pressure transmitter used in the experiments to regulate the partial pressures in the mixture. Uncertainty calculation for the equivalence ratio is performed based on the detailed work of Chen [80] and formulated as follows for alkanes and air mixtures:

$$\Phi = \Phi_0 + \left(\frac{\Delta P_{Fuel}}{P} - \frac{\Phi_0}{1.5n + 0.5}\frac{\Delta P_{O2}}{P}\right)[\Phi_0 + (1.5n + 0.5)(1 + r)] \tag{5.1}$$

where Φ_0 is the target equivalence ratio, n is the carbon number, ΔP_{Fuel} and ΔP_{O2} are uncertainities in partial pressures of fuel and oxygen respectively and r is the molar ratio of N2/O2 (0.79/0.21 for air). For the present experiments, pressure uncertainity is equal to ±0.4% (see section 3.1.4). Table 5.2 presents the uncertainties calculated for Φ and their corresponding effect on S_L^0 for the present experimental conditions. For the detailed information on the transition from the equivalence ratio

uncertainty to S_L^0 uncertainty, reference [80] should be consulted. Only CH4-air mixtures are considered in this calculation, and it is assumed that these uncertainties will not change much with the addition of H_2 to the mixture.

Table 5.2 Uncertainty in Φ (%) and S_L^0 (%) for different Φ

Φ	Uncertainty in Φ (%)	Uncertainty in S_L^0 (%)
0.6	9.22	48.12
0.8	7.21	18.08
1	6.22	6.842

This table shows that the Φ uncertainty effects the S_L^0 uncertainty strongly for mixtures far stoichiometric condition. This can be understood from Fig. 5.6 showing the variation of S_L^0 vs Φ. In the future work section (Chapter 7.2) the importance of the measurement accuracy of partial pressures is highlighted.

5.3 Numerical Results

5.3.1 2D Spherical Flame Propagation Results

2D spherical flame modelling and computations are performed for Φ=0.6, 0.8 and 1, both for 100% CH4-air premixture and with 20% H_2 addition rate. Each condition is simulated under freely propagating and confined conditions, which correspond to a total of 12 runs. Mass fractions for the unburned mixture are given in Table 5.3.

Table 5.3 Mixture mass fractions of the unburned mixture, with Φ and H_2%

Φ	H_2%	Mass Fractions			
		CH_4	H_2	$O2$	N_2
0.6	0	0.034	0	0.225	0.741
	20	0.032	0.001	0.225	0.741
0.8	0	0.047	0	0.223	0.73
	20	0.042	0.0013	0.223	0.734
1	0	0.055	0	0.22	0.725
	20	0.052	0.0016	0.22	0.726

Spherical flame propagation 2D computations are illustrated in Fig. 5.11. for %100 CH4-air mixture at Φ=1, with contours of a) temperature, b) normalized heat reaction rate, c) CH4 mass fraction and d) CO2 mass fraction. 3 consecutive snapshots are shown at instances at t=0, 7.5ms and 15ms, respectively. Only 40x40 mm section of the domain is considered to identify better the contours. As the flame propagates, the area of burned gases with high temperature increases. Normalized heat reaction rate represents the reaction term $\dot{R}_h$ (from Eq. 4.4), which depicts the reaction zone. It can be associated with the flame front and one can observe the increasing radius with time. As the flame propagates through unburned gases, CH4 is consumed and CO2 is produced as a product of the reaction, which can be seen in Figs. 5.11c. and 5.11d respectively.

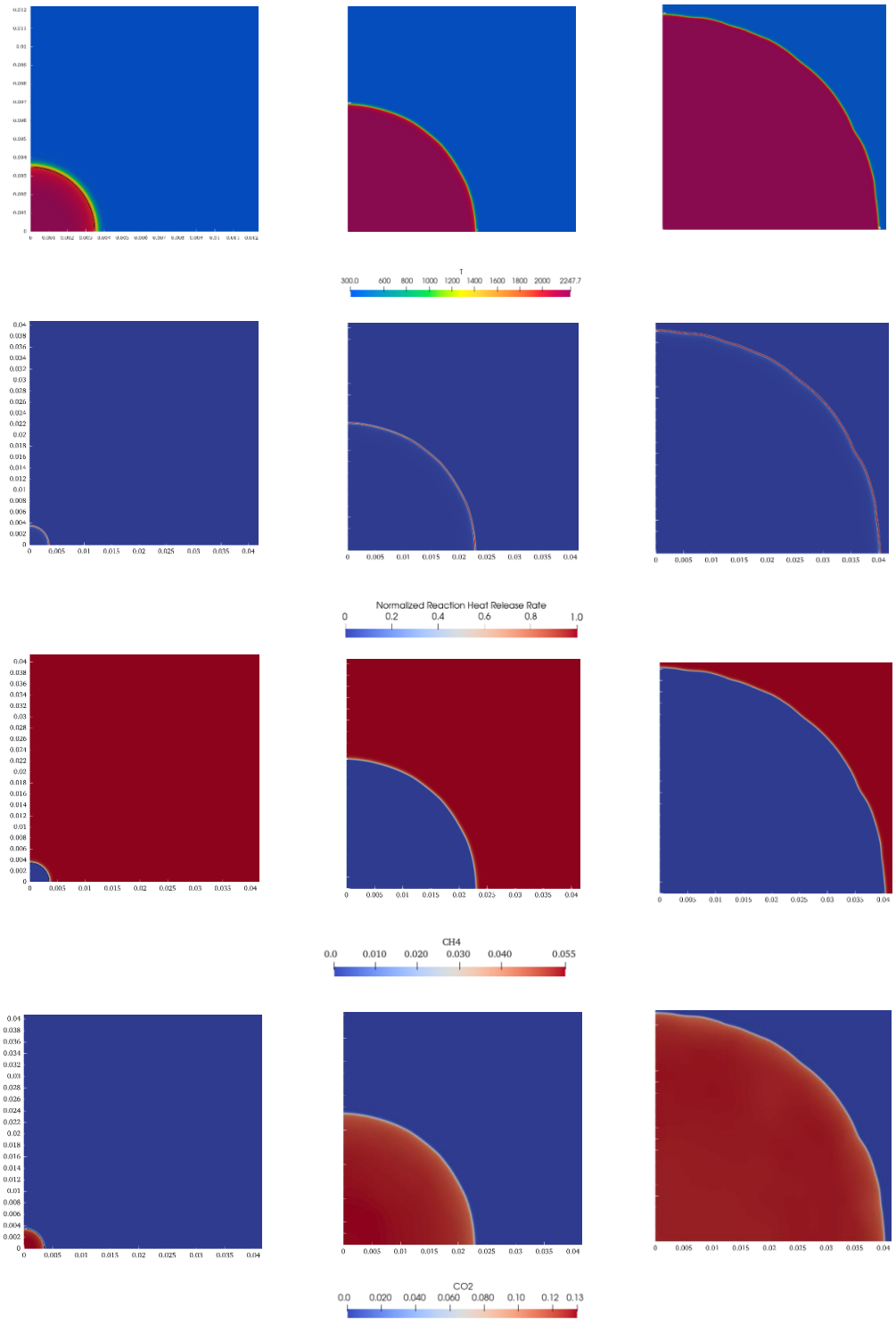

Figure 5.11. a) Temperature b) Normalized Heat Release Rate c) CH4 d) CO2 contours for Φ=1 at t=0, 7.5ms and 15ms

Figs. 5.12 to 5.14 present and compare 2D spherical flame computations for freely propagating and confined cases. The reduction of the propagation velocity under the confined cases is apparent from Figs. 5.12 and 5.13. both for CH4-air flames and those with hydrogen addition. It is however obvious from Fig.5.12 that the confinement effect is less important for the hydrogenated mixture. The relative differences between flame radius evolutions under freely propagating and confined cases are depicted in Fig. 5.13 showing that differences strongly increase when the chamber walls are approached. Finally, Fig. 5.14 compares the laminar flame speeds from 1D and freely propagating and confined 2D computations with our experimental data for varying equivalence ratios. Again, the effect of confinement is apparent for the flame propagation speeds, albeit not larger than 10%. The experimental values are lower than the computed ones because of the effects of heat loss (non-adiabaticity) and the confinement effects. But in general, they show that the experimental facility and the experimental procedure that we developed in this thesis are able to reproduce both phenomenologically expected laminar flame propagation results and the literature results.

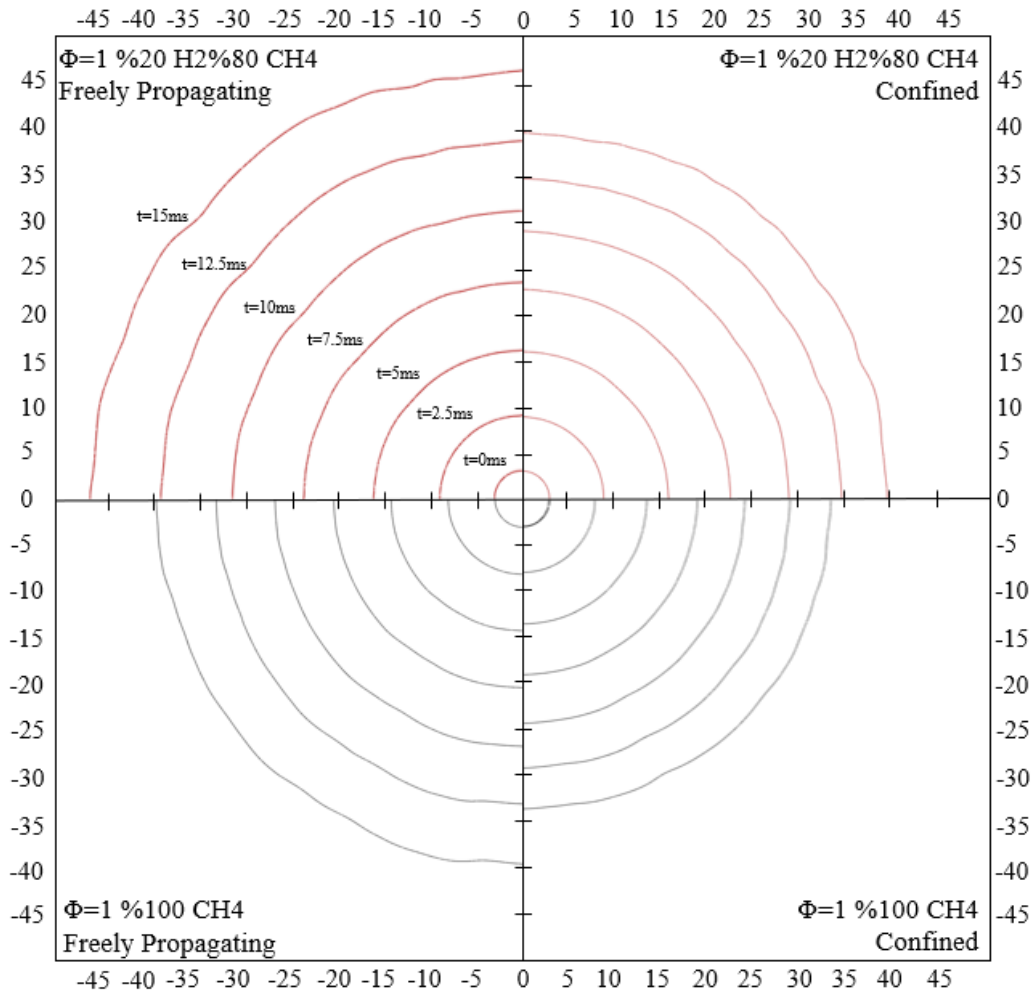

Figure 5.12. Representations of 2D spherical flame propagation computations vs time, visualized using T=1750K isocontours for Φ=1 both with CH_4/air and with CH4/air 20%H_2 addition rate. Comparison of the confinement and H_2 addition effects

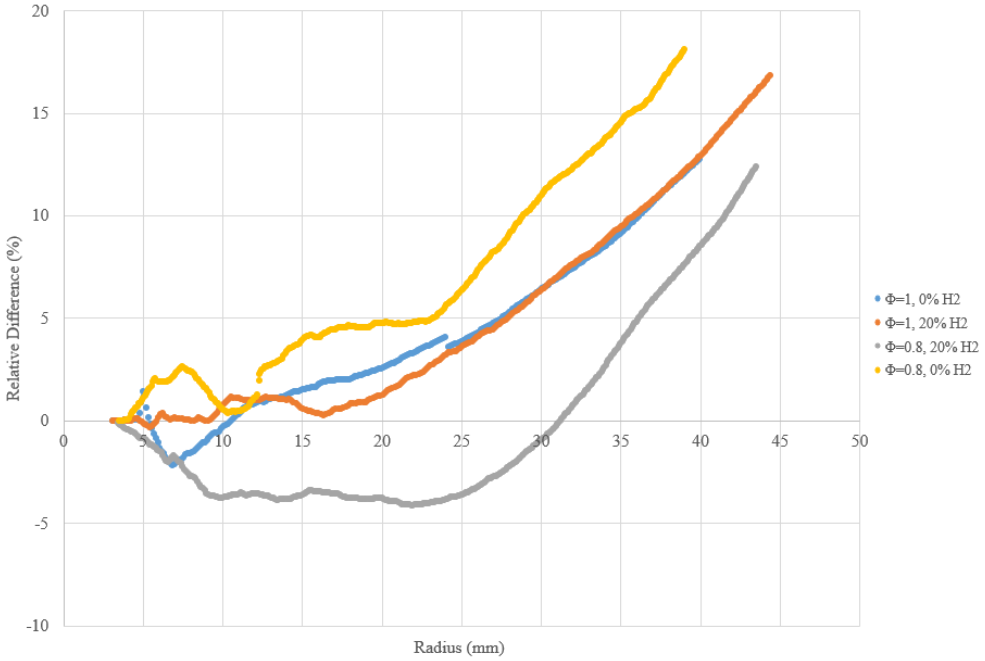

Figure 5.13. Relative differences (%) between confined and freely propagating flame radius development based on confined flame radius values for Φ=0.8 and 1. For CH4+air mixture and CH4+air with 20% H_2 addition

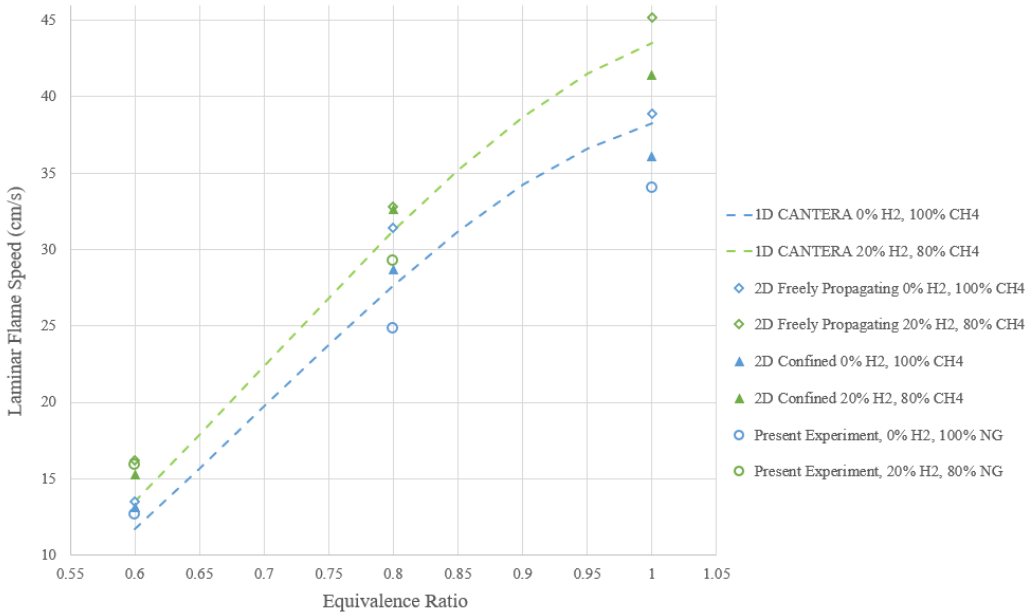

Figure 5.14. Laminar Flame Speed comparisons between 2D Numerical Results, 1D CANTERA computations and present experiments

CHAPTER 6

NUMERICAL BOUNDARY LAYER FLASHBACK STUDIES

6.1 Methodology

Flashback dynamics for CH4-air and CH4+H2-air laminar premixed flames explored numerically, based on primarily experimental research conducted in the past. For a particular combination of fuel mixture and bulk input velocity, a numerical framework is selected to determine whether or not flashback occurs. 10% and 20% volumetric hydrogen was introduced to methane for each of the tested wall temperature conditions (300K and 600K). In addition, an adiabatic wall case with a 20% hydrogen addition rate is examined. In this part, instead of full GRIMECH 3.0 mechanism, a reduced version is used where NOx reactions are not included. Reduced version includes 36 species and 218 reaction. This way, a noticeable acceleration in run time is achieved. Seven different cases are presented in this work totally. The computed flashback limits are compared with the experiments of de Vries et al. [81], the experimental correlations proposed by Lewis and von Elbe [31], Putnam et al. [32] and the theoretical correlations of Hoferichter [33].

6.1.1.1 Computational Domain and Boundary Conditions

The experimental setup of deVries et al. [81], a quartz tube burner with 10 mm inner diameter and 1 m length, is chosen as the basis geometry for the computational domain. A two-dimensional modeling approach is used for the burner and the surrounding ambient air. Even though this assumption does not strictly represent the axisymmetric geometry of the experimental case, it is chosen to capture asymmetrical instabilities that result in boundary layer flashback. The computed inlet tube length is set to be 30 mm from the numerical domain inlet to the burner exit

(see Fig. 6.1) to observe flashback dynamics inside the tube. A total number of 102,050 fully structured cartesian cells make up the mesh system which is uniformly confined at the vicinity of the flame front. Since resolving the boundary layer with enough detail is critical in computing flame flashback, the cell size in the radial direction is set to 0.066 mm, giving y^+=0.33 for the highest bulk inlet velocity case. This cell size also order of the flame thickness for the investigated mixtures. The mesh resolution is further validated by 1D laminar flame speed calculations with the same resolution as the two-dimensional mesh used in OpenFOAM computations.

Figure 6.1 illustrates the computational domain with its boundary conditions. The cold premixture enters the domain inlet with a fully developed Hagen-Poiseuille flow velocity profile, as demonstrated in the experimental study under consideration [58]. It is assumed that the initial temperature and pressure are 300 K and 100 kPa, respectively. Adiabatic temperature boundary conditions are assumed for outlet. At the outlet boundary, a wave transmissive pressure outlet boundary condition is applied to prevent any instability caused by incoming waves. The outlet's reference pressure is set to atmospheric pressure (100 kPa), and the velocity boundary condition at the outlet prohibits any backflow. Both adiabatic and two constant wall temperature conditions were implemented. There are no experimental burner wall temperature measurements given in de Vries et al.'s study [81]. Therefore, we performed the computations for an isothermal wall at 300K and 600K. The two wall temperature values were selected to guarantee that the experimental flashback limits fall within the estimations derived from these two sets of calculations. Kurdyumov et al. [82] examine the effect of burner temperature; they predict that the experimental circumstances will be between adiabatic and cold isothermal wall conditions. Our calculations indicate that, under adiabatic wall circumstances, the flame attaches to the wall because there is no heat loss to the burner walls. This is a non-realistic phenomenon modelled for demonstration purposes; hence, only results for constant wall temperature are described in detail below.

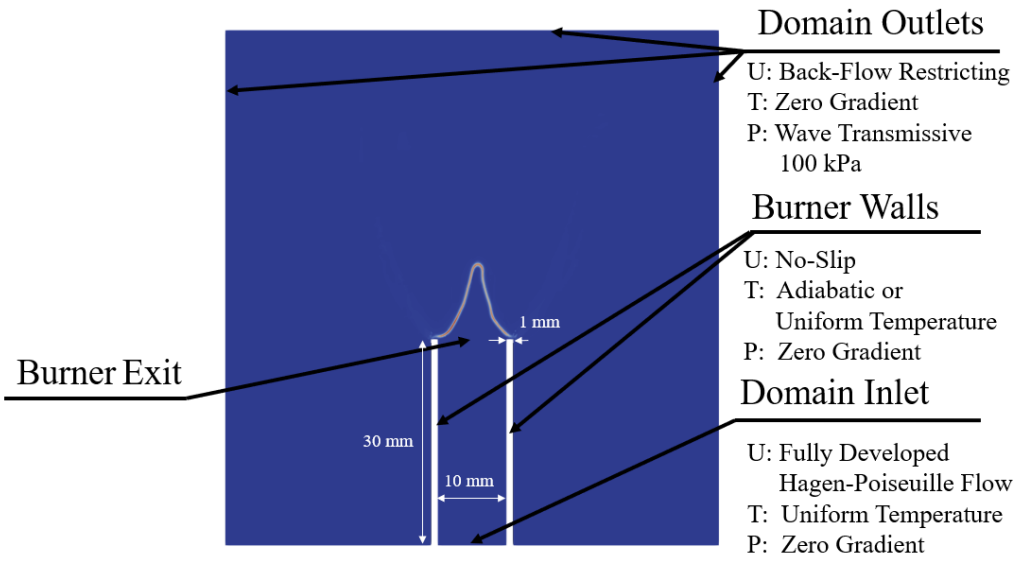

Figure 6.1. Problem domain and boundary conditions for the flashback study

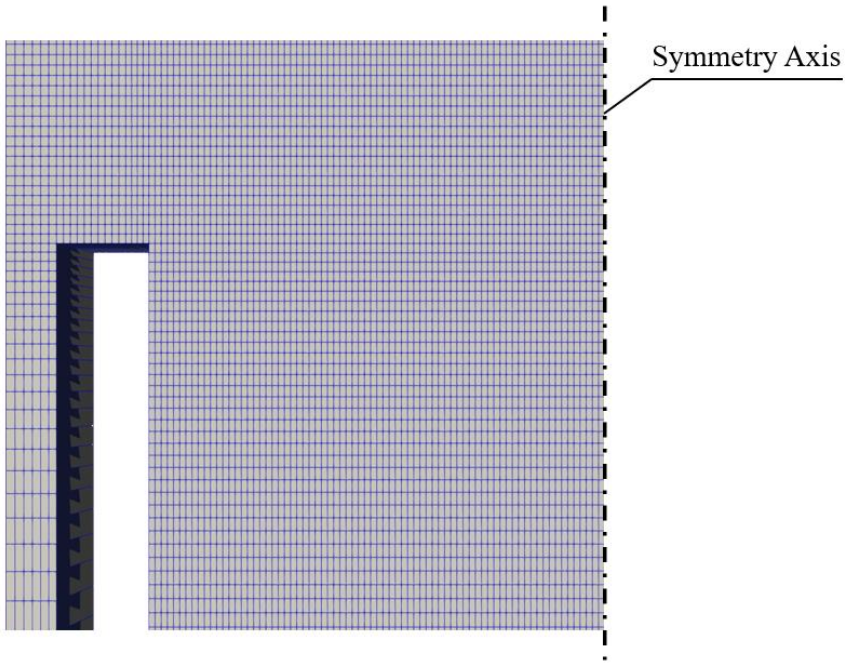

Figure 6.2. Structured mesh of the problem domain, close up view to the burner exit

6.1.1.2 Equivalence Ratio Shift and Species Concentrations

In the experimental work of de Vries et al. [81], the premixture equivalence ratio changes with hydrogen addition due to their experimental procedure. To compare the numerical results with the experiments, the changes in the equivalence ratio are calculated accordingly, as shown in Table 6.1. The mass fractions are subsequently calculated to adjust the reactive mixture composition to the experiments.

Table 6.1 Equivalence ratio shift and species mass fraction with the addition of hydrogen

H_2% [mol]	Φ	Y_{H_2}	Y_{CH_4}	Y_{O_2}	Y_{N_2}
0	1.3	0	0.071	0.216	0.713
10	1.258	0.00093	0.067	0.217	0.715
20	1.216	0.0019	0.063	0.217	0.716

6.2 Results and Discussion

6.2.1 Temperature and Velocity Profiles of Stationary Flame

Combustion is initiated by imposing a homogeneous temperature field set at 2000K at the burner exit. For a stable CH_4 -air flame with no H_2 addition and a bulk inlet velocity of 0.40 m/s, Figs. 6.3 show the flow streamlines colored by the temperature (Fig. 6.3a) and by the velocity magnitude (Fig. 6.3b). When the cold flow reaches the flame front, the streamlines turn in the flame's local normal direction, and the velocity jump is well observed.

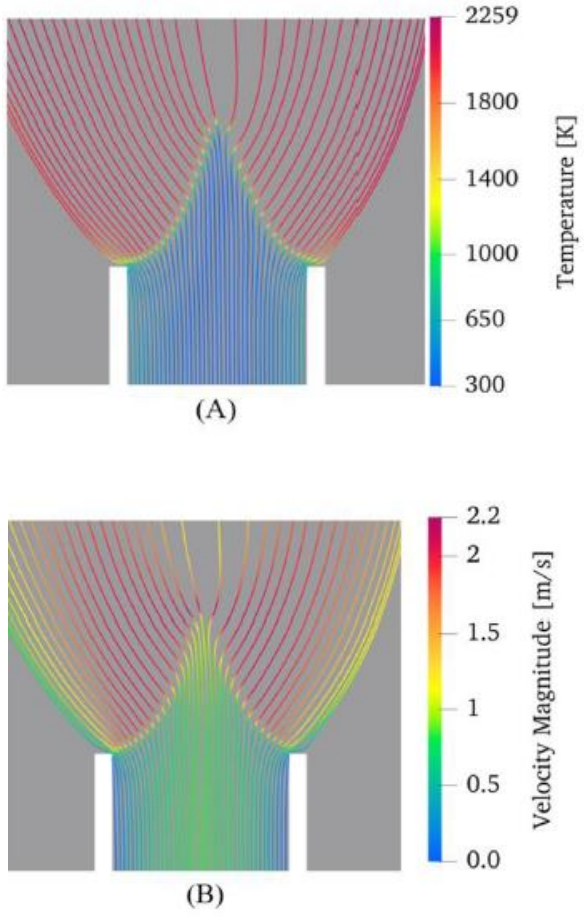

Figure 6.3. Streamlines colored by (a) temperature [K] (b) velocity magnitude [m/s].

6.2.2 Flashback Dynamics

The computations began with a stationary flame far from flashback conditions; the inlet velocity was then gradually decreased until flashback occurred. When the flame front begins to enter the burner tube and propagates upstream, it is considered to be flashback. For all cases, the flashback dynamics analysis begins with a stable flame equivalent to the lowest bulk inlet velocity that does not result in flashback under the conditions in consideration. To explore the flashback dynamics, the bulk entrance velocity of the laminar flame is decreased (at the time marked t = 0) by a percentage of the laminar flame speed.

For a CH4-Air mixture at Φ =1.3 and a wall temperature condition of 600K, an example of the method employed for the computational analysis of flame flashback dynamics is described below (Fig. 6.4). In the subsequent flashback sequences, the flame front is depicted using the normalized heat release rate, which is the ratio of the calculated heat release rate to its maximum value. At the start of the computations, a stable laminar flame is simulated with a bulk inlet velocity of 0.48 m/s, which is double the computed S_L (0.24 m/s). The bulk inlet velocity is then gradually decreased until the formation of a leading edge is observed. The step values for velocity reduction correspond to 5% of the laminar flame speed. This is the ratio between the bulk inflow velocity reduction step (0.012 m/s) and the estimated laminar flame speed (0.24 m/s) in this example. In this instance, the decrease in bulk inlet velocity from 0.38 m/s to 0.368 m/s causes flashback. Once flashback is initiated, the bulk velocity is kept constant while the temporal flame dynamics are computed.

Figure 6.4a depicts a flame moving at 0.38 m/s, which is evident that the flame front is not linked to the burner rim. Time is set to t=0 at the instant when the bulk inlet velocity is reduced from 0.38 m/s to 0.368 m/s. 0.195 seconds after the bulk inflow velocity decreases to 0.368 m/s, flame symmetry is lost (Fig. 6.4b) and the flame front on the left side of the burner rim becomes parallel to the rim. Figure 6.4c depicts the formation of a leading flame edge and the propagation of the flame front in the

upstream direction. The quenching distance is visible at the left wall, where the rate of heat release diminishes (Fig. 6.4c and d). In these figures, the emergence of the penetration distance is also evident. The front tip of the flame is pushed to the right, and the flame becomes tilted (Fig. 6.4c and 6.4d). The tilted flame form, also observed in experiments [31,81,83-84] and a numerical study by Vance et al. [85], is generated by a negative pressure gradient upstream of the leading edge and the subsequent deflection of streamlines in the opposite direction of the flame [86]. Figure 6.4d depicts the initiation of the flame front's upstream propagation.

In this example, flashback occurs at a bulk velocity of 0.368 m/s, which is 53% faster than the speed of laminar flame propagation (0.24 m/s). A 0.195-second flashback initiation latency is noted (Fig. 6.4b). Formation of the leading edge is noticed at 0.27s (Fig. 6.4c), and upstream flame propagation is observed at 0.292 s. (Fig. 6.4d). Flashback dynamics sequence is given only for the methane-air mixture at Φ=1.3 for 600K wall temperature in this thesis. Detailed information about other computation conditions can be found in our paper published in May 2022 in the *International Journal of Hydrogen Energy* [87].

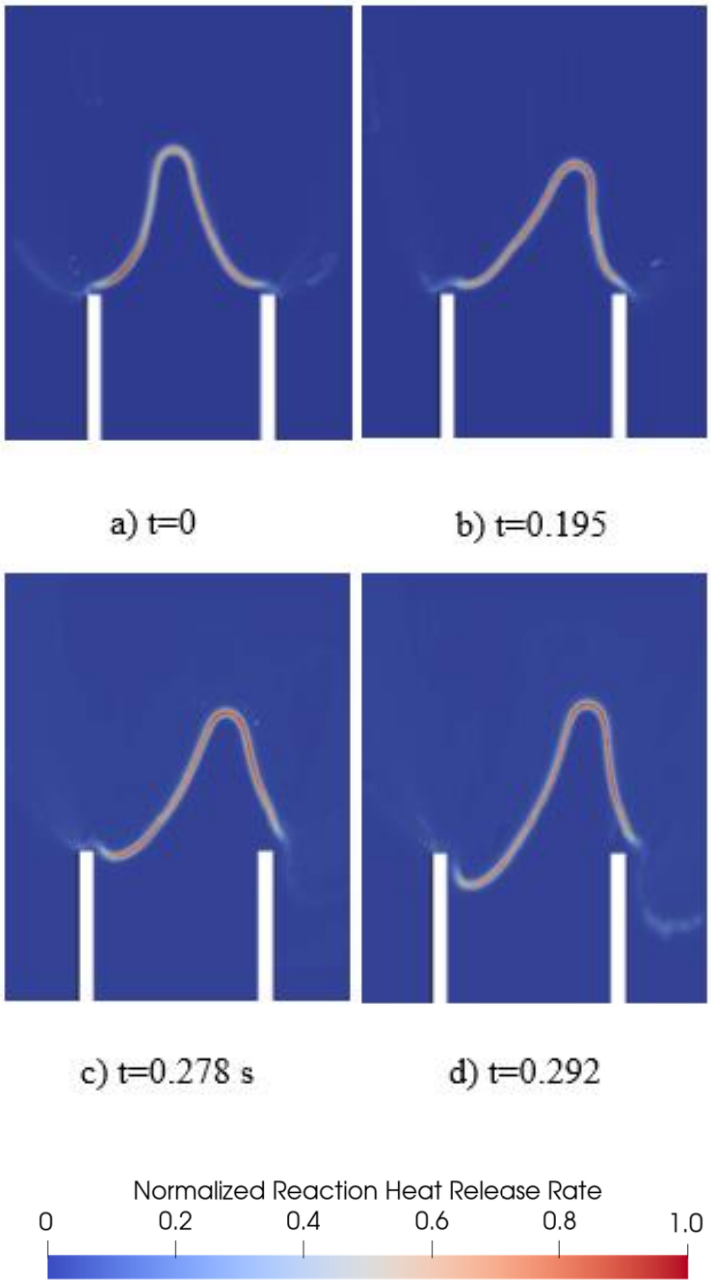

Figure 6.4. Flashback dynamics represented with the normalized reaction heat release rate contours for the methane-air mixture at Φ=1.3 for 600K wall temperature.

6.2.3 Hydrogen Addition Effect on the Quenching Distance

There are numerous estimation methods for the quenching distance in the literature. Using isocontours of 50% of the maximum OH* concentration or 50% of the maximum CH* concentration or the temperature that corresponds to the maximum gradient of the heat release rate [88] are a few examples. Normalized reaction heat release rate is used to examine quenching and penetration distances because it provides direct information about the reaction rate. Therefore, the quenching distance is determined by selecting the closest position to the wall where the normalized reaction heat release rate is 0.5. Fig. 6.5 illustrates the quenching and penetration lengths, as well as the leading edge, from an instantaneous snapshot of flashback for a 20% H_2 blend case with a wall temperature of 600K. A black line represents the isocontour of the normalized reaction heat release rate at a value of 0.5 on Fig. 6.5. The midpoint of the burner's exit is used as the origin for the coordinates in Figures 6.5 and 6.6. After the leading edge of each mixture composition has travelled 3 mm upstream of the burner exit, 10 successive snapshots of the normalized heat release rate are taken with a 1 ms time step for each mixture composition.

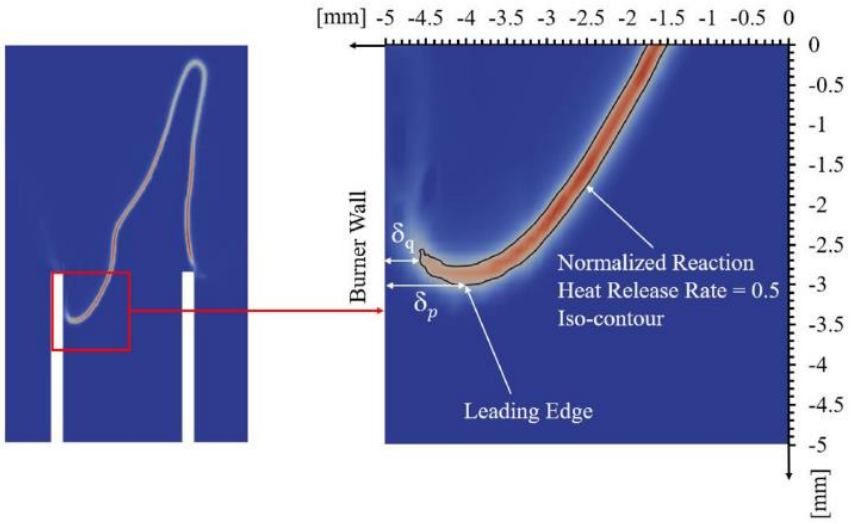

Figure 6.5. Representation of the quenching distance and the penetration distance at flashback for 20% H_2 addition rate at T=600K

The calculated quenching distances were first averaged and reported in Table 6.2. In accordance with earlier studies [85-86,89], the quenching distance has been found to decrease as H_2 is added. The combination containing 10% H_2 results in a 33% decrease in the quenching distance. A further 10% increase in the H_2 percentage of the fuel results in a lesser reduction (24%) in the quenching distance, showing that the effect is fading. Compared to hydrocarbon fuels, hydrogen has faster kinetics and higher reactivity [86,90]. These features of hydrogen lead to shorter quenching distances than those of hydrocarbon-based fuels. Thus, even a modest amount of hydrogen addition dramatically reduces the quenching distance and hence increases the flashback tendency.

Table 6.2 Variation of the average quenching distance with H_2 addition for T_{wall}=600K

H_2% [mol]	δ_q [mm]
0	0.86
10	0.58
20	0.44

6.2.4 Wall Temperature Effect

In this section, the influence of burner wall temperature is explored in further detail. According to Ref. [82], the heat transfer to the wall and the ensuring temperature distribution along the wall have a significant impact on the flashback limits. Changes in the molecular transport rates and reactivity caused by the thermal boundary layer close to the wall have a significant impact on flame dynamics and, consequently, flame curvature. With constant wall temperatures of 300K, 600K, and adiabatic wall conditions, numerical computations are performed. Figure 6.6a-c illustrates snapshots of the heat release rate of the methane-H_2-air flame at Φ=1.216 with 20% H_2 during the boundary layer flashback for the three distinct wall conditions.

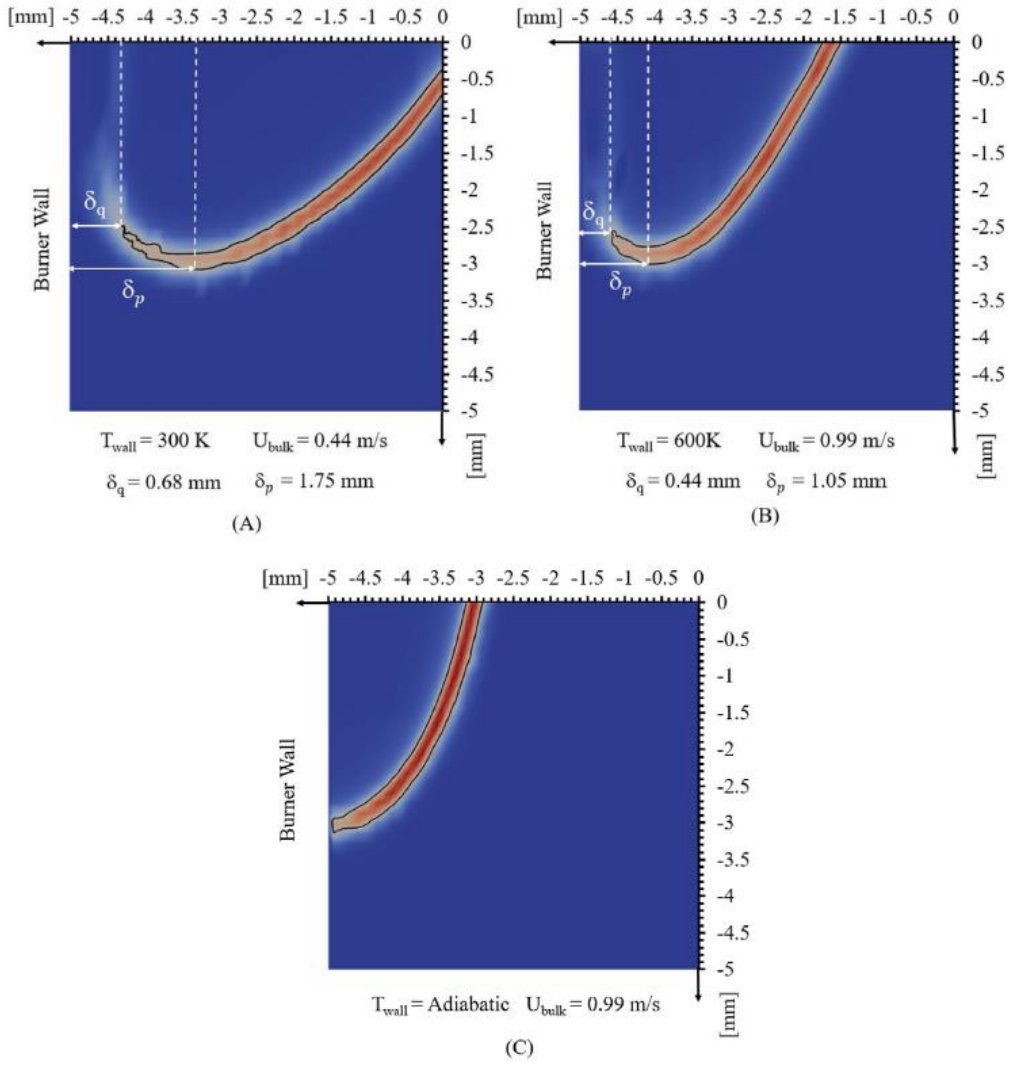

Figure 6.6. Normalized heat release rate contours for different wall temperature conditions for the CH_4-H_2- air flame at Φ =1.216 with 20% H_2 addition. A) T_{wall} = 300K B) T_{wall} = 600K C) Adiabatic

Compared to the 600K instance shown in Fig. 6.6b, the reaction rate near the wall is significantly reduced in the 300K case in Fig. 6.6a. As described in the previous section, the distances of quenching and penetration were computed. Both δ_q and δ_p decrease as the wall temperature increases from 300K to 600K. The decrease rates

of δ_q and δ_p are comparable, at 35% and 41%, respectively. Even though the laminar flame speeds at equivalent conditions are identical, a 35% decrease in δ_q leads in a 125% rise in the critical flashback limit from 0.44 m/s to 0.99 m/s. Thus, it is insufficient to describe the flashback limitations using just the laminar flame speed and the quenching distance, particularly for burners with high wall temperatures. As seen in Figure 6.6a-b, the curvature of the flashbacking flame increases near the leading edge. The curve of the stretched flame results in a higher local flame speed close to the leading edge, hence increasing the susceptibility for flashback. Contrary to the constant wall temperature situations, the quenching distance and leading-edge development are not detected in Fig. 6.6c for the adiabatic wall condition, in accordance with Kurdyumov et al. [82].

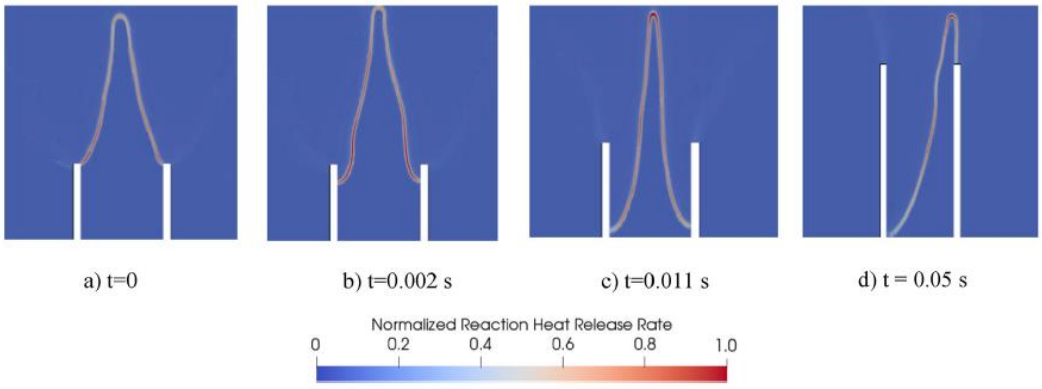

Figure 6.7. Flashback dynamics represented with the normalized heat release rate contours for methane-air flame at Φ = 1.216 with 20% H_2 addition rate at adiabatic wall condition.

Figure 6.7 illustrates the whole sequence of flashback dynamics for an adiabatic wall condition, which exhibits a markedly different behaviour from the isothermal wall situations for the identical mixture. The flame front is attached to the burner wall, unlike isothermal wall conditions, and the flashback times are drastically shorter. These results demonstrate that the adiabatic wall temperature condition does not represent the phenomenon of boundary layer flashback.

6.2.5 Flashback Limits

Fig. 6.8 compares the computed flashback limits to the measurements of de Vries et al. [81] and the correlations based on the critical gradient concept of von Elbe et al. [31], Putnam et al. [32], and Hoferichter et al. [33]. Once the flame has been stabilized in the experiments, the bulk inlet velocity is gradually decreased until flashback occurs. The experimental flashback limit defined as the bulk inlet velocity Uf just as the flame enters the burner tube.

In Fig. 6.8, the curves designate the flashback region below which the flashback is detected. The absolute values of the critical flashback velocity are shown in Figure 6.8a. When hydrogen is added to a mixture, the tendency for flashback has been shown to increase. This is because the laminar flame speed increases and the quenching distance decreases compared to pure hydrocarbon flames [86,88,90].

The predictions of the critical gradient concept model of von Elbe and the modified model of Hoferichter et al. [33] are similar; the modified model suggests flashback limits that are closer to the experimental results. As the amount of hydrogen added to the fuel mixture increases, the critical gradient concept correlations diverge since flame stretch becomes more significant. Putnam's correlation estimates deviate the most from experimental results. It may be explained as Putnam’s model, which is based on the theory of Lewis and von Elbe, is only validated for ethylene/air and acetylene/oxygen mixes. The Lewis and von Elbe model is based on experimental data regarding the combustion of natural gas and hydrogen in air.

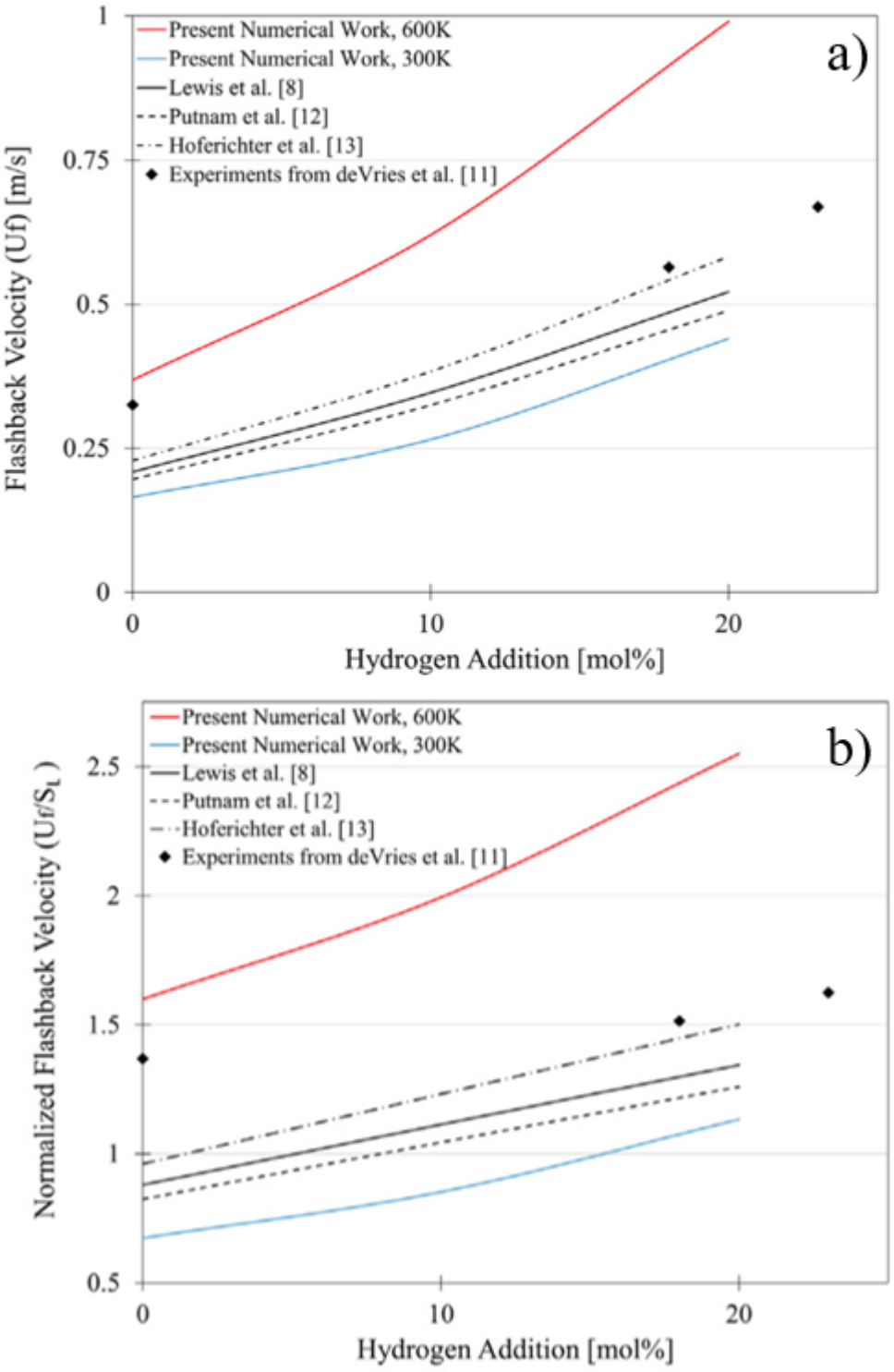

Figure 6.8. Comparison of experimental and calculated flashback limits

The experimental results fall between our numerical results for 600K and 300K constant wall temperatures. Comparing the correlations between numerical results for 300K and the critical gradient theory demonstrates that flashback limits are comparable. The results of de Vries et al. [81] exceed the predictions of the model for all hydrogen addition rates at 300K wall temperature. This may be related to the quartz burner used in de Vries et al. [81]. Due to the low thermal conductivity of the quartz, the experimented wall temperature may have increased locally at the rim. This reduces the quenching distance, hence increasing the discrepancy between the actual quenching distance and the value employed in the correlations.

Figure 6.8b displays the same data normalized by the calculated laminar flame speed (SL) for each mixing condition. Notably, all correlations and the 300K wall temperature instances underestimate the normalized flashback velocity for a pure methane flame, but the 600K wall temperature calculations overestimate it. Experimentally, the normalized critical flame flashback velocity is more than 1 and increases with the addition of hydrogen. All correlations and calculations for 300K wall temperature exhibit the same trend, particularly above an H_2 addition rate of 10% molar. Similarly, 600K wall temperature calculations follow the similar trend, albeit with greater critical flame flashback velocities. This observation appears to contradict the straightforward definition of the boundary layer flashback critical velocity as being only related to the laminar flame propagation speed for hydrogen-added methane flames and requires additional investigation.

CHAPTER 7

CONCLUSIONS AND FUTURE WORK

7.1 Conclusions

In this work, laminar spherically expanding flames of NG-air and NG-air mixtures with H_2 addition in a spherical combustion chamber are investigated both experimentally and numerically. The experiments are performed at atmospheric conditions with H_2 addition rates of up to 20% for lean and stoichiometric conditions (Φ=0.6, 0.8, 1). To investigate spherical flame propagation experimentally, a spherical combustion chamber is designed, manufactured, installed, and commissioned. Experiments were performed at 1 bar, 288 ± 2K. The Schlieren method is used to visualize spherically expanding flames, and recorded images are post-processed by fitting an ellipse to the flame front. Stretched laminar burning velocities are deduced from flame front radius raw data fitted using both polynomial and differential equation fitting methods. Deviations between different order polynomial fits are illustrated and differential equation fitting method is applied. Linear methodology is used to extrapolate stretched laminar burning velocity to zero stretch. Unstretched laminar flame speeds are deduced using the expansion rates computed from 1D simulations and used to determine unstretched laminar flame burning velocities. Laminar flame speeds of mixtures are obtained by averaging 3 successful experiments under same conditions and standard deviations are presented. Deviations between the experiments are within the experimental uncertainties. The results for Φ =1 with 20% H_2 addition are not presented since acceptable flame propagation images could not be obtained. It is shown that the laminar flame speed of NG-air mixtures increases with hydrogen addition and increasing equivalence ratio from 0.6 to 1. Present experimental results are compared with the results from the literature obtained by heat flux and spherically expanding flame methods.

Generally, present results are in good agreement with the literature and 1D computations within the limits of our measurement uncertainties. The experiments were performed by assuming that the used NG gas mixture is composed of CH4 with a molar fraction higher than 95%. However, after the experiments were performed, the composition of the NG mixture is checked using the gas chromatography method. The CH4 molar concentration is found about 88%. The uncertainties occasioned for the mixture equivalence ratio and the laminar flame speeds are estimated.

1D computations were performed for NG-air mixtures at 288K and 300K to observe the temperature effect on laminar flame speed data. It is found that the laminar flame speed increases with increasing temperature. Also, the actual NG-air and CH4-air mixtures are compared at 300K to observe the effect of fuel composition at the same temperature. Results show that laminar flame speeds of NG-air mixtures are higher than CH4-air mixtures and deviations between them decreases with increasing hydrogen addition rate. Markstein lengths are determined and compared with the literature results. It is found that Markstein lengths increase with increasing equivalence ratio and decrease with the hydrogen addition rate. This implies that flame sensitivity to stretch decreases up to 20% hydrogen addition rate to lean and stoichiometric NG-air laminar flames. It is also observed that adding 20% hydrogen does not result in negative Markstein lengths, even in the leanest case.

In addition to 1D CANTERA/CHEMKIN simulations, 2D simulations were performed to investigate spherically expanding flames numerically. The GRIMECH 3.0 chemical kinetic mechanism is used for both simulations. 2D transient, finite volume simulations were performed with the OpenFOAM numerical framework, taking multispecies transport into account. A mesh independence study is performed, and a 50 μm grid size is used in a fully hexahedral mesh. To reduce computational time, only a quarter of the domain is modelled, assuming that the flame is perfectly symmetric. The calculations were performed for CH4-air mixtures at 300K under atmospheric pressure conditions. The flame radius for each time step is extracted by taking the average of the distances of each point to the center on a temperature isocontour. Laminar flame speeds were calculated by applying the same

methodology as in the experiments. Confinement effect is investigated by changing the boundary of the computational domain (from freely propagating to wall-confined). It is found that, laminar flame speed decreases when the flame is confined, and the confinement effect is less apparent with H_2 addition rate.

Additionally, laminar boundary layer flashback phenomenon is investigated numerically for CH4-air and CH4-H_2-air mixtures. Experimental work of deVries et al. (2015) is modelled in 2D. Flashback dynamics were investigated, and the asymmetrical nature of the laminar boundary layer flashback is observed. Flashback limits were calculated by decreasing the cold premixture inlet flow velocity by steps of 5% and results were compared with the experimental results and theoretical models. The effect of H_2 addition on flashback limits were also investigated and it is found that flashback propensity increases with the increase of H_2 addition to the mixture. The wall temperature effect on flashback propensity is investigated by applying 300K and 600K isothermal wall conditions. Importance of the wall temperature on boundary layer flashback is discussed and it is found that flashback propensity increases with increasing wall temperature. Change in the flame quenching distance is investigated with H_2 addition to the premixture and it is shown that the quenching distance is decreasing with the addition of H_2. The discrepancy observed in the literature between the experimental flashback limits and the numerical ones can be attributed to the use of inaccurate wall temperature conditions. Assuming a uniform wall temperature may not represent the exact flame flashback dynamics. Furthermore, simplification of the geometry to 2D may induce additional errors in computations.

7.2 Future Work

In this work, an experimental facility is designed, manufactured, installed, commissioned, operated and the first results are obtained. The suggested *improvements on the experimental setup and future experimental work recommendations* are as follows:

- A fast response pressure transducer should be flash-mounted on one of the high pressure flanges. This is required to obtain the chamber pressure history accurately during the flame propagation process. This will also reduce the uncertainties in adjusting the partial pressures of the various gases in the combustion chamber, since more accurate pressure readings will be possible.
- A pressure transducer with higher accuracy should be used in order to reduce the equivalence ratio uncertainties. Moreover, needle valves should be replaced with high accuracy flow meters to eliminate the human errors during reactive mixture preparation.
- Due to angles of the flat mirrors used in the imaging system, it is really hard to obtain a perfectly spherical shape for Schlieren images. The experimental setup should be placed in a more convenient area, where the flat mirrors can be eliminated from the system.
- Ignitors with sharper edges will increase the sphericity of the flames, which should be manufactured since the last pair is broken during the final experiments.
- Ignition characteristics of NG-air and NG-H_2-air mixtures can be studied with a more advanced ignition system. This system should precisely supply the desired voltage in order to reduce the initial excess energy deposit. In this way, initial flame front radius values below 10 mm can be used to gather more data points away from the chamber walls.
- The ignition system and the camera should be fully automated (camera should start recording automatically when ignition is triggered), in order to perform experiments in a more convenient way.

- During the experiments, a crack was initiated from the contact point of the high-pressure quartz window and the window holder. Experiments were continued with another tempered glass window which can only withstand experiments up to 25 bars. New high pressure quartz windows should be integrated to the combustion chamber and the reason of the crack initiation should be investigated in detail.
- High pressure experiments should be performed for the mixtures investigated in this work. There is indeed limited amount of high pressure premixed laminar flame speed data available in the literature.
- Experiments should be performed with the corrected partial pressure values of NG-air and NG-H_2-air mixtures, using the actual NG composition.
- Hydrogen addition rates to the NG-air mixtures should be increased. Syngas and biogas mixtures can also be investigated.
- In this work, only diffusion mixing is used to constitute the reactive mixture. A mixing chamber should be designed in order to obtain a more homogeneous mixture.

Concerning 2D numerical simulations:

- Laminar flame thickness evolution of the spherically expanding flames should be investigated.
- Velocity field data may be extracted from the computations and used for comparison with the laminar flame burning velocities obtained by using the flame front radius evolution data.
- Reasons behind the lack of deviation between the laminar flame speeds for the confined and freely propagating flame configurations at Φ =0.8 and %20 H2 addition rate should be investigated.

For boundary layer flashback computations:

- Inclusion of the Soret effect into the numerical computations would enhance the accuracy of the flashback limit calculations, especially for high hydrogen addition rates.
- 3D investigations of laminar boundary layer flashback phenomenon will provide additional insights for the flashback dynamics. The accuracy of the 2D assumption should also be validated further.
- Since burner wall temperatures have a great effect on flashback limits, the conjugate heat transfer approach at the burner walls should be investigated.

REFERENCES

[1] World energy outlook. Paris, 2010.

[2] Bouvet, N., Chauveau, C., Gökalp, I., Halter, F. (2011) Experimental studies of the fundamental flame speeds of syngas (H2/CO)/air mixtures. Proc. of the Combustion Institute 33: 913-920. https://doi.org/10.1016/j.proci.2010.05.088

[3] Bouvet, N., Chauveau, C., Gökalp, I., Lee, S.-Y., Santoro R.J. (2011) Characterization of syngas laminar flames using the Bunsen burner configuration. International Journal of Hydrogen Energy 36: 992-1005. https://doi.org/10.1016/j.ijhydene.2010.08.147

[4] Yılmaz, B., Özdogan, S., Gökalp, I. (2010) Influence of hydrogen addition on lean premixed methane-air flame statistics. Proc. of the ASME 10th Biennal Conference on Engineering Systems Design and Analysis 4:281-287 . DOI:10.1115/ESDA2010-25375

[5] Cohé, C., Halter, F., Chauveau, C., Gökalp,I., Gülder, Ö.L. (2007) Fractal characterization of high pressure and hydrogen enriched CH4-Air turbulent premixed flames. Proc. of the Combustion Institute 31: 1345-1352. doi:10.1016/j.proci.2006.07.181

[6] Halter, F., Chauveau, C., Gökalp, I. (2007) Characterization of the effects of hydrogen addition in premixed methane/air flames. Int. J. Hydrogen Energy 32: 2585-2592. https://doi.org/10.1016/j.ijhydene.2006.11.033

[7] Halter, F., Chauveau, C., Djebaili-Chaumeix, N., Gökalp, I. (2005) Characterization of the effects of pressure and hydrogen concentration on laminar burning velocities of methane-hydrogen-air mixtures. Proc. of the Combustion Institue 30: 201-208. DOI : 10.1016/j.proci.2004.08.195

[8] Gökalp, I. (2019) A holistic approach to promote the safe development of hydrogen as an energy vector. Proceedings of the Ninth International Seminar on

Fire and Explosion Hazards. Vol. 2: 21-26 April 2019, Saint Petersburg, Russia, DOI 10.18720/SPBPU/2/k19-127

[9] Anderson, J. D. (2011). Fundamentals of Aerodynamics (5th ed.). New York: McGraw-Hill.

[10] Pope, S. B. (2000). Turbulent flows. Cambridge, UK: Cambridge University Press.

[11] Law, C. K., & Sung, C. J. (2000). Structure, aerodynamics, and geometry of premixed flamelets. Progress in energy and combustion science, 26(4-6), 459-505.

[12] Zeldovich, Y. B., & Frank-Kamenetskii, D. A. (1938). The theory of thermal propagation of flames. Zh. Fiz. Khim, 12, 100-105.

[13] Mallard, E., & Le Chatelier, H. (1881). Sur la vitesse de propagation de l'inflammation dans les melanges explosifs. Comptes rendus de l'Academie des Science, Paris, 93-145.

[14] Turns, Stephen. (1996). An Introduction To Combustion: concepts and applications. MCGRAW-HILL EDUCATION.

[15] Peters, N. (2000). Turbulent combustion. Cambridge Monographs on Mechanics. Cambridge, UK: Cambridge University Press.

[16] Alexander A. Konnov, Akram Mohammad, Velamati Ratna Kishore, Nam Il Kim, Chockalingam Prathap, Sudarshan Kumar, A comprehensive review of measurements and data analysis of laminar burning velocities for various fuel+air mixtures, Progress in Energy and Combustion Science, Volume 68, 2018, Pages 197-267, ISSN 0360-

[17] Williams, F. A. (1985). Combustion theory (2nd ed.). Boca Raton, FL: CRC Press. https://doi.org/10.1201/9780203881047

[18] Matalon, M. (1983). On flame stretch. Combustion Science and Technology, 31, 169-181.

[19] Candel, S., & Poinsot, T. (1990). Flame stretch and the balance equation for the flame area. Combustion Science and Technology, 70, 1-15.

[20] Seshadri, K., Peters, N., & Williams, F. (1994). Asymptotic analyses of stoichiometric and lean hydrogen-air flames. Combustion and Flame, 96(4), 407-427.

[21] Clavin, P. (1985). Dynamic behavior of premixed flame fronts in laminar and turbulent flows. Progress in Energy and Combustion Science, 11(1), 1-59.

[22] Law, C. K. (1988). Dynamics of stretched flames. In 22nd Symp (Int.) on Combustion (pp. 1381-1402).

[23] Williams, P., & Williams, F. (1987). Premixed flames with general rates of strain. Combustion Science and Technology, 54, 237.

[24] Hummel, J. R., Eitel, D. A., & Williams, F. A. (2001). Flame stretch and flamelet structure in nonpremixed turbulent flames. Combustion and Flame, 124(1-2), 118-141.

[25] Markstein, G. H. (1964). Non-steady flame propagation. New York: Pergamon.

[26] Chen, Z. (2010). Effects of radiation and compression on propagating spherical flames of methane/air mixtures near the lean flammability limit. *Combustion and flame*, *157*(12), 2267-2276.

[27] Wu, F., Liang, W., Chen, Z., Ju, Y., & Law, C. K. (2015). Uncertainty in stretch extrapolation of laminar flame speed from expanding spherical flames. Proceedings of the Combustion Institute, 35(1), 663-670.

[28] Han, W., Dai, P., Gou, X., & Chen, Z. (2020). A review of laminar flame speeds of hydrogen and syngas measured from propagating spherical flames. *Applications in Energy and Combustion Science*, *1*, 100008.

[29] Lieuwen, T. C. (2012). Unsteady Combustor Physics Cambridge University Press. *Cambridge, UK*.

[30] Jones, D. R., Al-Masry, W. A., & Dunnill, C. W. (2018). Hydrogen-enriched natural gas as a domestic fuel: an analysis based on flash-back and blow-off limits for domestic natural gas appliances within the UK. *Sustainable Energy & Fuels*, *2*(4), 710-723.

[31] Lewis, B., & von Elbe, G. (1943). Stability and Structure of Burner Flames. The Journal of Chemical Physics, 11(2), 75–97. https://doi.org/10.1063/1.1723808

[32] Putnam, A. A., Ball, D. A., & Levy, A. (1980). Effect of fuel composition on relation of burning velocity to product of quenching distance and flashback velocity gradient. Combustion and Flame, 37, 193–196. https://doi.org/10.1016/0010-2180(80)90085-1

[33] Hoferichter, V. et al. (2018). Prediction of boundary layer flashback limits of laminar premixed jet flames. Combustion, Fuels, and Emissions. doi:10.1115/gt2018-75546

[34] Wu, Y. (2016). Experimental investigation of laminar flame speeds of kerosene fuel and second generation biofuels in elevated conditions of pressure and preheat temperature (Doctoral dissertation, Rouen, INSA).

[35] Vagelopoulos, C. M., Egolfopoulos, F. N., & Law, C. K. (1994, January). Further considerations on the determination of laminar flame speeds with the counterflow twin-flame technique. In Symposium (international) on combustion (Vol. 25, No. 1, pp. 1341-1347). Elsevier.

[36] Egolfopoulos, F. N., Cho, P., & Law, C. K. (1989). Laminar flame speeds of methane-air mixtures under reduced and elevated pressures. Combustion and flame, 76(3-4), 375-391.

[37] Van Maaren, A., & De Goey, L. P. H. (1994). Stretch and the adiabatic burning velocity of methane-and propane-air flames. Combustion Science and Technology, 102(1-6), 309-314.

[38] Bosschaart, K. J., & De Goey, L. P. H. (2003). Detailed analysis of the heat flux method for measuring burning velocities. Combustion and flame, 132(1-2), 170-180.

[39] Hermanns, R. T. E. (2007). Laminar burning velocities of methane-hydrogen-air mixtures.

[40] Hinton, N. I. (2014). Measuring laminar burning velocities using constant volume combustion vessel techniques (Doctoral dissertation, Oxford University).

[41] Goswami, M., Van Griensven, J. G. H., Bastiaans, R. J. M., Konnov, A. A., & De Goey, L. P. H. (2015). Experimental and modeling study of the effect of elevated pressure on lean high-hydrogen syngas flames. *Proceedings of the Combustion Institute*, *35*(1), 655-662.

[42] Lewis B, Von Elbe G (2012) Combustion, flames and explosions of gases. Elsevier, London

[43] Varea, E. (2013). *Experimental analysis of laminar spherically expanding flames* (Doctoral dissertation, Rouen, INSA).

[44] Egolfopoulos, F. N., Hansen, N., Ju, Y., Kohse-Höinghaus, K., Law, C. K., & Qi, F. (2014). Advances and challenges in laminar flame experiments and implications for combustion chemistry. *Progress in Energy and Combustion Science*, *43*, 36-67.

[45] Lewis, B., & Von Elbe, G. (1934). Determination of the speed of flames and the temperature distribution in a spherical bomb from time-pressure explosion records. *The Journal of Chemical Physics*, *2*(5), 283-290.

[46] Faghih, M., & Chen, Z. (2016). The constant-volume propagating spherical flame method for laminar flame speed measurement. *Science Bulletin*, *61*(16), 1296-1310.

[47] Halter, F., Chen, Z., Dayma, G., Bariki, C., Wang, Y., Dagaut, P., & Chauveau, C. (2020). Development of an optically accessible apparatus to characterize the

evolution of spherically expanding flames under constant volume conditions. *Combustion and Flame*, *212*, 165-176.

[48] Hu, E., Huang, Z., He, J., Jin, C., & Zheng, J. (2009). Experimental and numerical study on laminar burning characteristics of premixed methane–hydrogen–air flames. *international journal of hydrogen energy*, *34*(11), 4876-4888.

[49] Tse, S. D., Zhu, D. L., & Law, C. K. (2000). Morphology and burning rates of expanding spherical flames in H2/O2/inert mixtures up to 60 atmospheres. *Proceedings of the combustion institute*, *28*(2), 1793-1800.

[50] Qin, X., & Ju, Y. (2005). Measurements of burning velocities of dimethyl ether and air premixed flames at elevated pressures. *Proceedings of the Combustion Institute*, *30*(1), 233-240.

[51] Kelley, A. P., Jomaas, G., & Law, C. K. (2009). Critical radius for sustained propagation of spark-ignited spherical flames. *Combustion and Flame*, *156*(5), 1006-1013.

[52] Van Maaren, A., & De Goey, L. P. H. (1994). Stretch and the adiabatic burning velocity of methane-and propane-air flames. *Combustion Science and Technology*, *102*(1-6), 309-314.

[53] Yu, G., Law, C. K., & Wu, C. K. (1986). Laminar flame speeds of hydrocarbon+ air mixtures with hydrogen addition. *Combustion and flame*, *63*(3), 339-347.

[54] Dirrenberger, P., Le Gall, H., Bounaceur, R., Herbinet, O., Glaude, P. A., Konnov, A., & Battin-Leclerc, F. (2011). Measurements of laminar flame velocity for components of natural gas. *Energy & fuels*, *25*(9), 3875-3884.

[55] Tang, C. L., Huang, Z. H., & Law, C. K. (2011). Determination, correlation, and mechanistic interpretation of effects of hydrogen addition on laminar flame speeds of hydrocarbon–air mixtures. *Proceedings of the combustion institute*, *33*(1), 921-928.

[56] Poinsot, T., & Veynante, D. (2005). *Theoretical and numerical combustion*. RT Edwards, Inc.

[57] Goodwin, D. G., Moffat, H. K., & Speth, R. L. (2009). Cantera: An object-oriented software toolkit for chemical kinetics, thermodynamics, and transport processes. *Caltech, Pasadena, CA, 124*.

[58] CHEMKIN-PRO 15112, Reaction Design: San Diego, 2011.

[59] Settles, G. S. (2001). *Schlieren and shadowgraph techniques: visualizing phenomena in transparent media*. Springer Science & Business Media.

[60] Smits, A. J. (2012). *Flow visualization: techniques and examples*. World Scientific.

[61] Clavin, P., & Joulin, G. (1983). Premixed flames in large scale and high intensity turbulent flow. *Journal de Physique Lettres*, *44*(1), 1-12.

[62] Law, C. K. (1989). Dynamics of stretched flames. In *Symposium (international) on combustion* (Vol. 22, No. 1, pp. 1381-1402). Elsevier.

[63] Peters, N. (1986). Turbulent combustion. Proceedings of the Combustion Institute, 21, 1231-1250.

[64] Dowdy, D. R., Smith, D. B., Taylor, S. C., & Williams, A. (1991). The use of expanding spherical flames to determine burning velocities and stretch effects in hydrogen/air mixtures. In *Symposium (International) on Combustion* (Vol. 23, No. 1, pp. 325-332). Elsevier.

[65] Brown, M. J., McLean, I. C., Smith, D. B., & Taylor, S. C. (1996). Markstein lengths of CO/H2/air flames, using expanding spherical flames. In *Symposium (International) on Combustion* (Vol. 26, No. 1, pp. 875-881). Elsevier.

[66] Tahtouh, T., Halter, F., & Mounaïm-Rousselle, C. (2009). Measurement of laminar burning speeds and Markstein lengths using a novel methodology. *Combustion and Flame*, *156*(9), 1735-1743.

[67] Halter, F. (2005). Caractérisation des effets de l'ajout d'hydrogène et de la haute pression dans les flammes turbulentes de prémélange méthane/air (Doctoral dissertation, Université d'Orléans).

[68] Kelley, A. P., & Law, C. K. (2009). Nonlinear effects in the extraction of laminar flame speeds from expanding spherical flames. Combustion and Flame, 156(9), 1844–1851. https://doi.org/10.1016/j.combustflame.2009.04.004

[69] Halter, Fabien, Toni Tahtouh, and Christine Mounaïm-Rousselle. "Nonlinear effects of stretch on the flame front propagation." *Combustion and Flame* 157.10 (2010): 1825-1832.

[70] Zhang, F., Bonart, H., Zirwes, T., Habisreuther, P., Bockhorn, H., & Zarzalis, N. (2014). Direct Numerical Simulation of Chemically Reacting Flows with the Public Domain Code OpenFOAM. High Performance Computing in Science and Engineering '14, 221–236. https://doi.org/10.1007/978-3-319-10810-0_16

[71] Zhong, S., Zhang, F., Peng, Z., Bai, F., & Du, Q. (2018). Roles of CO2 and H2O in premixed turbulent oxy-fuel combustion. Fuel, 234, 1044–1054. DOI:10.1016/j.fuel.2018.07.135

[72] Holzmann, Tobias. (2019). Mathematics, Numerics, Derivations and OpenFOAM®.

[73] Gregory P. Smith, David M. Golden, Michael Frenklach, Nigel W. Moriarty, Boris Eiteneer, Mikhail Goldenberg, C. Thomas Bowman, Ronald K. Hanson, Soonho Song, William C. Gardiner, Jr., Vitali V. Lissianski, and Zhiwei Qin http://www.me.berkeley.edu/gri_mech/

[74] Contino, F., Jeanmart, H., Lucchini, T., & D'Errico, G. (2011). Coupling of in situ adaptive tabulation and dynamic adaptive chemistry: An effective method for solving combustion in engine simulations. Proceedings of the Combustion Institute, 33(2), 3057–3064. https://doi.org/10.1016/j.proci.2010.08.002

[75] Pope, S. B. (1997). Computationally efficient implementation of combustion chemistry usingin situadaptive tabulation. Combustion Theory and Modelling, 1(1), 41–63. https://doi.org/10.1080/713665229

[76] Liang, L., Stevens, J. G., Raman, S., & Farrell, J. T. (2009). The use of dynamic adaptive chemistry in combustion simulation of gasoline surrogate fuels. Combustion and Flame, 156(7), 1493–1502. https://doi.org/10.1016/j.combustflame.2009.02.008

[77] Atkins, P., & de Paula, J. (2006). Atkins' physical chemistry (8th ed.). Oxford University Press.

[78] Bradley, D., Gaskell, P. H., & Gu, X. J. (1996). Burning velocities, Markstein lengths, and flame quenching for spherical methane-air flames: a computational study. *Combustion and flame*, *104*(1-2), 176-198.

[79] Clarke, A., & Hargrave, G. K. (2009). Measurements of laminar premixed methane—air flame thickness at ambient conditions. *Proceedings of the Institution of Mechanical Engineers, Part C: Journal of Mechanical Engineering Science*, *223*(8), 1969-1973.

[80] Chen, Z. (2015). On the accuracy of laminar flame speeds measured from outwardly propagating spherical flames: Methane/air at normal temperature and pressure. *Combustion and Flame*, *162*(6), 2442-2453.

[81] de Vries, H., Mokhov, A. V., & Levinsky, H. B. (2017). The impact of natural gas/hydrogen mixtures on the performance of end-use equipment: Interchangeability analysis for domestic appliances. *Applied energy*, *208*, 1007-1019.

[82] Kurdyumov, V., Fernandez-Tarrazo, E., Truffaut, J. M., Quinard, J., Wangher, A., & Searby, G. (2007). Experimental and numerical study of premixed flame flashback. *Proceedings of the Combustion Institute*, *31*(1), 1275-1282.

[83] Dam, B., Love, N., & Choudhuri, A. (2011). Flashback propensity of syngas fuels. *Fuel*, *90*(2), 618-625.

[84] Duan, Z., Shaffer, B., & McDonell, V. (2013). Study of Fuel Composition, Burner Material and Tip Temperature Effects on Flashback of Enclosed Jet Flame. Volume 1A: Combustion, Fuels and Emissions. https://doi.org/10.1115/gt2013-94822

[85] Vance, F. H., de Goey, L. P. H., & van Oijen, J. A. (2022). Development of a flashback correlation for burner-stabilized hydrogen-air premixed flames. *Combustion and Flame*, 112045.

[86] Kalantari, A., & McDonell, V. (2017). Boundary layer flashback of non-swirling premixed flames: Mechanisms, fundamental research, and recent advances. Progress in Energy and Combustion Science, 61, 249–292. https://doi.org/10.1016/j.pecs.2017.03.001

[87] Kıymaz, T. B., Böncü, E., Güleryüz, D., Karaca, M., Yılmaz, B., Allouis, C., & Gökalp, İ. (2022). Numerical investigations on flashback dynamics of premixed methane-hydrogen-air laminar flames. *International Journal of Hydrogen Energy*, *47*(59), 25022-25033.

[88] Zirwes, T., Häber, T., Zhang, F., Kosaka, H., Dreizler, A., Steinhausen, M., ... & Bockhorn, H. (2021). Numerical study of quenching distances for side-wall quenching using detailed diffusion and chemistry. *Flow, Turbulence and Combustion*, *106*(2), 649-679.

[89] Ebi, D., Bombach, R., & Jansohn, P. (2021). Swirl flame boundary layer flashback at elevated pressure: Modes of propagation and effect of hydrogen addition. *Proceedings of the Combustion Institute*, *38*(4), 6345-6353.

[90] Crabtree, R. H. (2001). Alkane C–H activation and functionalization with homogeneous transition metal catalysts: A century of progress—A new millennium in prospect. *Journal of the Chemical Society, Dalton Transactions*, (17), 2437-2450.

APPENDICES

A. MATLAB Code for Curve Fitting

```
rng default % for reproducibility

filename = 'neq1_1.xlsx';
columnB = xlsread(filename,'B105:B230');
columnC = xlsread(filename,'C105:C230');

tdata = columnB.';
rdata = columnC.';

fun = @(x)sseval(x,tdata,rdata);

x0 = [1;0.1;5];
bestx = fminsearch(fun,x0)

Vs0 = bestx(1);
Lb = bestx(2);
C1 = bestx(3);
Z=exp((Vs0*tdata+C1)/(2*Lb))/(2*Lb);
W0=lambertw(Z);
yfit = 2*Lb*W0;

plot(tdata,rdata,'*');
hold on
plot(tdata,yfit,'r');
xlabel('Time(ms)')
ylabel('Radius(mm)')
title('Data and Best Fitting Curve')
legend('Data','Fitted Curve')
hold off

function sse = sseval(x,tdata,rdata)
Vs0 = x(1);
Lb = x(2);
C1 = x(3);
Z=exp((Vs0*tdata+C1)/(2*Lb))/(2*Lb);
W0=lambertw(Z);
sse = sum((rdata - 2*Lb*W0).^2);

end
```

B. Python Code for Image Processing

```
from dataclasses import field
import math
import cv2 as cv
import numpy as np
import csv
CONTOURS = False
# Colors used. (Blue, Green, Red) each value in range [0, 255]
ELLIPSE_COLOR = (0, 255, 0)
CENTER_COLOR = (0, 0, 255)
FONT_FG_COLOR = (0, 0, 0)
FONT_BG_COLOR = (255, 255, 255)
FONT = cv.FONT_HERSHEY_TRIPLEX
FONT_SCALE = 0.5  # Text size
FONT_THICKNESS = 1
FONT_PADDING = 5
NUM_POINTS_ON_ELLIPSE = 10
APERTURE_IN_MM = 70
MS_PER_FRAME = 0.04167
# Definition of mathematical expressions for image processing
class Point:

  def __init__(self, x, y=None):
    if type(x) == tuple:
      self.x, self.y = x
    else:
      self.x = x
      self.y = y
  def GetFloat(self):
    return (self.x, self.y)
```

```
  def GetInt(self):
    return (int(self.x), int(self.y))
  def GetHalf(self):
    return (int(self.x / 2), int(self.y / 2))
  def __sub__(self, other):
    return (self.x - other.x, self.y - other.y)
  def __add__(self, other):
    return (self.x + other.x, self.y + other.y)
  def __mul__(self, scalar):
    return (self.x * scalar, self.y * scalar)
  def Length(self):
    return math.sqrt((self.x * self.x) + (self.y * self.y))
  def TopRight(self, pad=(FONT_PADDING, FONT_PADDING)):
    return Point(self.x + pad[0], self.y - pad[1])
def WriteText(image, text, where, thickness=FONT_THICKNESS):
  (text_width, text_height), baseline = cv.getTextSize(text, FONT, FONT_SCALE,
thickness)
  bottom_left = where.TopRight()
  top_right = bottom_left.TopRight((text_width + FONT_PADDING, text_height +
FONT_PADDING))
  # Draw background rectangle
  cv.rectangle(image, bottom_left.GetInt(), top_right.GetInt(), FONT_BG_COLOR,
cv.FILLED)
  # Draw actual text in rectangle
  cv.putText(image,
          text,
          bottom_left.TopRight().GetInt(),
          FONT,
          FONT_SCALE,
          FONT_FG_COLOR,
          FONT_THICKNESS,
          lineType=cv.LINE_AA)
```

```
  return (top_right.x - bottom_left.x, bottom_left.y - top_right.y)
def GetPixelRatio(first_frame):
  # Determination of pixel distances for radius calculations.
  grayscale = cv.cvtColor(first_frame, cv.COLOR_BGR2GRAY)
  blurred = cv.medianBlur(grayscale, 11)
  _, threshed = cv.threshold(blurred, 20 , 255, cv.THRESH_OTSU)
  #cv.imshow("PixelRatio", threshed )
  #cv.waitKey(0)
  closed = cv.morphologyEx(threshed, cv.MORPH_CLOSE, np.ones((15, 15), np.uint8))
  #cv.imshow("PixelRatio", closed)
  #cv.waitKey(0)
  contours, hier = cv.findContours(closed, cv.RETR_EXTERNAL, cv.CHAIN_APPROX_NONE)
  # contours[0].squeeze()
  rotrect = cv.fitEllipse(contours[0].reshape(contours[0].shape[0], 2))
  center = Point(rotrect[0])
  axes = Point(rotrect[1])
  angle = int(rotrect[2])
  viewport_radius = np.mean(axes.GetFloat()) / 2
  pixel_ratio = (APERTURE_IN_MM / 2) / viewport_radius

  return pixel_ratio
def ProcessVid(video_name, outfile_name):
  # create the csv file to output. If it exists overwrite the data.
  outfile = open(outfile_name, 'w')
  csv_writer = csv.DictWriter(outfile, fieldnames=['Frame No', 'Millisecond (Real)', 'Avg. Radius'])
  csv_writer.writeheader()
  # Choose a background subtractor.
  background_subtractor = cv.createBackgroundSubtractorMOG2(history=150, varThreshold=20, detectShadows=True)
```

```
#background_subtractor = cv.createBackgroundSubtractorKNN(history=100, dist2Threshold=50, detectShadows=False)

# Open video file
video_file = cv.VideoCapture(video_name)
frame_width = video_file.get(cv.CAP_PROP_FRAME_WIDTH)
frame_height = video_file.get(cv.CAP_PROP_FRAME_HEIGHT)
_, first_frame = video_file.read()
video_file.set(cv.CAP_PROP_POS_FRAMES, 0)
DIST_PER_PIXEL = GetPixelRatio(first_frame)

# Process all frames in a video
while True:
  next_frame_available, frame = video_file.read()
  if not next_frame_available or frame is None:
    # Video finished, exit loop
    video_file.release()
    outfile.close()
    break
  # Get frame no and frame ms
  frame_no = video_file.get(cv.CAP_PROP_POS_FRAMES)
  frame_ms = video_file.get(cv.CAP_PROP_POS_MSEC)
  avg_radius = -1  # -1 for empty frames

  # Create a grayscale copy of frame
  frame_gray = cv.cvtColor(frame, cv.COLOR_BGR2GRAY)
  # Apply the background subtractor and get the foreground

  detection_im = background_subtractor.apply(frame_gray)
  # Apply tresholding
  _, detection_im = cv.threshold(detection_im, 50 , 255, cv.THRESH_OTSU)
```

```
    # Apply blur
    detection_im = cv.medianBlur(detection_im, 7)
    # Edge detection
    detection_im = cv.Canny(detection_im,50,100)

    # Create a colored copy of detection_im to be able to draw colored shapes on
    # and display.
    display_im = cv.cvtColor(detection_im, cv.COLOR_GRAY2BGR)

    # Find all the white pixels in the detection image assuming that those
    # pixels are the flame front
    flamefront = cv.findNonZero(detection_im)
    # If there are active pixels and there are more than 5, process the frame.

    if flamefront is not None and flamefront.shape[0] >= 5:
      # 'fitEllipse' gives us the bounding rectangle of the fitted ellipse
      ellipse_info = cv.fitEllipse(flamefront)
      ellipse_center = Point(ellipse_info[0])
      ellipse_axes = Point(ellipse_info[1])
      rotation_angle = ellipse_info[2]

      # Get (x,y) coordinates ofo points on the ellipse.
      points_on_ellipse = cv.ellipse2Poly(ellipse_center.GetInt(), ellipse_axes.GetHalf(),
int(rotation_angle), 0, 360,
                                          360 // NUM_POINTS_ON_ELLIPSE)
      # Subtract the center from all points to get the distance vector of each point.
      dist_vectors = points_on_ellipse - ellipse_center.GetFloat()
      distances = [Point(x, y).Length() for x, y in dist_vectors]
      mean_dist = round(sum(distances) / len(distances), 4)  # Round to 4 digits, change if
needed
```

```
    # Draw the ellipse and its center (as a small circle) on the processed frame
    cv.ellipse(display_im, ellipse_info, ELLIPSE_COLOR, thickness=1, lineType=cv.LINE_AA)
    cv.circle(display_im, ellipse_center.GetInt(), radius=1, color=CENTER_COLOR, thickness=2)

    # Draw the ellipse and its center (as a small circle) on the original frame
    cv.ellipse(frame, ellipse_info, ELLIPSE_COLOR, thickness=1, lineType=cv.LINE_AA)
    cv.circle(frame, ellipse_center.GetInt(), radius=1, color=CENTER_COLOR, thickness=2)

    # Draw colorful sample lines on both images
    hues = list(np.arange(0, 255, 255 // len(points_on_ellipse)))
    for i in range(len(points_on_ellipse)):
     color = [int(x) for x in cv.cvtColor(np.uint8([[[hues[i], 100, 255]]]), cv.COLOR_HSV2BGR)[0][0]]
     cv.line(frame, ellipse_center.GetInt(), points_on_ellipse[i], color, thickness=1, lineType=cv.LINE_AA)
     cv.line(display_im, ellipse_center.GetInt(), points_on_ellipse[i], color, thickness=1, lineType=cv.LINE_AA)

    # Write mean radius near the center point of the ellipse in both images
    avg_radius = mean_dist * DIST_PER_PIXEL
    WriteText(display_im, f'r = {avg_radius:.4f} mm', ellipse_center)
    WriteText(frame, f'r = {avg_radius:.4f} mm', ellipse_center)

  w, h = WriteText(display_im, f'FRAME: {frame_no:.04f}', Point(0, frame_height))
  w2, h2 = WriteText(display_im, f'MSEC: {frame_ms:.06f}', Point(0, frame_height - h))
  w3, h3 = WriteText(display_im, f'MSEC REAL: {frame_no*MS_PER_FRAME:.06f}', Point(0, frame_height -h - h2))
  w, h = WriteText(frame, f'FRAME: {frame_no:.04f}', Point(0, frame_height))
  w2, h2 = WriteText(frame, f'MSEC: {frame_ms:.06f}', Point(0, frame_height - h))
```

```
    w3, h3 = WriteText(frame, f'MSEC REAL: {frame_no*MS_PER_FRAME:.06f}',
Point(0, frame_height - h - h2))

    cv.imshow('Frame', frame)

    cv.imshow('Detection', display_im)

    # Write to csv file.

    csv_writer.writerow({'Frame No': int(frame_no), 'Millisecond (Real)':
frame_no*MS_PER_FRAME, 'Avg. Radius': avg_radius})

    keyboard = cv.waitKey(1000 // 60)

    if keyboard == 'q' or keyboard == 27:

      video_file.release()

      cv.destroyAllWindows()

      break

# Pass the video name to process and the output file name

ProcessVid('eq0.8_1.mp4', 'eq0.8_1
```

C. Expansion Ratios

Table C.1 Calculated expansion ratios for the experimental conditions

Equivalence Ratio	*Mixture [mol %]*		*Expansion ratio(σ)*
	CH_4	*H_2*	
0.6	100	0	5.55
	90	10	5.54
	80	20	5.54
0.8	100	0	6.71
	90	10	6.70
	80	20	6.69
1	100	0	7.48
	90	10	7.45
	80	20	7.44